UNIVERSITY OF OKLAHOMA

GRADUATE COLLEGE

THE ROLE OF SURFACE DRAG IN SUPERCELL TORNADOGENESIS AND MESOCYCLOGENESIS: STUDIES BASED ON IDEALIZED NUMERICAL SIMULATIONS

A DISSERTATION

SUBMITTED TO THE GRADUATE FACULTY

in partial fulfillment of the requirements for the

Degree of

DOCTOR OF PHILOSOPHY

By

BRETT JULIAN ROBERTS
Norman, Oklahoma
2017

THE ROLE OF SURFACE DRAG IN SUPERCELL TORNADOGENESIS AND MESOCYCLOGENESIS: STUDIES BASED ON IDEALIZED NUMERICAL SIMULATIONS

A DISSERTATION APPROVED FOR THE
SCHOOL OF METEOROLOGY

BY

_____
Dr. Ming Xue, Chair

_____
Dr. Howard Bluestein

_____
Dr. Daniel T. Dawson II

_____
Dr. Alan Shapiro

_____
Dr. Alexander Grigo

Acknowledgements

Financial support for the research in this dissertation came primarily from NSF grant AGS-0802888. Computing resources for simulations and data processing were provided by the Texas Advanced Computing Center (TACC) and National Institute for Computational Sciences (NICS) (both through the Extreme Science and Engineering Discovery Environment [XSEDE] program), as well as the OU Supercomputing Center for Education and Research (OSCER) and the Center for the Analysis and Prediction of Storms (CAPS).

Over the past decade, my experiences as a student at the University of Oklahoma and as an aspiring scientist inside the vibrant National Weather Center have led me down a path I only dreamed of as a weather-obsessed child; I owe an immense debt of gratitude to many individuals along that path. First and foremost, I thank my graduate advisor, Dr. Ming Xue, for his guidance throughout the long (and frequently nerve-racking) process of settling into a research role fraught with challenges and controversies. His vast research experience, and particularly his unmatched knowledge of the ARPS model used herein (which he created for his own dissertation), were essential in keeping me on the road to meaningful progress with this work. Discussions, frank advice, and in some cases code from Dr. Daniel Dawson and Dr. Alex Schenkman also proved indispensable while designing experiments, making sense of results, and presenting my work to others. I also wish to thank committee members Dr. Alan Shapiro, Dr. Howard Bluestein, and Dr. Alex Grigo for their guidance, feedback, and taking time out of their busy schedules to participate in the formalities required throughout the doctoral program!

Looking back, I owe thanks to Dr. Fred Carr for his mentorship and advice when I first arrived at OU as a freshman from across the country. All of my professors in the School of Meteorology were professional and contributed something important to the meteorological knowledge I have today; Dr. Kenneth Crawford, Dr. Alan Shapiro (on my committee), Dr. Howard Bluestein (also on my committee), Dr. Brian Fiedler, Dr. David Strensrud, and Dr. Xuguang Wang, among others, made lasting impressions with the course(s) they taught. I thank Travis Smith and Kevin Manross for giving me an opportunity to begin my research career at CIMMS as an undergraduate assistant, and also thank Rick Smith and others at the NWS Norman WFO for allowing me to volunteer there for several years and keep one foot in the operational world, where my passion started. Debra Farmer, Eileen Hasselwander, and Chris Cook at CAPS, as well as Christie Upchurch, Debbie Barnhill, Marcia Polluto and others over the years at the SoM, have kept the institutions supporting this research running like a well-oiled machine and deserve my gratitude.

My many colleagues and friends within the "weather Mecca" known as the NWC have made studying and working here rewarding in countless ways. So many of them deserve thanks; I am particularly grateful for illuminating discussions with Daniel Betten and Derek Stratman during my PhD work, in addition to those mentioned above. Finally, I would not be where I am in my academic career without the support of my family, and particularly my parents. Their encouragement has been unconditional all the way from early childhood to the extended adolescence known as graduate school. Their emphasis on academics was always unwavering; this entailed high expectations, but also nearly unbounded support to help me meet them (including financial support

during my undergraduate years!). My Dad's love of science, mathematics, and technology was an inspiration for the path I've chosen, while my Mom's interest and strength in all things verbal has always provided a much-needed sounding board when stuck with tasks I am less gifted at! As I end another chapter of my life and begin the next, I wish to thank them once more for everything they've done.

Table of Contents

List of Tables

List of Figures

Abstract

Idealized numerical simulations of supercell thunderstorms have been employed for several decades to study tornadogenesis, providing valuable insights that have helped shape our current understanding of the process. Until the past several years, however, most of these simulations used a free-slip lower boundary condition, effectively disregarding the effects of surface drag. In this study, 50-m (tornado-resolving) idealized simulations of a supercell thunderstorm are performed using the Advanced Regional Prediction System (ARPS) with parameterized surface drag. Analyses of the dynamics of low-level mesocyclogenesis and tornadogenesis are conducted.

Two sets of experiments are performed and analyzed in this study. First, a pair of experiments is performed to identify mechanisms by which drag affects storm behavior. In the first experiment (full-wind drag), surface drag is applied to the full wind components; in the second experiment (environmental drag), drag is applied only to the background environmental wind, with storm-induced perturbations unaffected. In the full-wind drag experiment, a tornado develops around 25 min into the simulation and persists for more than 10 min; in the environmental drag experiment, no tornado occurs. An important mechanism leading to tornadogenesis in the full-wind drag experiment is the generation of near-ground crosswise horizontal vorticity by drag on the storm scale as inflow air accelerates into the low-level mesocyclone; this vorticity is subsequently exchanged into the streamwise direction and eventually tilted into the vertical. Preceding tornadogenesis, the low-level mesocyclone in the full-wind drag experiment also intensifies and lowers rapidly toward the ground, which does not occur

in the environmental drag experiment. Circulation budgets for material circuits enclosing the low-level mesocyclone reveal substantial generation of new circulation by surface drag in the full-wind drag experiment, while the mesocyclone circulation in the environmental-drag experiment is primarily barotropic in origin.

A second set of experiments is performed in which the drag coefficient (Cd) is varied over a range of values appropriate for water and land. The initial low-level mesocyclone lowers toward the ground, intensifies, and produces a tornado in all experiments with $C_d > 0$, with the intensification occurring earlier for larger C_d; in the no-drag experiment, the low-level mesocyclone remains comparatively weak during this period. Circulation budgets for material circuits initialized around the mesocyclone again implicate surface drag acting in the inflow region as having generated important new circulation. Although a greater relative contribution from drag is seen as C_d increases, the difference between the last two experiments ($C_d = 0.02$, $C_d = 0.05$) is minimal and the tornado in the latter experiment is weaker, suggesting an upper limit on the drag coefficient for the favorability of this circulation-generating mechanism. Later in the simulations, after precipitation-driven outflow encloses much of the near-ground mesocyclone, tornadoes in experiments with large Cd tend to be weaker and shorter-lived than those in experiments with small Cd. Circulation analysis of a tornado in one strong-drag experiment suggests that the previously described mechanism may still be important even for tornadoes in this context, where baroclinic vorticity is readily available near the vortex. Implications of the proposed roles of surface drag in supercell tornadogenesis dynamics are discussed, and suggestions for future work are offered.

Chapter 1 Introduction

The road to understanding supercell tornadogenesis in the scientific community has been long and circuitous thus far, and much work remains. After supercell thunderstorms were first described at length by Browning (1964), it was a mere decade-and-a-half until Lemon and Doswell (1979) developed a detailed conceptual model of their structure and behavior which endures to this day. Shortly thereafter, Davies-Jones (1984) penned an exhaustive mathematical description of the mechanism which gives rise to mid-level mesocyclones, the defining feature of the supercell thunderstorm. While supercells are disproportionately responsible for all types of severe weather hazards among convective storms, the supercell tornado is by far the most destructive such hazard, and therefore has rightly captured the most focus from the severe storms research community. Even so, understanding the specific physical mechanism(s) which give rise to these tornadoes has proved far more elusive than for the parent storms from which they spawn.

In some ways, we find ourselves in an era of increased skepticism on this topic; conceptual models and hypotheses which had gained considerable consensus over the last two or three decades are now subject to renewed scrutiny. Scientific support for the idea that baroclinic vorticity is the chief supplier of tornadic vorticity dates back at least to Klemp and Rotunno (1983), and a wealth of modeling and observational studies over subsequent years bolstered this concept to varying degrees. Underappreciated for much of that time, perhaps, was that the effects of surface drag are both difficult to observe in nature and completely missing in the free-slip numerical simulations which informed much of our early modeling-based understanding of supercell behavior. Pioneering

work by Schenkman et al. (2012) and Schenkman et al. (2014) has ushered in an exciting new era in which frictional effects are being given their due in the tornadogenesis problem. As further evidence of the scientific upheaval currently underway, Rotunno et al. (2017) directly undermines a fundamental premise which has influenced much of the work on tornadogenesis since the 1980s: namely, that meaningful cyclonic vorticity near the ground *must* be generated within downdrafts, rather than developing rapidly within rising parcels. Amidst a flurry of new ideas and hypotheses from the severe storms community, the work presented in this dissertation aims to contribute one important piece of the discussion by specifically exploring surface drag's role in supercell dynamics and tornadogenesis from an idealized modeling perspective.

The remainder of the dissertation is organized as follows. Chapter 2 provides background, context, and motivation for the study by reviewing how our understanding of supercell thunderstorms and the tornadoes they spawn has evolved over preceding decades. Chapter 3 describes and analyzes a pair of idealized supercell simulations intended to parse out the distinct roles surface drag can play in supercell tornadogenesis. Chapter 4 extends analysis of the same pair of experiments to include the pre-tornadogenesis low-level mesocyclone, and also employs material circuits to quantify holistically mechanisms generating vorticity in the mesocyclone and tornado. Chapter 5 presents a larger set of simulation experiments in which the drag coefficient is varied to test the sensitivity and generality of the effects described in Chapter 3 and Chapter 4. Finally, Chapter 6 summarizes the results of all the simulations herein, their implications, and possible directions for future work in this area.

Chapter 2 Review of Tornadoes, Supercells and Tornadogenesis[1]

The overarching goal of the work in this dissertation is to further our knowledge of tornadogenesis, ideally in a way that can be translated into operational meteorology (e.g., to aid in tornado prediction, either directly by identifying precursors or indirectly by guiding future development of numerical models). It is appropriate, then, to provide context for what we do and do not know about tornadoes through a brief review.

2.1 Tornadoes and their types

A tornado is a rapidly rotating column of air that makes contact with the ground (Bluestein 2007) and is the most intense atmospheric vortex found in nature, posing a serious threat to life and property. Grice et al. (1999) suggest that on 25 March 1948, weather officers at Tinker Air Force Base made the first official tornado forecast in the United States. Since that time, the average number of tornado deaths per year in the U.S. has declined from about 180 in the 1940s to about 50 in 2005 (Ashley 2007), owing to prodigious advances in scientific understanding and an integrated warning system (Brotzge and Donner 2013). Fujita (1971) proposed the Fujita (F) scale to rate tornado damage in a six-tier system, with ratings ranging from F0 to F5; this scale was in wide use until being supplanted by the Enhanced Fujita (EF) scale (WSEC 2006), a refinement which continues to use the same tiers. Brotzge et al. (2013) calculated an array of statistics for tornadoes across the United States in 2003-04 and found that 97% of tornado fatalities, as well as 92% of tornado damage, resulted from supercell thunderstorms. Before narrowing our focus to supercells and their tornadoes, it is

[1] Portions adapted from Roberts et al. (2016) and Roberts and Xue (2017, in press).

appropriate to review our understanding of tornado types, as pertains to the larger-scale convective mechanisms spawning them.

Davies-Jones et al. (2001) (hereafter DJ01) proposed a binary taxonomy of tornadoes. The authors defined type I tornadoes as those arising from a broader parent circulation, which they considered tantamount to a mesocyclone; type II tornadoes were defined as those without such a parent circulation. Subsequently, Agee and Jones (2009) (hereafter AJ09) extended this taxonomy by differentiating within the set of tornadoes with parent circulations. Specifically, AG09 proposed the following categories: supercell tornadoes (type I), quasi-linear convective system (QLCS) tornadoes (type II), and localized convective and shear vortices (type III). As such, the type I category proposed by DJ01 was partitioned into types I-II in the AJ09 taxonomy.

Examples of type III tornadoes in the AJ09 taxonomy include landspouts, waterspouts, and gustnadoes. AJ09 note that because these tornadoes lack a parent circulation, their formation is more directly tied to a local updraft or downdraft than other types. Wakimoto and Wilson (1989) examined a broad set of landspout (Bluestein 1985) tornadoes observed in Colorado, concluding that their formation mechanism typically involved shear instabilities along convergence lines which fortuitously became collocated with a preexisting convective updraft; waterspouts can be regarded as equivalent vortices forming over water (Golden 1971). The definition of *gustnado* is comparatively murky, having sometimes been used in reference to phenomena with substantial similarities to landspouts (Wilson 1986); in a more recent review, Bluestein (2007) specifies this class of vortices to form along thunderstorm gust fronts (to the exclusion of synoptic and mesoscale convergence boundaries which may host

landspouts). Agee (2014) proposed a slight modification to the AJ09 taxonomy which removed gustnado-like vortices entirely, illustrating the continued debate over whether they qualify as tornadoes at all. Aside from exceptional cases such as the intense gustnado-like vortex described in Wakimoto and Atkins (1996), AJ09 consider type III tornadoes incapable of "significant" damage meeting or exceeding the EF2 threshold.

Type II tornadoes (in the AJ09 taxonomy) are spawned within QLCSs. A QLCS is an organized convective system consisting of multiple cells within a broader line structure, such as a bow echo or squall line (Weisman and Trapp 2003). Smith et al. (2012) estimate, based on an exhaustive study of severe weather reports in the United States from 2003-11, that QLCSs are responsible for about 14% of tornadoes and 38% of severe non-tornadic wind events. The existence of tornadoes or tornado-like vortices within QLCSs was noted at least as early as Nolen (1959), who found tornado occurrence within squall lines to coincide with a "line echo wave pattern" (LEWP) in radar reflectivity. Forbes and Wakimoto (1983) documented 17 cyclonic vortices in a ground survey following a QLCS in Illinois, compelling them to muse about the implications for what constitutes a tornado. Przybylinski (1995) leveraged the modern Weather Service Radar-1988 Doppler (WSR-88D) network to analyze a QLCS tornado event in the upper Midwest on 19 July 1983, finding that tornadoes occurred both along a surging gust front and beneath a later mesoscale circulation. Indeed, the existence and dynamics of mesovortices within QLCSs have become important research topics since the 1990s. Mesovortices, whose scale is on the order of 2-20 km, are often found within bow echoes to the north (in the Northern Hemisphere) of their apex (Atkins et al. 2004). A myriad of physical mechanisms have been proposed to explain the formation of

QLCS mesovortices. A landmark modeling study by Weisman and Davis (1998) suggested that the typical vortex couplet configuration (cyclonic north, anticyclonic south; often termed "bookend vortices") observed in QLCSs could plausibly be explained by two distinct mechanism (Fig. 2.1). The first mechanism involves the upward tilting (by air rising over a gust front) of vortex lines produced within easterly shear (consistent with the flow at the leading edge of a strong cold pool in an eastward-moving QLCS); the second involves the downward tilting (by storm-scale downdrafts) of vortex lines produced within westerly shear (consistent with the typical environmental wind profile supporting long-lived QLCSs).

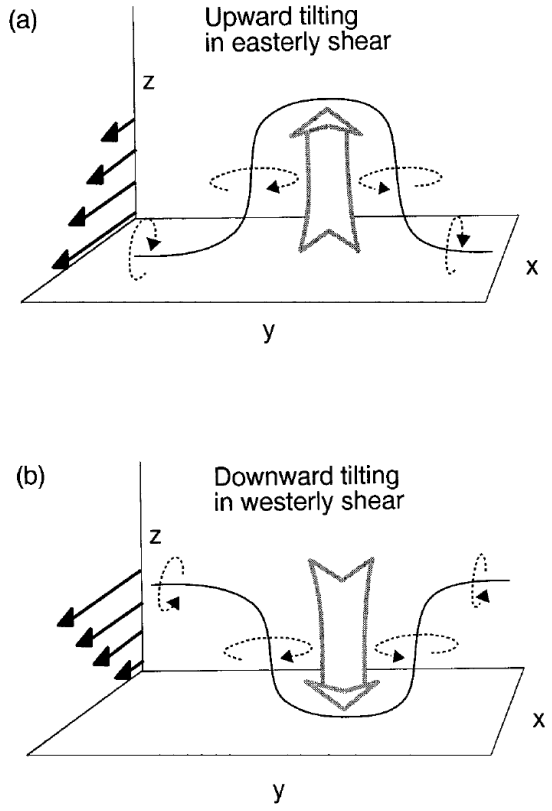

Fig. 2.1. Schematic of vertical vorticity generation through vortex tilting. For westerly shear (b), descending motion pushes the vortex lines down in the center, resulting in cyclonic rotation on the north end and anticyclonic rotation on the south end. Localized ascent in easterly shear (a) produces the same vertical vorticity pattern. From Weisman and Davis (1998).

More recently, modelers have attempted simulations of real QLCS mesovortex and tornado cases. Atkins and Laurent (2009) (hereafter AL09) performed quasi-idealized simulations of a 10 June 2003 bow echo event in Missouri; in analyzing vortices of both a "cellular QLCS" nature and within a subsequent classical bow echo, the authors implicated baroclinic vorticity as the primary mesovortex source in all cases. AL09 employed a free-slip lower boundary condition, conceding that "the lack of surface friction will have some impact on the low-level wind field" while citing earlier coarse-grid modeling studies which showed the inclusion of surface drag not to be important for simulating meso-γ scale and larger vortices. Subsequently, Schenkman et al. (2012) (hereafter S12) performed a 100-m real-data simulation of the 8 May 2007 mesovortex in Oklahoma which included surface drag. S12 analyzed the dynamics of mesovortex-genesis at length, including the use of parcel trajectories with vorticity budgets, and concluded that surface friction was essential to the formation of a "rotor" which supported the mesovortex; this was bolstered by a sensitivity test without drag, in which a much weaker mesovortex (and no tornado) was observed. The fundamental discrepancy between AL09 and S12 regarding the physical mechanism for vortex-genesis mirrors similar uncertainty that has characterized the supercell tornadogenesis problem for decades.

As mentioned at the beginning of this section, supercell tornadoes (type III in the AJ09 taxonomy) are widely recognized as producing a large share of the strongest and most destructive tornadoes (Duda and Gallus 2010; Thompson et al. 2012; Brotzge et al. 2013). As such, the remainder of this chapter will be dedicated to describing supercell storms and their mode of tornadoes.

2.2 Supercell thunderstorms

Browning and Donaldson (1963) were the first to invoke the term "supercell" to describe a long-lived convective storm; in their case, they analyzed a tornadic supercell in Oklahoma (and compared it to another supercell in Great Britain), gaining remarkable insights given the tools and data availability at the time. Browning (1964) then noted some essential features of many supercells: that they often move to the right of the "winds in the middle troposphere," and also that their precipitation tends to fall out downwind of the updraft, supporting their longevity. Within the following decade, enhanced interest in tornadoes and their parent storms would spur research leveraging real-time observations, particularly using Doppler radar. Brandes (1978) performed an illuminating dual-doppler analysis of the wind field for two 1974 tornadic supercells in central Oklahoma, noting the commonly observed "hook echo" accompanying tornadoes and the role of strong inflow wrapping into the low-level mesocyclone. Lemon and Doswell (1979) (hereafter LD79) presented seminal work describing a conceptual model of the tornadic supercell thunderstorm, synthesizing the volume of observational and theoretical work from the 1960s-1970s; in large part, their model endures to this day. Their conceptual model (Fig. 2.2) exhibits several key features. Among them are a forward-flank downdraft (FFD) upstream of the storm updraft, a rear-flank downdraft (RFD) behind and to the right of the updraft, and corresponding forward-flank and rear-flank gust fronts (FFGF and RFGF) which represent the demarcation between precipitation-influenced downdraft air and environmental air. Crucially, the rotating mesocyclone inherent to all supercells is a "divided

mesocyclone" comprised of both updraft and portions of the RFD; the tornado is most often seen near the interface of these two airflows.

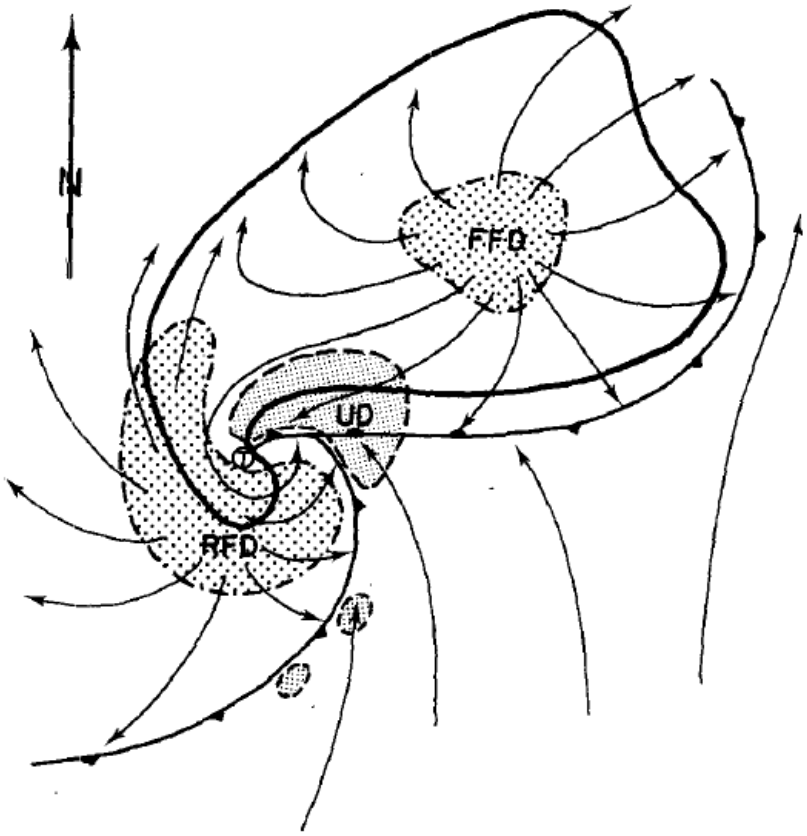

Fig. 2.2. Schematic plan view of a tornadic thunderstorm at the surface. Thick line encompasses radar echo. The thunderstorm "gust front" and "occluded" wave are also depicted using a solid line and frontal symbols. Surface positions of the updraft (UD) are finely stippled, forward flank downdraft (FFD) and rear flank downdraft (RFD) are coarsely stippled, along with associated streamlines (relative to the ground) are also shown. Tornado location is shown by an encircled T. From Lemon and Doswell (1979).

The late 1970s and early 1980s also saw the advent of computing power sufficient for realistic numerical simulations of supercell storms. Klemp and Wilhelmson (1978a) is perhaps the landmark study in this era, reporting exhaustively on the configuration of a three-dimensional cloud model and all its required parameterization schemes (microphysics, subgrid-scale turbulence, and others), and also presenting results from some basic experiments in which convective storms were

initiated with artificial thermal perturbations. This study paved the way for a new era, of which the present study is a part (nearly 40 years later), in which numerical simulations of this type have continually advanced our understanding of supercell dynamics and processes; this has included filling knowledge gaps where observational data was unavailable, or insufficient for major progress. Klemp and Wilhelmson (1978b) used a similar model configuration to simulate splitting supercell storms, correctly identifying the relationship between clockwise (anticlockwise) environmental hodograph curvature and the propensity for right (left) splits to dominate. In the years which followed, additional simulations in this vein unleashed a wealth of knowledge about why supercells develop, propagate and behave as they do, particularly as relates to the influence of environmental wind shear (Klemp et al. 1981; Rotunno and Klemp 1982; Weisman and Klemp 1982).

Davies-Jones (1984) (hereafter DJ84) derived the theoretical correlation coefficient between perturbation vertical velocity (w') and vertical vorticity (ζ') in a thunderstorm updraft; it was shown to vary directly with the proportion of environmental vorticity which is streamwise:

$$\mathrm{r}(w', \zeta') \approx \frac{|\bar{\boldsymbol{v}} - \boldsymbol{c}|}{\sqrt{\sigma^2 D^2 + |\bar{\boldsymbol{v}} - \boldsymbol{c}|^2}} \frac{\bar{\boldsymbol{\omega}}_{\boldsymbol{S}}}{|\bar{\boldsymbol{\omega}}|} \tag{2.1}$$

where $\bar{\boldsymbol{\omega}}_{\boldsymbol{S}}$ is the streamwise component of the environmental vorticity vector. This means that when large streamwise environmental vorticity is available, there is a greater tendency for updrafts to rotate cyclonically. This is another landmark study, as it clearly and quantitatively shows why supercell thunderstorms rotate (in the mid-levels; about 3-7 km AGL). Rotunno and Klemp (1985) demonstrated this fact using numerical simulations, while also exploring the origins of low-level rotation, which will be

discussed in the next section. Davies-Jones et al. (1990) built upon the work of DJ84 to define the quantity storm-relative environmental helicity (SREH); Droegemeier et al. (1993) then showed in numerical simulations that its value (over the 0-3 km AGL layer) is directly related to the propensity for convection to organize into a supercell. Brooks et al. (1994) suggested that mid-tropospheric flow may also be important for supercell longevity and the propensity for a low-level mesocyclone to develop; specifically, mid-level storm-relative flow which is too strong may advect precipitation too far downstream from the updraft for ideal downward transport of barotropic environmental vorticity, whereas flow which is too weak will tend to choke off the updraft with precipitation and cold outflow. Overall, the body of literature suggests that the development of strong, long-lived supercells is dependent on both low-level wind shear (particularly streamwise vorticity and SREH) and wind shear over the depth of the troposphere, a concept which has enabled operational meteorologists to use ingredients-based forecasting with success.

Additional breakthroughs in understanding supercell structure and dynamics arrived in the 1990s with the Verification of the Origins of Rotation in Tornadoes Experiment (VORTEX), a field campaign conducted in the southern Great Plains of the United States from 1994-1995 featuring mobile radars and other instrumentation (Rasmussen et al. 1994). Among the more interesting results from this campaign were a propensity for supercells to produce low-level mesocyclones and tornadoes when interacting with mesoscale boundaries (Markowski et al. 1998; Rasmussen et al. 2000) and a less pronounced discrepancy in storm structure than expected between tornadic and nontornadic supercells (Trapp 1999). More than a decade later, VORTEX2 was

conducted from 2009-2010 with an even larger armada of instrumented vehicles (Wurman et al. 2012). Paired with modern supercomputing power that affords high-resolution simulations assimilating these observational datasets, VORTEX2 has ushered in new research advances which continue to the present time (Coffer and Parker 2017). One prominent theme from work analyzing VORTEX2 observations involves the presence and behavior of internal RFD outflow "surges," both whose cause and relationship to tornadogenesis remain under investigation (Skinner et al. 2014; Marquis et al. 2016). Given our relatively well-formed knowledge of mid-level mesocyclones and first-order supercell dynamics, much work in recent years (including work utilizing VORTEX2 datasets) has focused primarily on the comparatively challenging topics of near-ground mesocyclones and tornadogenesis, which will be addressed in the following section.

2.3 Dynamics of supercell tornadogenesis and low-level mesocyclogenesis

Despite several decades of intense focus from the research community, our understanding of the physical mechanisms responsible for supercell tornadogenesis remains incomplete. Horizontal vorticity in the pre-storm environment has been well-established as the primary source for mid-level rotation in supercells (Davies-Jones 1984); by contrast, various potential sources for near-ground vorticity in a tornadic supercell continue to be investigated. A fundamental question underlying much of the contemporary research on this topic is: does the vertical vorticity associated with tornadoes originate primarily from a baroclinic source, or some other source? The earliest numerical modeling studies of supercells which resolved near-ground circulations (Klemp and Rotunno 1983; Rotunno and Klemp 1985) emphasized the

importance of storm-generated baroclinic vorticity associated with a cool, rainy downdraft. Subsequent observational studies, however, revealed that cooler downdrafts are associated with a decreased likelihood for tornadogenesis; this is true for both the forward-flank (Shabbott and Markowski 2006) and rear-flank (Markowski et al. 2002; Grzych et al. 2007) downdraft regions. To reconcile these findings with the baroclinic mechanism, Markowski et al. (2008) hypothesized the existence of a "goldilocks phenomenon" wherein the cold pool must be of sufficient strength to generate baroclinic vorticity exceeding some threshold, but not so strong as to inhibit upward vertical acceleration of parcels (and hence vertical stretching within an incipient vortex) due to reduced buoyancy. Thermodynamic observations made by Markowski et al. (2012) of the 5 June 2009 Goshen County, WY, tornadic supercell during VORTEX2 supported this theory; sensitivity tests of idealized simulations in Markowski and Richardson (2014) similarly found that an "intermediate" cold pool strength was optimal for generating a strong near-surface vortex.

The relative roles of environmental barotropic vorticity (brought into the storm from the environment) and baroclinically-generated vorticity in producing strong low-level rotation in supercell storms have recently been investigated in idealized simulations by Dahl et al. (2014) (hereafter D14) and Dahl (2015) (hereafter D15), using 250 m horizontal grid spacing (which can at most simulate "tornado-like vortices," not tornadoes themselves). Using a Lagrangian technique for tracking the evolution of vortex line segments in a simulated tornadic supercell, D14 determined that the horizontal vorticity ultimately tilted into the vertical in near-surface vortices was dominated by the baroclinic component; very near the ground, the barotropic vorticity

component generally remained nearly horizontal, in line with the local velocity vector. The importance of the baroclinic mechanism was confirmed using a similar methodology in D15, even for storm environments that contained large crosswise environmental vorticity. Thus, the work of D14 and D15 supports the notion that baroclinically-generated vorticity is paramount for developing strong rotation near the ground in supercells. Most recently, Orf et al. (2017) (hereafter O17) conducted an extremely high-resolution (30-m) supercell simulation based on a sounding from the 24 May 2011 tornado outbreak in Oklahoma; three-dimensional visualizations of their dataset exhibit remarkable similarities to photographs of real tornadic supercells in nature, including structures like the wall cloud and horizontal vortices wrapping around the tornado. A streamwise vorticity current along the FFGF, which owed primarily to baroclinity, was identified as the chief source of tornadic vorticity.

The aforementioned idealized tornadic supercell simulations, including D14, D15, and O17, employed free-slip lower boundary conditions. As such, surface drag (a potentially important source of horizontal vorticity) was neglected, except for its role in producing near-surface vertical wind shear in the environment. Within the context of idealized tornado vortex simulations, researchers employed no-slip lower boundary conditions (and hence included surface drag) in studies of tornadoes as early as the 1990s (Trapp and Fiedler 1995; Lewellen et al. 1997; Trapp 2000). However, these highly idealized experiments typically used artificial, steady-state forcing mechanisms (for both the supporting updraft and the source of vertical vorticity) in lieu of dynamic forcing that would develop within realistic simulations of tornadic storms. Certain questions therefore cannot be answered based on such simulations.

Wicker and Wilhelmson (1993) (hereafter WW93) performed supercell storm simulations in which two fine-mesh (120 m grid spacing) simulations were nested within a coarse mesh (600 m grid spacing) simulation just prior to the development of a strong low-level mesocyclone; surface drag was included in one of the fine-mesh simulations. The results of WW93 demonstrated a contraction of the diameter of a tornado-like vortex (TLV) and substantially stronger low-level updraft around the vortex when surface drag was included, although computational limitations of the time prohibited a more holistic approach with drag enabled throughout the storm's life cycle. Adlerman and Droegemeier (2002) explored the effects of surface drag on mesocyclone evolution as part of a broad parameter-space numerical study, finding more steady-state, persistent mesocyclones with increasing drag coefficient; however, their simulations were limited to a relatively coarse mesocyclone-resolving resolution (x = 500 m), and the authors were forced to use a relatively small drag coefficient ($C_d = 10^{-3}$) to obtain a sustained supercell. When a drag coefficient typical of that over land ($C_d = 10^{-2}$) was used, a mesocyclone did not develop. In Adlerman and Droegemeier (2002), the drag was applied to perturbation winds and the base state was assumed to be in balance with friction (but unlike the present study, no adjustment procedure was applied to ensure that the base state actually was in balance with the model's parameterization of surface drag).

Not until very recent years have real-case simulations incorporating heterogeneous observation-based initial and boundary conditions been performed at tornado-resolving resolutions; such real-case simulations usually include surface drag. Mashiko et al. (2009) modeled a tornadic mini-supercell associated with a typhoon at a

50 m grid spacing by starting from mesoscale NWP (numerical weather prediction) model initial conditions; the authors performed quantitative vorticity budget analyses along parcel trajectories and suggested that preexisting horizontal vorticity in the environment was the dominant source of tornadic vorticity. The direct generation of horizontal vorticity by friction was found to be negligible in their case. A point worth noting is that in their tropical cyclone environment, the low-level vertical wind shear of about 20 m s^{-1} in the lowest 500 m above ground level (AGL) was much larger than that typical of continental tornadic supercell environments. Additionally, the strong near-surface vertical wind shear in the environment can be attributed to surface drag as the strong typhoon circulation moved over land. In other words, large vertical wind shear (and horizontal vorticity) had already been generated by surface drag before the near-surface air parcels entered the tornadic mini-supercell.

Schenkman et al. (2012) simulated a TLV associated with a mesovortex within a mesoscale convective system in Oklahoma, implicating surface drag in the development of a horizontal rotor. The circulation associated with the rotor dramatically enhanced low-level convergence and updraft near the mesovortex center, leading to the development of the TLV. Houser et al. (2016) also reported on a weak-echo reflectivity band in mobile Doppler radar data associated with a rotor-like feature near a significant supercell tornado, identifying surface drag as one possible vorticity source for the rotor. Xue et al. (2014) reported on a successful simulation of a tornadic supercell and embedded tornadoes in central Oklahoma on 8 May 2003 at 50 m grid spacing. Their simulation started from an initial condition that assimilated real radar observations. Through detailed vorticity diagnostic analyses along parcel trajectories, Schenkman et

al. (2014) (hereafter S14) showed that in the same simulation, surface drag played a significant, if not dominant, role in the development of two simulated tornadoes within the supercell. Specifically, surface drag generated large horizontal vorticity which was imported by tornado-entering parcels and then tilted into the vertical. For the first tornado, drag generated horizontal vorticity within an internal rear-flank downdraft (RFD) surge and within low-level inflow. For the second tornado, drag similarly enhanced horizontal vorticity in the low-level inflow of a new developing convective cell. In both cases, horizontal vorticity enhancement by drag was associated with a region of accelerating low-level flow. Most recently, Nowotarski et al. (2015) performed idealized simulations of a supercell that included surface drag and found that convective rolls within the boundary layer can modulate mesocyclone intensity, depending upon their orientation. Their study did not address the role of frictionally-generated vorticity in low-level mesocyclone development, however.

As discussed at length in Section 2.2, supercells are characterized by a persistent mesocyclone (Lemon and Doswell 1979), and the mid-level (3-6 km above ground level [AGL]) mesocyclone is understood to mainly result from tilting of vorticity associated with the vertical shear of environmental wind (Davies-Jones 1984). While all supercells feature mid-level rotation, some also develop mesocyclones below 2 km AGL, and this development can be important for tornadogenesis. Markowski et al. (1998) investigated the tendency for storms to produce tornadoes upon interacting with mesoscale boundaries during the VORTEX field experiment and found that the intensification of the low-level mesocyclone during these interactions to be a critical factor. In a climatological study of mesocyclones detected by WSR-88D radars across the United

States, Trapp et al. (2005) found that while only 15% of mid-level mesocyclones were associated with tornadoes, more than 40% of low-level (below 1 km AGL) mesocyclones were tornadic. More recently, high-resolution modeling studies have also implicated the intensification of the low-level mesocyclone in supercell tornadogenesis (Mashiko et al. 2009; Schenkman et al. 2014). The dynamical link between the low-level mesocyclone intensification and tornadogenesis may be complex and multi-faceted. One potential instigating factor is the enhancement of low-level updraft via pressure drops aloft (Grasso and Cotton 1995; Wicker and Wilhelmson 1995; Noda and Niino 2010), which can augment stretching of vertical vorticity near the ground within an incipient vortex. Low-level mesocyclone intensification may also be associated with rear-flank downdraft (RFD) momentum surges (Schenkman et al. 2016), which can aid in tornadogenesis (Schenkman et al. 2014) and tornado maintenance (Marquis et al. 2012), particularly when parcels comprising the surge have relatively modest potential temperature deficit (Lee et al. 2012; Skinner et al. 2014).

In more recent years, the potentially important role of surface drag in supercell dynamics and tornadogenesis has received increased interest in the severe storm research community. S14 analyzed tornadogenesis processes within a 50-m simulation obtained earlier in Xue et al. (2014), which assimilated Doppler radar and other observations from the 8 May 2003 tornado case in Oklahoma. This study was one of the first realistic tornado simulations employing realistic, heterogeneous environmental conditions that include full model physics including surface friction; most earlier tornado modeling studies used horizontally homogeneous environmental conditions defined by a single sounding, and surface friction was not considered. Individual

trajectory budgets were analyzed for parcels entering two different tornadoes produced by the simulated storm. These budgets showed drag to play a dominant role in generating horizontal vorticity which was ultimately tilted into the vertical and stretched within the tornadoes. Specifically, drag generated large horizontal vorticity within an RFD momentum surge (environmental inflow) in the first (second) simulated tornado. The dominance of frictional vorticity for trajectories entering the first tornado suggests the possibility that even when large baroclinic vorticity is available in close proximity to a developing vortex, there may be some cases in which frictional vorticity is nonetheless an important source.

Mashiko (2016a) (hereafter MS16a) analyzed a mesocyclone in their 50-m simulation of the 6 May 2012 tornadic supercell which struck Tsukuba City, Japan. Notably, this simulation used a heterogeneous, realistic initial condition derived from the Japan Meteorological Agency (JMA) operational mesoscale model analysis. In analyzing a material circuit initialized enclosing the low-level mesocyclone about 2 min prior to tornadogenesis, MS16a found that the circulation about the circuit had doubled during the preceding 15 min. Most of this increase in circulation owed to baroclinic forcing, but frictional forcing had a non-negligible secondary contribution. Mashiko (2016b) (hereafter MS16b) performed analyses of tornadogenesis in the same simulation. In the case of a material circuit initialized at 150 m AGL encircling the tornado at genesis time, a similar result was found to that for the low-level mesocyclone: most of the increase in circulation over the preceding 15 min owed to baroclinic forcing, but frictional forcing was a secondary positive contributor. In MS16b, an RFD outflow surge is said to trigger tornadogenesis, implying the presence

of a mature cold pool near the tornado. MS16b performed a sensitivity experiment in which evaporation of rain and melting of ice-phase hydrometeors were disabled, preventing diabatic cooling. A vortex also developed in this experiment, but was substantially weaker than the one in the control run. Circulation analysis of a material circuit about the tornado in the sensitivity experiment without diabatic cooling suggested that friction contributed a large proportion of the circulation around its weaker vortex, although the integrated and interpolated circulation values did not agree especially well.

Roberts et al. (2016) (hereafter R16), which is adapted to Chapter 3 of this dissertation[2], conducted idealized simulations of a supercell to assess the impact of surface drag on tornadogenesis. Unlike in MS16a, the simulations of R16 were initialized with a single sounding and lacked terrain. Two simulation experiments were performed and compared. In one experiment, the surface drag was applied to the full wind (referred to as full-wind friction, or FWFRIC, hereafter) while in the other experiment, the surface drag is applied to the environmental wind only (EnvFRIC hereafter). The environmental wind profile was set up to be in balance among the Coriolis, environmental horizontal pressure gradient and frictional forces in the experiments. A tornado developed in FWFRIC only 1500 s into the simulation, before a mature cold pool was established, suggesting a fundamentally different genesis mode than that in MS16b. Through trajectory-based vorticity budget analyses, R16 found direct impacts of surface friction that led to tornadogenesis in the FWFRIC experiment but not in the EnvFRIC experiment. Specifically, surface drag was found to have two

[2] Despite its adaptation to a chapter this dissertation, R16 is included for context here because it precedes a few very recent studies chronologically which will be discussed below.

roles in promoting the development of a tornado. First, drag generated new horizontal vorticity as near-ground flow accelerated towards the low-level mesocyclone, and this frictional vorticity was ultimately tilted into the vertical within and near the incipient tornado. Second, drag enhanced low-level horizontal convergence, promoting enhanced updraft near the ground which augmented stretching of vertical vorticity, ultimately leading to a stronger low-level mesocyclone and subsequent development of a tornado.

Markowski (2016) (hereafter M16) used highly idealized simulations to evaluate the relative roles of barotropic, frictional ("viscous"), and baroclinic vorticity in vortex-genesis for supercell-like pseudostorms. Although the methodology of M16 features some overlap with that of R16 from a conceptual standpoint, an important difference is that the simulations of M16 were dry, using an analytically-defined artificial heat sink in lieu of a precipitation-driven downdraft characteristic of a supercell. Nonetheless, the idealized setup of M16 made possible an array of experiments where causality is relatively straightforward. In his simulations, when an environmental sounding with primarily crosswise vorticity in the lowest 250 m AGL was used, a tornado-like vortex developed early in the pseudostorm evolution (similar to the full-wind drag simulation of R16). This early vortex occurred in simulations using both free-slip and semi-slip (i.e., containing parameterized drag) lower boundary conditions. When a different background sounding was used wherein the environmental vorticity in the lowest 250 m AGL was instead primarily streamwise, an early vortex was not observed in either the semi-slip or free-slip simulation; instead, a stronger vortex eventually developed later in the simulations when cool "outflow" from the heat sink reached the low-level mesocyclone. Using material circuits initialized around the vortex and traced backward

in time, M16 demonstrated that frictional vorticity contributes about half of the final circulation in the semi-slip simulation with crosswise initial vorticity. However, the free-slip simulation initialized with the same hodograph developed a similar but *stronger* vortex that owed almost entirely to barotropic vorticity. This result implies that early-storm vortex-genesis in the absence of meaningful baroclinity may be possible *without* surface drag in cases where large crosswise near-ground vorticity is present in the environment. Nonetheless, because surface drag exists in the real world, the semi-slip simulations in M16 should be more realistic than their free-slip counterparts.

Collectively, the results of recent studies addressing drag's role in high-resolution numerical simulations support the possibility of a significant role of friction in supercell tornadogenesis, and the role tends to be larger for tornadogenesis at earlier stages of storm evolution when a mature cold pool has not been established. Observations of real supercells suggest this mode is less common than "mature-storm" genesis, but Doppler radars have observed storms which produced a tornado within half an hour of the first echoes (Palmer et al. 2011). Some non-supercell tornadoes may also develop this way (Xue et al. 2016). Furthermore, a study of significant supercell tornadoes in the central US using WSR-88D radar data reported a handful of cases wherein 30 dBZ radar reflectivity appeared only 30-40 min prior to the first tornado (Boustead and Gross 2016). As asserted in R16, the relevance of simulated "early-storm" tornadoes to supercell tornadoes in the real world is the subject of ongoing investigation. While the "early-storm" tornado in R16 (and in M16's simulations with large crosswise vorticity) provides evidence for the physical plausibility of non-baroclinic vorticity sources dominating tornadogenesis dynamics in certain situations, it

is unclear how often supercell tornadoes actually occur in the absence of precipitation-cooled air nearby. In terms of drag's role in more traditional supercell configurations, spatiotemporally high-resolution datasets of near-ground flow over the lowest few hundred meters AGL are inherently difficult to retrieve using conventional methods (e.g., anemometers are limited to very near the ground, while radar systems cannot measure very near the ground except at a small radial distance); however, a rare example of such a dataset was described by Dowell and Bluestein (1997) (hereafter DB97). Based on observations from a 400-m tall instrumented tower over which a supercell passed in Oklahoma, DB97 noted that low-level horizontal vorticity nearly doubled in the near-storm environment (compared with the far field), and suggested this was important for low-level mesocyclogenesis and tornadogenesis in the storm. This is perhaps one indication that vorticity generated directly by drag *could* be important in typical tornadogenesis cases.

The idea that surface drag, terrain, and land cover properties may in some cases influence supercell processes (including tornadogenesis) is motivating a new era of scientific study and literature. Tang et al. (2016) discussed potential interactions between terrain and a supercell in New York which produced an EF3 tornado; terrain channeling of unstable air was suggested to have enhanced the storm's intensity. Elsner et al. (2016) examined the relationship between elevation roughness and tornado reports in the central United States, finding a small but statistically significant effect: specifically, areas with uniform elevation (flat terrain) are associated with a slightly higher likelihood of tornado reports, when compared against areas with relatively variable elevation. Katona et al. (2016) performed statistical analyses on a large volume

of operational NWP output from the High-Resolution Rapid Refresh (HRRR) model and found statistically significant local anomalies in parameters measuring wind shear that are likely attributable to terrain effects. Ongoing work by Larissa Reames employs idealized numerical simulations (at much coarser resolution than the storm-scale simulations in this study) to evaluate the effects of land use properties, including urban areas, on supercell thunderstorms. One important preliminary result is that, when a large urban area is placed upstream of a simulated supercell, a tendency is seen for a stronger low-level mesocyclone and more rightward storm motion (L. Reames, personal communication). The aforementioned studies help illuminate some of the potential operational implications of understanding how surface drag impacts tornado-producing storms, serving as further motivation for the present study.

Chapter 3 The Role of Surface Drag in Tornadogenesis[3]

3.1 Methodology

3.1.1 Model setup and parameters

The nonhydrostatic Advanced Regional Prediction System (ARPS) (Xue et al. 2000; Xue et al. 2001) is used to produce the pair of idealized simulations. The simulation domain is 64x96 km in the horizontal and 16 km in the vertical, with a Rayleigh sponge layer applied above 12 km AGL. Grid spacing is 50 m in the horizontal. The vertical grid spacing increases from 20 m at the surface to 400 m above 10 km AGL, with a total of 83 levels. The lower boundary is flat and the first level of scalar variables (as well as horizontal momentum) is at 10 m AGL. Advection is fourth-order in the horizontal and vertical. Parameterization of microphysics follows the five-species formulation of Lin et al. (1983) with a modified rain intercept parameter (N_{0r}) of $2x10^6$ m^{-4}; values reduced from the default of $8x10^6$ m^{-4} have yielded more realistic cold pools and stronger TLVs in previous supercell simulations (Snook and Xue 2008; Dawson et al. 2010; Dawson et al. 2015). Subgrid-scale turbulence is parameterized using the 1.5-order TKE formulation of Moeng and Wyngaard (1988), and fourth-order computational mixing is employed. Both experiments are integrated forward in time for 7200 s, although the results presented herein will focus on the first 2400 s.

The two experiments, to be referred to as FWFRIC ("full-wind friction") and EnvFRIC ("environment-only friction"), are differentiated solely by the surface drag formulation. The purpose of these experiments is to discriminate between effects from the frictionally-induced near-ground wind shear in the background environment versus

[3] Adapted from publication: Roberts, B., M. Xue, A. D. Schenkman, and D. T. D. II, 2016: The Role of Surface Drag in Tornadogenesis within an Idealized Supercell Simulation. *J. Atmos. Sci.*, **73,** 3371-3395.

effects from friction acting on the storm-induced wind perturbations. In both experiments, surface drag acts on the environmental flow, but only in FWFRIC does drag act on the storm-induced perturbation winds. The environmental flow, as will be shown below, is balanced by the horizontal pressure gradient force (PGF), the Coriolis force and the frictional force.

In the ARPS, surface drag is introduced through horizontal momentum stresses defined at the surface:

$$-\tau_{13}(z=0) = \rho C_d V_h u, \tag{3.1}$$

$$-\tau_{23}(z=0) = \rho C_d V_h v, \tag{3.2}$$

where τ_{13} and τ_{23} are components of the Reynolds stress tensor which appear in the subgrid scale turbulence parameterization; C_d is the dimensionless drag coefficient valid at 10 m AGL; u and v are the ground-relative horizontal wind components; and V_h is the ground-relative horizontal wind speed. In FWFRIC, the standard ARPS formulation for surface drag is used, as specified in (3.1) and (3.2). In EnvFRIC, surface drag operates only on the base-state wind components as defined by the environmental sounding; thus, storm-induced deviations from the environmental profile are not subject to surface drag. Mathematically, this is represented as:

$$-\tau_{13}(z=0) = \rho C_d \overline{V_h} \bar{u}, \tag{3.3}$$

$$-\tau_{23}(z=0) = \rho C_d \overline{V_h} \bar{v}, \tag{3.4}$$

where $\bar{u}$ and $\bar{v}$ are the base state wind components (as defined by the environmental sounding), and $\overline{V_h}$ is the corresponding wind speed. In the simulations presented herein, the drag coefficient C_d is set to 0.01, which is on the high end of representative values

over land. The use of a fixed value, rather than parameterized values as used in S14, simplifies the interpretation of the results of our idealized simulations.

For both experiments, the horizontally-homogeneous environment is based on a sounding extracted from a real data simulation of the 3 May 1999 central Oklahoma tornado outbreak from Dawson et al. (2010) (hereafter DA10). The sounding comes from the inflow region of the simulated storm valid at 2300 UTC, and was also used to initialize subsequent idealized simulations in DA10, as it was believed to better represent the storm environment than the closest available observed sounding (at Norman, OK). In this study, the original extracted sounding from DA10 is modified to ensure that the profile is balanced among the PGF, Coriolis, and frictional forces; the procedure employed for this modification will be described in the next subsection. With this configuration, the environmental wind profile (for both FWFRIC and EnvFRIC) remains more or less unchanged throughout our simulations. In addition, to keep the simulated storm quasi-stationary near the center of the computational domain, we subtract the observed storm motion[4] of the 3 May 1999 central Oklahoma tornadic supercell ($u = 9.8$ m s^{-1}, $v = 7.8$ m s^{-1}) from the final environmental sounding. We call the storm-relative soundings before and after the force-balance adjustment *MAY3* and *MAY3B*, respectively.

Finally, convection in the model is triggered by an ellipsoidal thermal perturbation centered at $x = 40$ km, $y = 56$ km, and $z = 1.5$ km. The ellipsoid has a radius of 10 km in the horizontal and 1.5 km in the vertical, and the maximum potential temperature perturbation is 6 K at the center. This amplitude is necessary to obtain a

[4] The storm motion was calculated manually using reflectivity data from the KTLX WSR-88D radar.

sustained storm due to the very weak lid atop the planetary boundary layer (PBL) in our initial sounding, based on sensitivity tests.

3.1.2 Establishment of a balanced sounding and initialization of the storm environment

In three-dimensional (3D) idealized simulations, when the Coriolis force is included, the background environment should be in hydrostatic balance and (above the PBL) also in geostrophic balance. In the presence of vertical wind shear, then, there should be a thermal wind balance. This would imply the presence of a horizontal temperature gradient, unlike the horizontally-homogeneous background environments traditionally used for single-sounding simulations. Furthermore, for simulations including the effect of surface drag, there is an additional frictional force within the PBL as a result of vertical momentum stress divergence. In the simplest case of constant eddy viscosity and a constant PGF within the PBL, the boundary layer wind would have a steady state Ekman spiral profile. In this study, we wish to define a storm environment that is in geostrophic balance above the PBL, and in a three-force balance (with friction added) within the PBL. When this force balance exists, the model state will remain steady over time in the absence of convective storm perturbations. In our case, we want to introduce a convective storm into this environment and study the effect of surface drag on the storm.

Setting up a 3D environment in thermal wind balance based on a single sounding is non-trivial, especially for a sounding with vertical wind shear that varies with height. A horizontal temperature gradient would need to be introduced into the background environment; for a geostrophic wind shear of 10 m s^{-1} over a 1 km vertical depth, this horizontal gradient would be about 3 K/100 km. Enforcing thermal wind

balance in this way may introduce unrealistic structures into the vertical temperature profiles, complicating the analysis of the simulated supercell storm (e.g., when inflow air parcels from different parts of the model domain have different thermodynamic properties). Such issues were discussed at length in Skamarock et al. (1994) (hereafter S94). For these reasons, we follow S94 and choose to neglect the horizontal temperature gradient associated with thermal wind balance, considering only the first-order geostrophic wind balance (and a three-force balance within the PBL). The horizontal pressure gradient is assumed to be in geostrophic balance with the environmental wind above the frictional boundary layer. The balance equations are:

$$0 = -\frac{1}{\rho_s}\frac{\partial p_s}{\partial x} + fv_s\,, \tag{3.5}$$

$$0 = -\frac{1}{\rho_s}\frac{\partial p_s}{\partial y} - fu_s\,. \tag{3.6}$$

Here subscript *s* denotes the base state that is in a hydrostatic and geostrophic balance. The supercell storm in our study has a spatial scale of only tens of kilometers, and we analyze our simulation over a period of 40 minutes, so the horizontal distance travelled by air parcels is relatively small (on the order of 10 km). The effects of neglecting the background horizontal temperature gradient should therefore be small for the short duration of our study; substantially smaller, in fact, than in the larger-scale mesoscale convective system (MCS) simulations of S94. In the present study, the base state variables ρ_s, p_s, u_s and v_s are defined by the original extracted sounding (*MAY3*) while the geostrophic horizontal pressure gradient is given by Eqs. (3.5) and (3.6). *MAY3* is assumed to be in geostrophic balance for the purpose of our adjustment procedure,

despite the profile exhibiting a frictional PBL; the consequences of this will be discussed below.

In our simulations, surface drag is continuously acting on the environmental wind profile. For the background environment in these simulations to remain unchanged over time, a three-force balance within the PBL needs to be established. This is achieved by first running a 1D column version of ARPS for 48 h (long enough for geostrophic adjustment[5]), using the original extracted sounding *MAY3* as the initial profile (this profile defines the base-state variables with subscript *s*). This 1D column simulation uses the same vertical grid and parameterization settings described in Section 3.1.1, and surface drag is turned on and applied to the full wind.

When the 1D solution reaches a steady state, the following equations are satisfied:

$$0 = -\frac{1}{\rho_s}\frac{\partial p_s}{\partial x} + f(v_s + v') + F_x[u_s + u'], \tag{3.7}$$

$$0 = -\frac{1}{\rho_s}\frac{\partial p_s}{\partial y} - f(u_s + u') + F_y[v_s + v'], \tag{3.8}$$

where the prime terms are deviations from the original sounding *MAY3*, and *F* represents the frictional terms. $F[\square]$ denotes that surface drag is calculated from the quantity $\square$ inside the square bracket. The final wind profile 48 h into the 1D simulation, given by $\bar{u} = u_s + u'$, $\bar{v} = v_s + v'$, is taken as the profile for *MAY3B*, which is used to initialize our 3D simulations. As mentioned earlier, the storm motion has been subtracted from the wind profile in both *MAY3* and *MAY3B*, but the *ground-relative*

[5] The wind profile in the 1D column simulation reaches a quasi-steady state after 12 h, but integration is carried out to 48 h to ensure robustness.

wind speed is always used in the calculation of surface drag. We note that in our simulations, the Coriolis force is actually applied only to deviations from *MAY3*, because of the assumed balanced between the base-state horizontal PGF and the base-state geostrophic wind, as given by Eqs. (3.5) and (3.6).

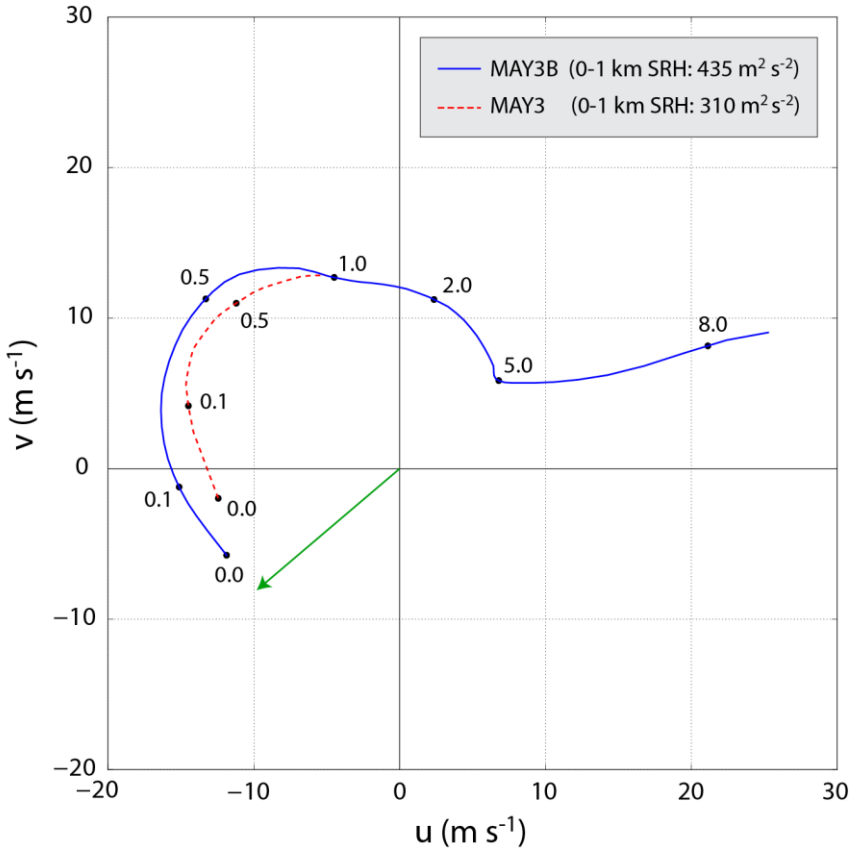

Fig. 3.1. Wind hodograph for storm-relative soundings *MAY3B* (solid blue) and *MAY3* (dashed red) up to 8 km AGL. Numerical values along the hodograph denote the height AGL (km) at which the nearest black dot is valid. Above 1 km AGL, the hodographs are qualitatively identical, so *MAY3* is omitted for clarity. The green arrow represents the "ground-motion vector" (i.e., the vector which was added to the original extracted wind profile to obtain a quasi-stationary storm in our simulations). The 0-1 km AGL storm-relative helicity is provided for each hodograph in the legend.

Fig. 3.1 shows the storm-relative hodographs for *MAY3* and *MAY3B*. Vertical wind shear is stronger within the lowest 1 km AGL in *MAY3B*, resulting in a 0-1 km AGL storm-relative helicity (SRH) approximately 40% larger than in *MAY3*. Although we assume *MAY3* is in geostrophic balance when we initialize the 1D adjustment

simulation, DA10's simulation from which *MAY3* is extracted actually did include surface drag (using a stability-dependent drag coefficient whose value at the sounding location was smaller than our constant value of C_d = 0.01). This yields somewhat exaggerated near-ground wind shear in *MAY3B*, compared to starting the 1D simulation with the true geostrophic wind profile (which is not precisely known, but contains much less shear in the lower levels than *MAY3*). Sensitivity testing suggests that about half of the difference in 0-1 km SRH between *MAY3* and *MAY3B* owes to this geostrophic assumption, with the remaining difference being attributable to the larger drag coefficient in our simulations.

Although *MAY3B* exhibits modestly exaggerated 0-1 km SRH, it nonetheless represents a profile in three-force balance among the horizontal PGF, Coriolis, and frictional forces in the model. To verify that this force balance holds in the 3D simulations, a version of experiment FWFRIC without an initial thermal bubble is integrated for 2400 s; the final kinematic profile throughout the domain is found to be virtually unchanged from the initial profile (not shown). Note that during the 1D column run, the moisture and temperature profiles from *MAY3* are also modified somewhat as the turbulence scheme operates on a grid with a higher vertical resolution than that used in DA10. This is a consequence of the 1.5 TKE formulation specifying mixing length as a function of grid spacing (Moeng and Wyngaard 1988). The resulting profile exhibits a relatively realistic, well-mixed boundary layer (Fig. 3.2). This modified thermodynamic profile is used in *MAY3B*, allowing the background environment to remain virtually unchanged during the 3D simulations.

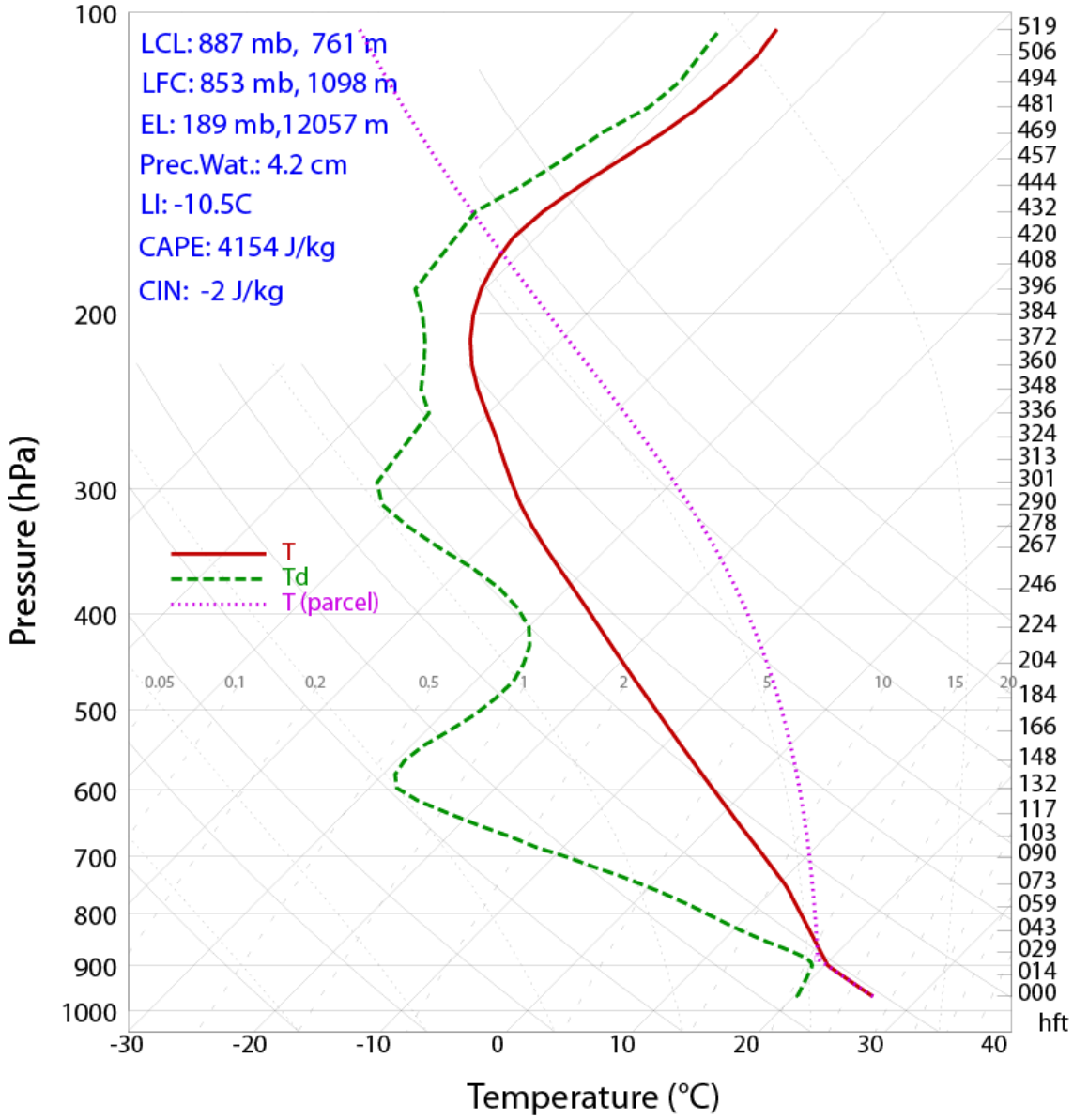

Fig. 3.2. Skew-T log-P plot for sounding *MAY3B*. The environmental temperature and mixing ratio are denoted by the solid red and dashed green lines, respectively. The temperature for an ascending surface-based parcel is denoted by the pink dotted line.

3.2 Simulation results

3.2.1 Overview and qualitative comparison of experiments

This section compares and contrasts experiments FWFRIC and EnvFRIC. In both cases deep convection develops rapidly during the first 600 s from the initial thermal bubble at (x = 40 km, y = 56 km). By 600 s, convergence has developed at the

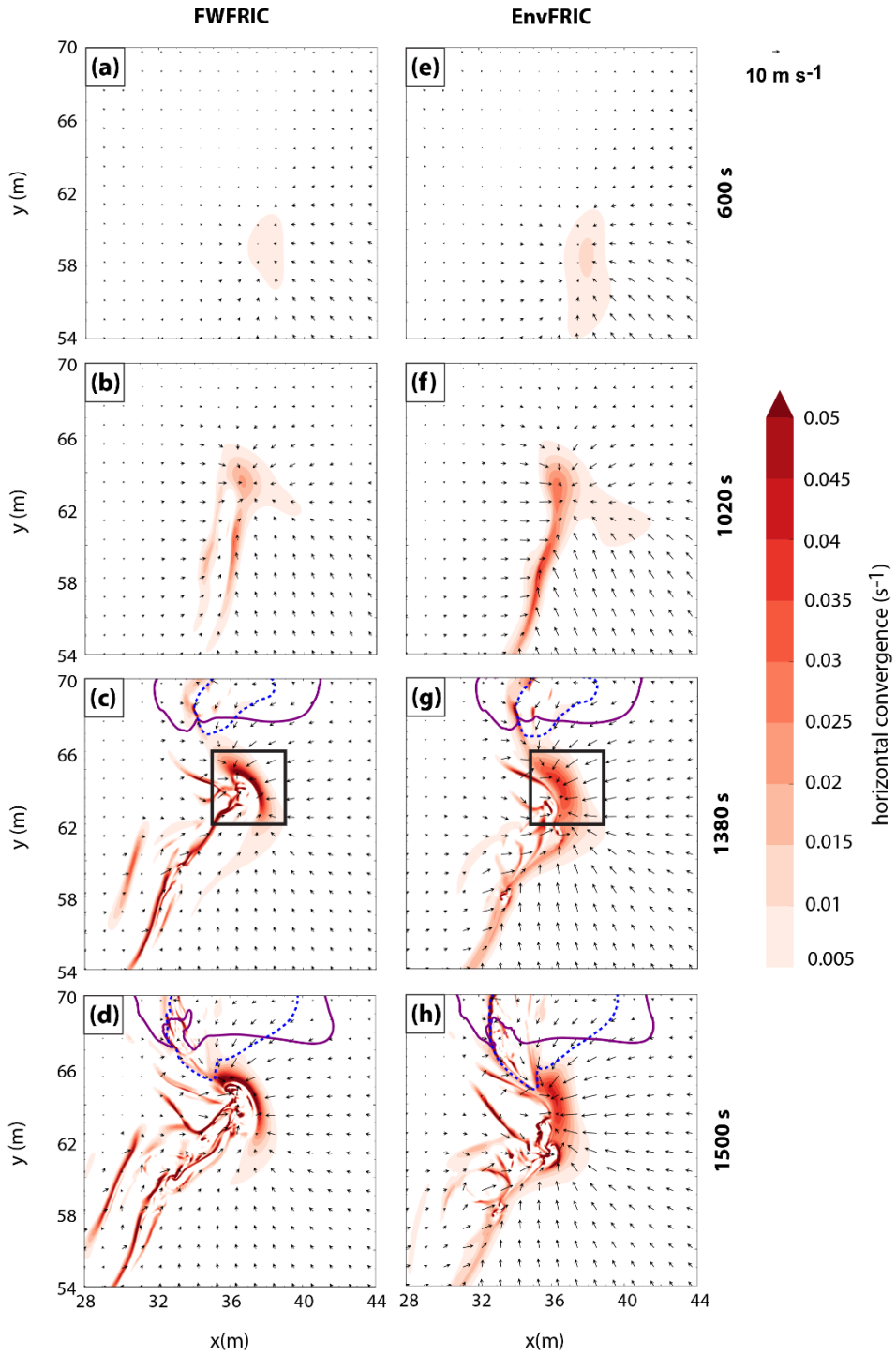

Fig. 3.3. Horizontal convergence (shaded), -1 K perturbation potential temperature contour (dashed blue), 0.3 g kg^{-1} rainwater mixing ratio contour (solid purple), and ground-relative wind vectors at 10 m AGL for FWFRIC at (a) 600 s, (b) 1020 s, (c) 1380 s, and (d) 1500 s; and for EnvFRIC at (e) 600 s, (f) 1020 s, (g) 1380 s, and (h) 1500 s. The storm motion is added to the model wind field to obtain ground-relative wind vectors. In panels (c) and (g), the black box denotes the zoomed region plotted in Fig. 3.4.

lowest model level in response to the strong updraft (Fig. 3.3a and e). The convergence continues to strengthen underneath the main updraft and along a north-south oriented boundary over the next 7 minutes (Fig. 3.3b and f) and beyond.

The low-level wind pattern in FWFRIC and EnvFRIC is qualitatively similar through 600 s. More noticeable differences start to appear around 700-900 s at the lowest model level (10 m AGL), when the flow directed towards the convergence boundary in EnvFRIC grows significantly stronger than in FWFRIC, reflecting the retarding effect of surface drag on convection-induced winds in the latter. This trend continues through 1200 s. Despite the noticeable difference between the two experiments, the general pattern of the low-level flow is still qualitatively similar at 1020s (Fig. 3.3b and f).

By 1380 s, the first convective precipitation has reached the ground in both experiments. In FWFRIC, the strongest surface convergence is concentrated primarily in a small, arcing zone at the northern tip of the convergence boundary; the convergence boundary itself is also thinner with a stronger maximum convergence magnitude (Fig. 3.3c). By contrast, the surface convergence boundary in EnvFRIC appears more diffuse, albeit with some arcing at the northern end (Fig. 3.3g). The convergence boundary is reminiscent of a rear-flank gust front associated with a classical RFD (Lemon and Doswell 1979) in both extent and storm-relative position. However, in the absence of significant precipitation or a cold pool, we do not consider the boundary a rear-flank gust front. While details of this boundary's formation are beyond the scope of this paper, we speculate its development to be a result of interaction between the low-level storm-relative vertically-sheared environmental flow and the storm-induced flow

converging towards the center underneath the developing updraft. The vertical wind shear in the environment is likely a key factor[6].

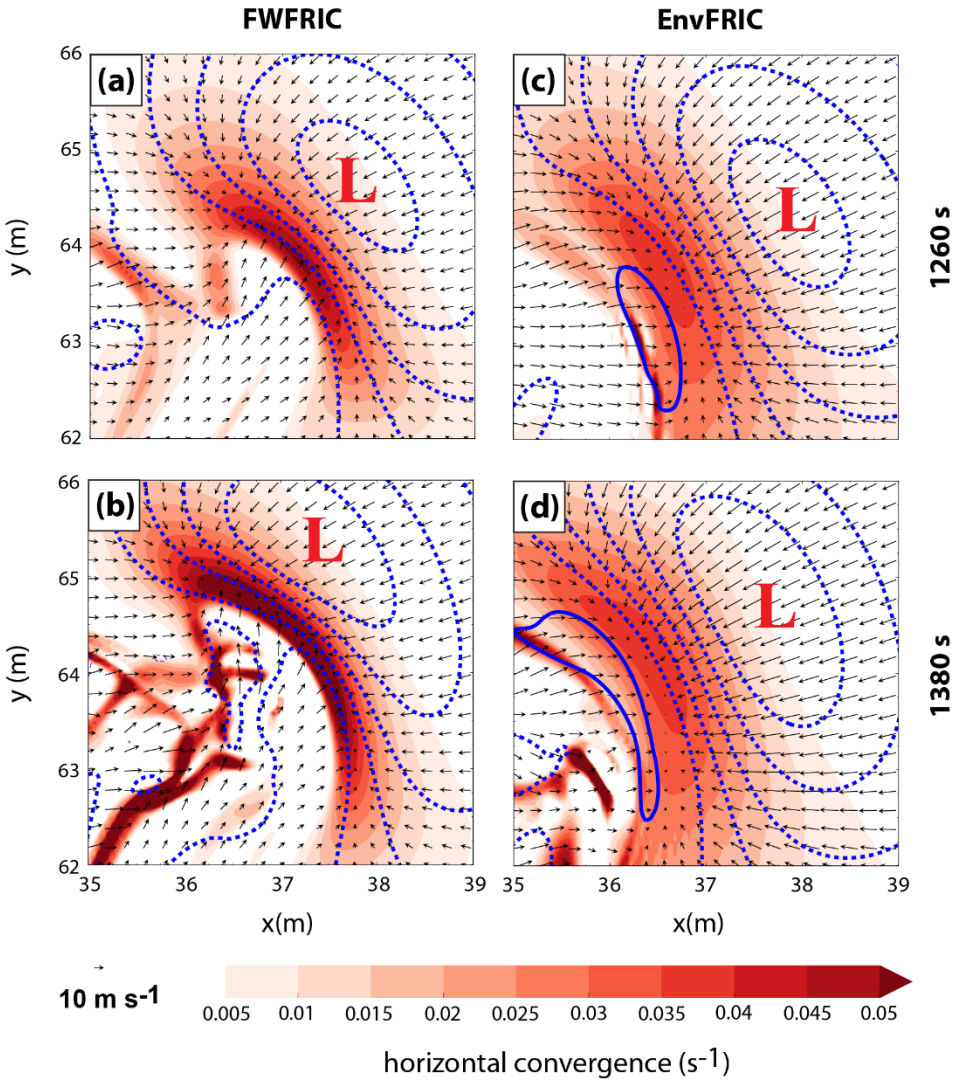

Fig. 3.4. Horizontal convergence (shaded), perturbation pressure (blue contours, 0 hPa in thick line, and negative values at 1 hPa intervals dotted), and ground-relative wind vectors at 10 m AGL for FWFRIC at (a) 1260 s and (b) 1380 s; and for EnvFRIC at (c) 1260 s and (d) 1380 s. Red "L" in each panel denotes local pressure minimum.

Between 1380-1500 s, differences between low-level winds in the two experiments continue to increase near the area of maximum surface convergence (Fig.

[6] If the environmental wind were constant throughout the depth of the atmosphere, the low-level flow would remain symmetric about the convergence center underneath the updraft (in the absence of surface drag).

3.3d and h). In particular, the arcing boundary in FWFRIC becomes more curved than in EnvFRIC, with a thinner and stronger convergence zone. To examine the evolution of this boundary more closely, a zoomed plan view of horizontal convergence, perturbation pressure, and ground-relative wind is presented in Fig. 3.4. At 1260 s, the difference between experiments in boundary curvature is still relatively small (Fig. 3.4a and c), although the difference in the width of convergence zone is significant. The most notable difference in the wind field is found immediately to the west of the boundary near (x = 36 km, y = 63 km), where flow in FWFRIC has a prominent northward-directed component which is absent in EnvFRIC. Immediately west of the boundary, flow in FWFRIC is directed northeastward, approximately normal to the boundary; flow in EnvFRIC is directed eastward, meeting the boundary at a substantially smaller angle. This enhances the surface convergence in FWFRIC and promotes the development of curvature along the northern segment of the boundary. By contrast, the northern segment of the boundary in EnvFRIC does not bend back to the west as much, as flow west of the boundary retains a strong westerly component. By 1380 s, the arcing boundary in FWFRIC has become more curved (Fig. 3.4b); a secondary convergence zone has developed near (x = 36 km, y = 64 km) to the west of the primary zone, creating a horseshoe-shaped convergence boundary. No clearly-defined secondary convergence boundary forms in EnvFRIC, and the main boundary remains comparatively straight and broad (Fig. 3.4d).

Time-height cross-sections of domain-wide maximum updraft speed show more dramatic differences between the two experiments at later times (Fig. 3.5). The experiments are qualitatively similar in terms of domain-wide maximum updraft until

1300 s, when a stronger updraft develops around 1.5 km AGL in FWFRIC. This stronger updraft quickly expands in vertical extent both upward and downward, exceeding 30 m s^{-1} at 250 m AGL in the developing tornado by 1500 s. Horizontal cross-sections (not shown) reveal that the strong updraft in FWFRIC is positioned almost directly above the strongest surface convergence.

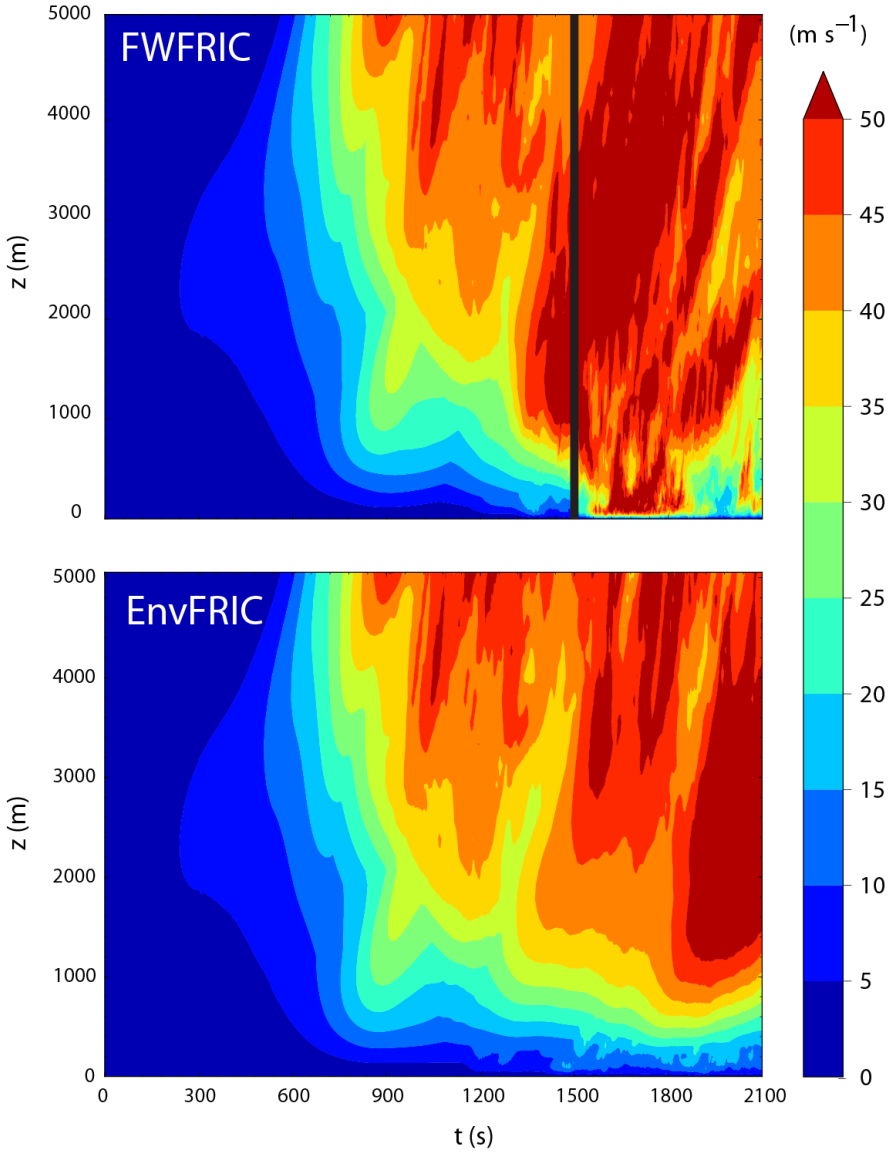

Fig. 3.5. Time-height section of domain-wide maximum updraft for FWFRIC (top) and EnvFRIC (bottom), valid from 0 s to 2100 s. The heavy black vertical line in FWFRIC denotes the time of tornadogenesis (1500 s).

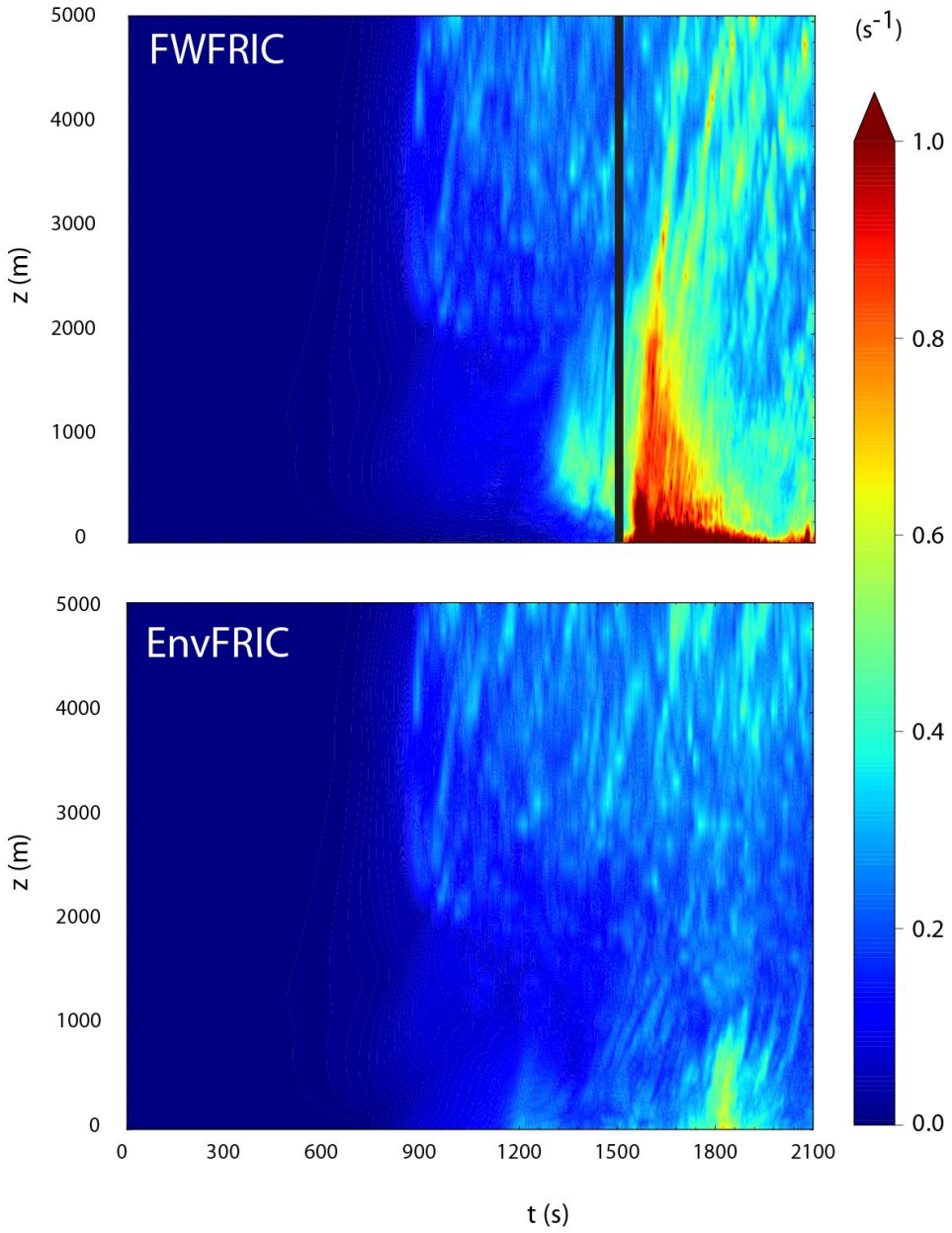

Fig. 3.6. As in Fig. 3.5, but for domain-wide maximum vertical vorticity.

The time-height vertical sections for domain-wide maximum vertical vorticity (ζ) (Fig. 3.6) also show that the two experiments are qualitatively similar until around 1200 s. Around that time, enhanced cyclonic ζ develops in FWFRIC at between 500 m and 1000 m AGL and expands in vertical extent after 1350 s. Coincident with the development of strong surface convergence and low-level updraft, a concentrated area

of cyclonic vertical vorticity develops at the lowest grid level (10 m AGL) in FWFRIC by 1350 s near (x = 37 km, y = 63 km) (Fig. 3.7a). This strong vorticity center is considered a pre-tornadic vortex (PTV) until 1500 s. Shortly before 1500 s, very large vertical vorticity exceeding 1 s^{-1} develops at the surface, which expands upward to 500 m AGL quickly. By this time, the surface vortex has reached tornado intensity based on our criteria that the maximum near surface horizontal wind speed (V_h) exceeds the EF0 threshold (29 m s^{-1}) and ζ exceeds 0.3 s^{-1}, criteria which will be used throughout this dissertation. The vortex maintains tornado intensity through 2100 s and beyond (Fig. 3.6). By contrast, while the largest ζ is found near the ground in EnvFRIC near 1800 s, it never exceeds 1 s^{-1}. Horizontal cross-sections near the ground in EnvFRIC reveal that only transient areas of $\zeta > 0.3$ s^{-1} occur along the convergence zone during the same time period (not shown). Eventually, a shallow vortex (extending upward only to about 1 km AGL) forms around 1800 s that persists for about 60s. However, wind speeds in this vortex do not exceed the EF0 threshold, so tornadogenesis does not occur in EnvFRIC.

The tornado in FWFRIC reaches its peak intensity around 1620-1680 s (Fig. 3.7c), during which time the maximum V_h near the ground approaches 100 m s^{-1} and ζ at the lowest grid level AGL briefly exceeds 2 s^{-1}. A vertical cross-section through the tornado at 1620 s reveals that it extends vertically to 2-3 km AGL, tilting from SSE to NNW with height (Fig. 3.8a). Fig. 3.8a also shows that by this time, a two-celled structure has developed in the tornado; at its center exists a downdraft which is strongest below 500 m AGL, and the downdraft is also found between 1300 and 1900 m

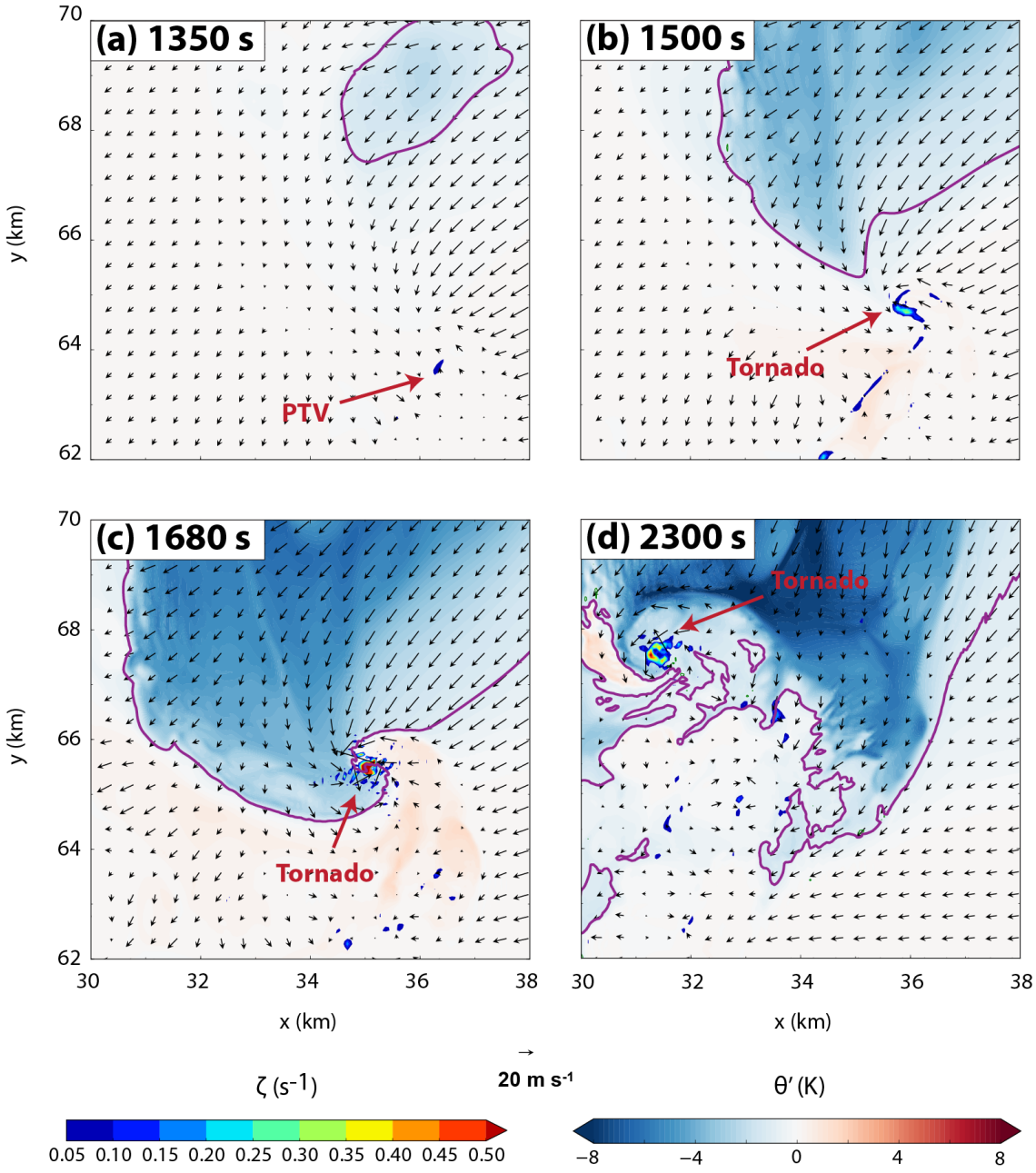

Fig. 3.7. Evolution of pre-tornadic vortex (PTV) and subsequent tornado in FWFRIC at 10 m AGL at (a) 1350 s, (b) 1500 s, (c) 1680 s, and (d) 2300 s. Perturbation potential temperature is shaded, with the -1 K contour highlighted in purple. Vertical vorticity is shaded in the foreground where $\zeta > 0.05$ s^{-1}. Ground-relative wind vectors are plotted. The location of the PTV/tornado is denoted in each panel.

AGL. The downdraft is consistent with the large negative pressure perturbation near the surface at the vortex center, creating a large negative downward PGF (Fig. 3.8b). The low-level downdraft is surrounded by strong updraft which exceeds 35 m s^{-1} at about

100 m AGL on the NNW side of the vortex. The maximum vorticity is found at the center of the vortex, consistent with the structure seen in the horizontal cross section in Fig. 3.7c. At later times, an annular structure develops in the vorticity field where maximum vertical vorticity is found within a ring surrounding the center (Fig. 3.7d). Horizontal cross-sections at and above 1 km AGL (not shown) indicate that the tornado is positioned near the center of the broader low-level mesocyclone.

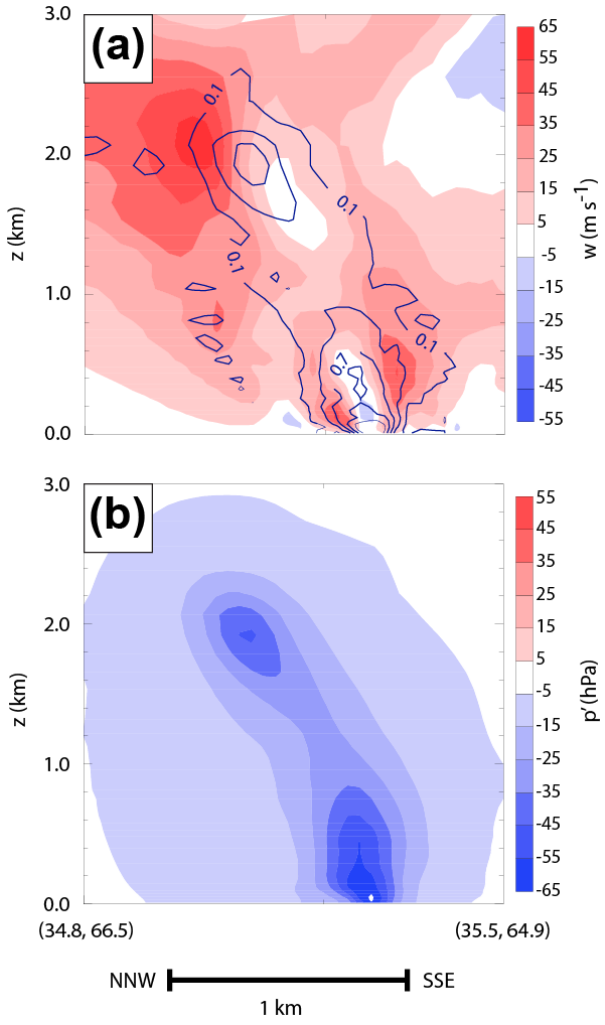

Fig. 3.8. Vertical cross-section through the tornado in FWFRIC at 1620 s of (a) vertical velocity (shaded) and vertical vorticity (contour; units s^{-1}), and (b) perturbation pressure (shaded). The cross-section is along a vertical plane extending from (x=34.8 km, y=66.5 km) at the north-northwest end to (x=35.5 km, y=64.9 km) at the south-southeast end.

3.2.2 Trajectory analysis of PTV/tornado in FWFRIC

We will focus on experiment FWFRIC for the remainder of Section 3.2 because it produced a tornado. Parcel trajectories are initialized in the vortex for various times preceding, during and after tornadogenesis. These trajectories are numerically integrated backward in time for 900 s using the fourth-order Runge-Kutta method from model output wind fields (at an interval of 2 s, with 0.25 s subintervals to which the wind field is interpolated linearly in time between data files) to trace the source of vorticity feeding the vortex in the low-levels. Of particular interest is the evolution of the Lagrangian source terms for both vertical and horizontal vorticity components as parcels approach and enter the vortex.

D14 discussed at length the challenges associated with treatment of trajectories passing below the lowest scalar variable level (which is half a grid interval above ground: 10 m AGL for the present study, and 50 m AGL for the simulations of D14), particularly in the context of vorticity budget analyses. They discussed two possible treatments for parcels in this region for free-slip lower-boundary simulations: (1) assuming no vertical gradient for horizontal velocity below the lowest scalar level, and (2) extrapolating horizontal velocity downward from the lowest scalar level to ground-level. Both methods can result in a dynamical inconsistency between the vorticity field and horizontal velocity field, and are therefore problematic in the context of Lagrangian vorticity budgets. In semi-slip simulations such as those in the present study, vorticity is similarly ill-defined in this region, since a zero-gradient condition is assumed for the horizontal wind components across the lower boundary.

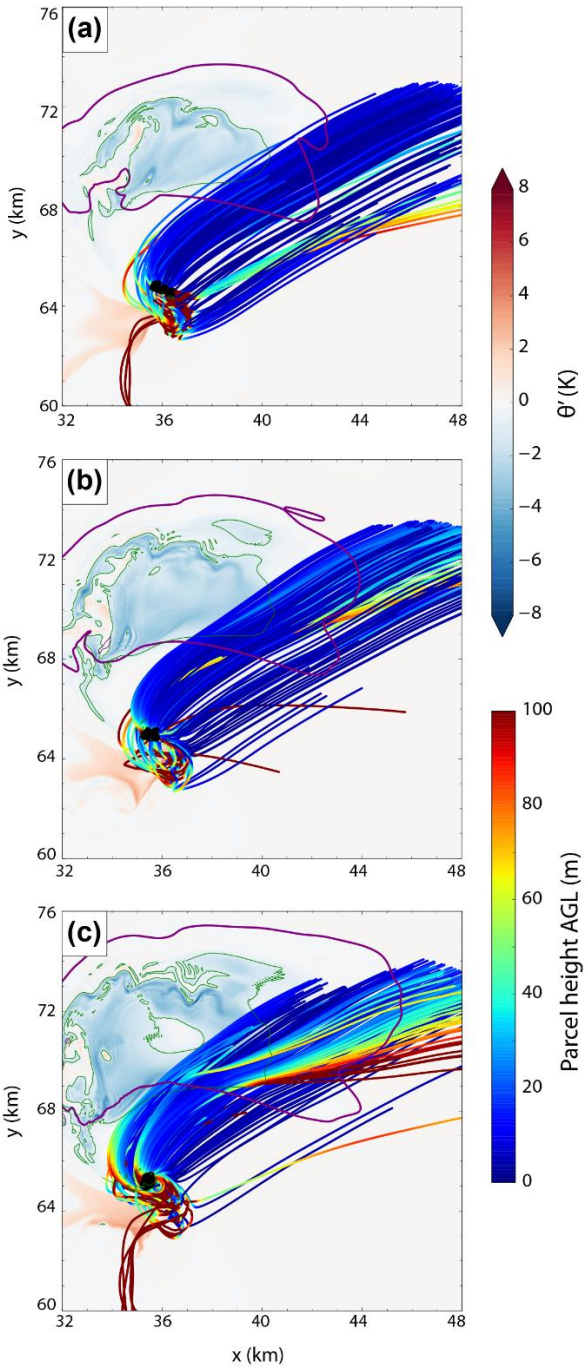

Fig. 3.9. Horizontal projection of trajectories initialized on a 1x1 km square grid centered on the PTV/tornado at 400 m AGL at (a) 1440 s, (b) 1500 s, and (c) 1560 s. Only trajectories with a final vertical vorticity value of $\zeta \geq 0.1$ s^{-1} are shown. The trajectories were integrated 900 s backward in time, and are color-coded by parcel height along the path, with a black dot denoting their final position in the PTV/tornado. For context, these trajectories are overlaid atop a horizontal cross-section (valid at the same time as the trajectory initialization in each panel) at 400 m AGL of perturbation potential temperature (shaded, with a green contour for -1 K) and the 0.3 g kg^{-1} rainwater mixing ratio contour (heavy purple contour).

Indeed, in the present study, agreement between Lagrangian and interpolated[7] values of the horizontal vorticity components is poor during times when parcels descend below the lowest scalar level (10 m AGL). Consequently, we require that a parcel remains above 10 m AGL at all times during the backward integration for it to be selected for quantitative analyses. Because of this, we initialize our backward trajectories at either 400 m or 600 m AGL within the vortex (where $\zeta \geq 0.1$ s^{-1}), since trajectories initialized at lower heights almost invariably originate from below 10 m AGL. Still, most these trajectories get very close to the lowest scalar level (10 m AGL) on their approach to the vortex.

Fig. 3.9a presents horizontal paths of trajectories entering the PTV at 400 m AGL at 1440 s. Parcels are found to originate almost exclusively from northeast of the vortex and below 100 m AGL, translating horizontally within this layer until ascending rapidly into the PTV at the end of the integration period. This distribution strongly favoring inflow trajectories from northeast of the vortex remains dominant at the time of tornadogenesis (1500 s, Fig. 3.9b) and even when the tornado is near its peak intensity (1560 s, Fig. 3.9c).

Dahl et al. (2012) (hereafter D12) investigated the accuracies of backward parcel trajectories that entered a low-level mesocyclone in two supercell simulations (using 250 m horizontal grid spacing, and ~100 m vertical spacing near the ground). It was found that as the time interval of the model velocity data used to calculate the trajectories increases, more backward trajectories enter the mesocyclone directly from

[7] In the context of trajectories in this study, "interpolated" refers to vorticity values interpolated directly from the model grid to the trajectory location; "Lagrangian" refers to values obtained through time integration of vorticity source terms along the trajectory (which themselves are also interpolated from the model grid).

the inflow without going through the downdraft region, a result which appeared to be erroneous in their simulation. The amplification of trajectory calculation errors initially created near the vortex (where flow curvature and velocity time tendencies are large) is believed to be the primary reason. In the present study, the model velocity data interval is only 2 s, but compared to the time it takes for a near-vortex parcel to travel one grid interval (about 0.5 s) it is still relatively large.

Because inflow trajectories are dominant in the present study, in order to test their accuracy, test trajectories are initialized in a grid pattern covering the area of origin suggested by the backward trajectories, then integrated forward in time. Note that these forward trajectories are integrated using the same 2 s data interval as the backward trajectories. D12 suggests that forward trajectories are inherently less prone to error amplification in regions of convergent flow, such as those flowing towards a tornado. Several of these forward test trajectories enter the tornado (not shown), and nearly all follow qualitatively similar paths toward the low-level mesocyclone when compared with the backward trajectories, increasing our confidence that the backward trajectories we analyze in this section are qualitatively reasonable. The thermodynamic and kinematic structure of the supercell in the present simulation differs markedly from the structure in D12; tornadogenesis occurs much earlier in the storm's evolution herein, before a precipitation-driven downdraft is well-established. Thus, it is plausible that inflow trajectories are dominant in the present study even if they are less prevalent in storms with well-established or stronger cool outflow, as in the case of D12. Indeed, Dawson et al. (2015) also found an inflow-dominant distribution of vortex-entering trajectories in a real-data simulation of the same 3 May 1999 case used as the basis for

our sounding. Still, based on the results of D12 and given the rapidly-evolving flow, we are less confident in the accuracy of the minority of our trajectories which enter along straight paths from due east of the vortex (most prominent at 1440 s) and will not include them in the analysis which follows.

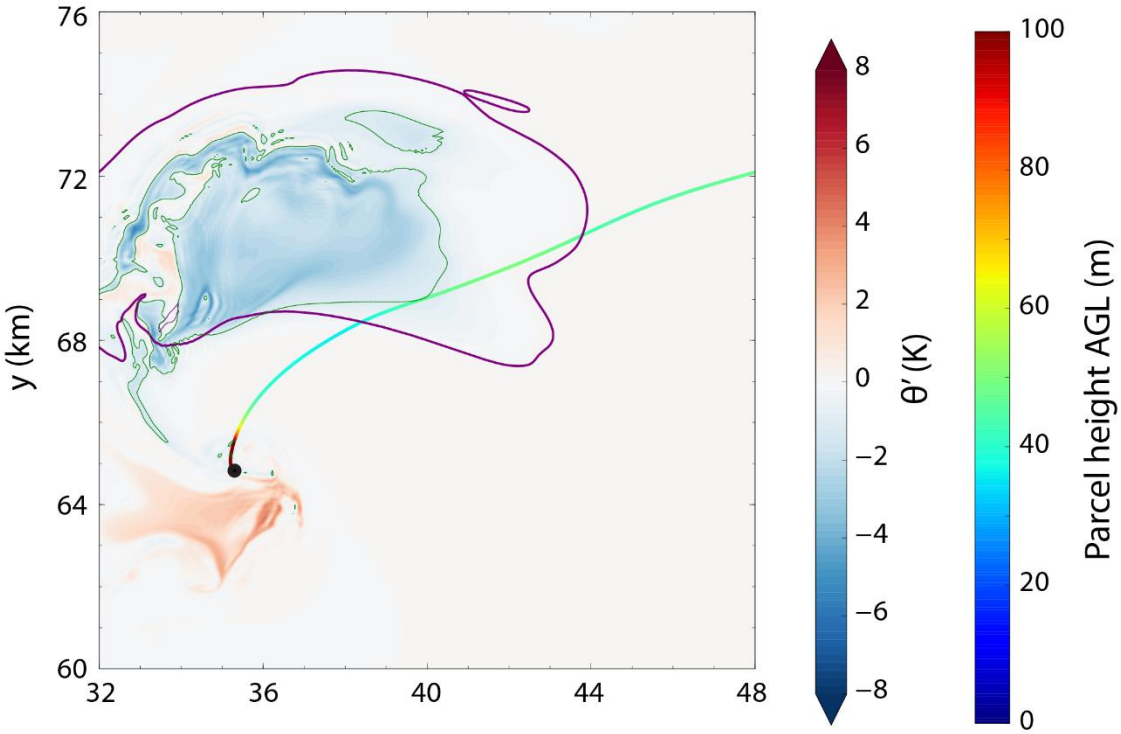

Fig. 3.10. As in Fig. 3.9b, but only the representative parcel (RP) trajectory (which enters the tornado at 1500 s) is shown.

A representative parcel (hereafter RP) which enters the tornado at 1500 s is chosen for the purpose of a detailed vorticity budget analysis. The horizontal path of the RP (Fig. 3.10) qualitatively resembles most of the tornado-entering trajectories valid at the same time in Fig. 3.9b. It originates from a height of approximately 50 m AGL at 600 s, remaining within ±20 m of that height throughout its approach until it begins ascending into the tornado after 1400 s.

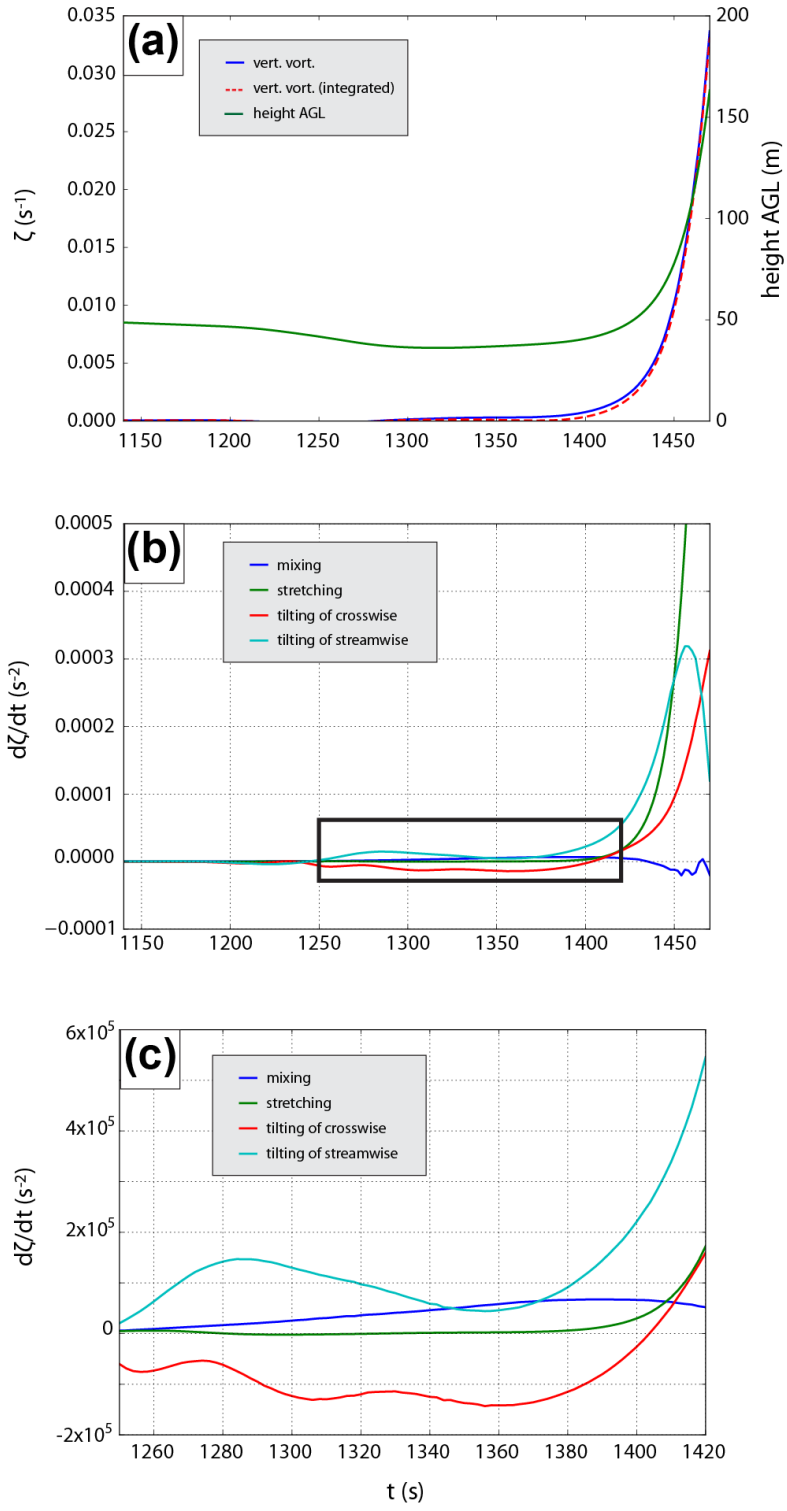

Fig. 3.11. Time series from 1140-1470 s along the representative parcel trajectory shown in Fig. 3.10, of (a) parcel height AGL, model predicted vertical vorticity (interpolated to the parcel locations), and vertical vorticity integrated from generation terms; and (b) vertical vorticity source terms. (c) A zoomed time series of source terms from 1250-1420 s. The period plotted in (c) is denoted by the black box in (b).

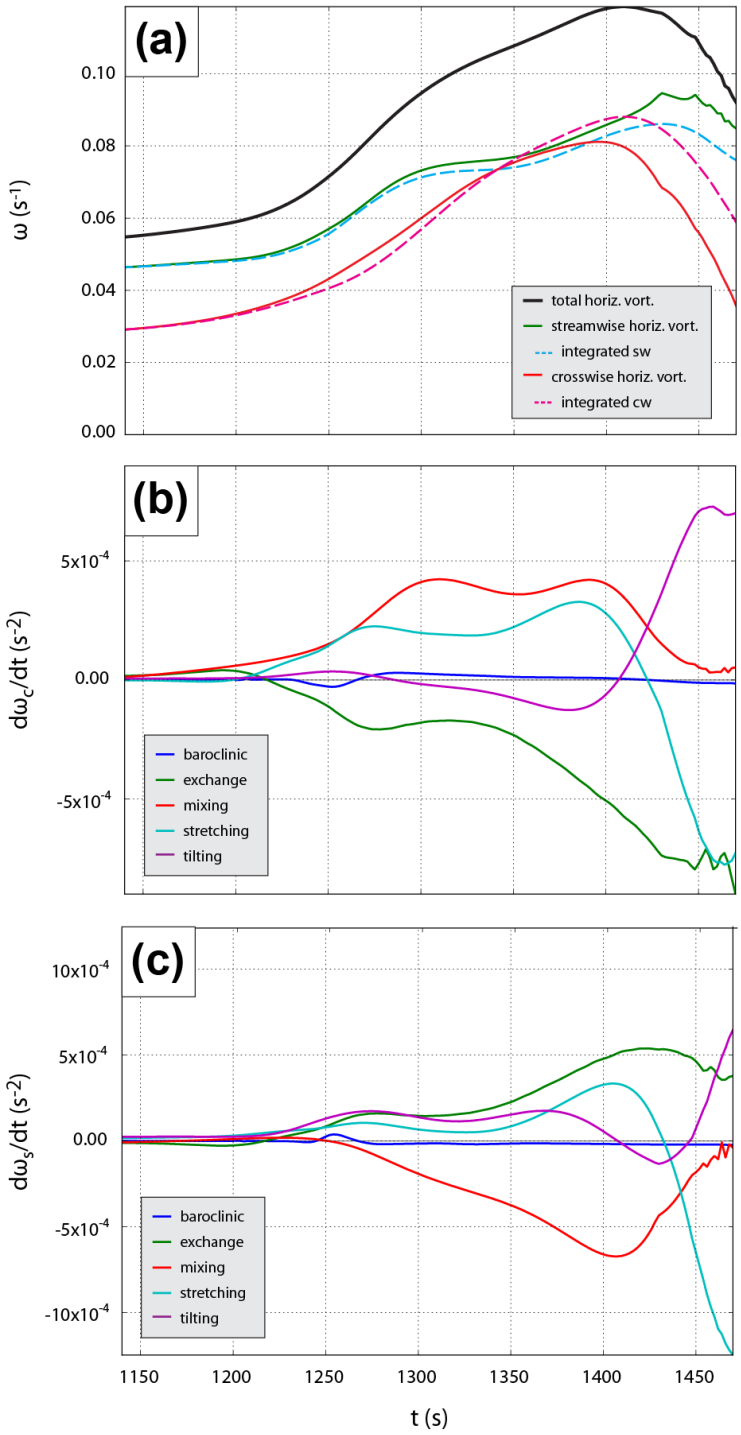

Fig. 3.12. Time series for the representative parcel trajectory from 1140-1470 s of (a) total horizontal vorticity, along with its streamwise and crosswise components (and their integrated values from source terms of the vorticity equations, in dashed lines); (b) horizontal crosswise vorticity source terms; and (c) horizontal streamwise vorticity source terms.

Of chief concern for the RP is the evolution of its vorticity components as it approaches the vortex, and particularly of the source[8] terms responsible for any significant changes in the magnitude or orientation of the vorticity. Fig. 3.11a presents an along-trajectory ζ time series for the RP between 1140-1470 s, while Fig. 3.11b depicts ζ source terms over the same period. Since the vorticity obtained by integrating the vorticity equation with its source terms along the trajectory agrees well with the vorticity interpolated to the trajectory from the model fields (Fig. 3.11a), we believe both the trajectory calculation and vorticity integration are very accurate for the RP.

It is apparent that after 1450 s, stretching is the dominant source of cyclonic ζ generation as the parcel ascends rapidly, leading the RP to acquire tornado-strength vorticity within the following minute. Because stretching can only act on existing vertical vorticity, the critical question becomes: which term(s) produced low-level cyclonic ζ prior to this amplification by stretching? Before stretching becomes dominant around 1450 s, tilting of streamwise[9] horizontal vorticity into the vertical is responsible for most of the positive ζ generation (Fig. 3.11c). By contrast, tilting of crosswise horizontal vorticity into the vertical has a negative contribution for much of this period before becoming weakly positive after 1380 s (Fig. 3.11c).

Because tilting of streamwise vorticity is the primary source of positive ζ for the RP, we want to identify the source of this streamwise vorticity. The prognostic

[8] We use "source term" in this paper to refer to any term which appears on the right-hand side of the prognostic equation for a vorticity component, e.g., of Eqs. (9) and (10). Some of these terms, such as the stretching and tilting terms, are not true sources of vorticity in the sense of new vorticity production, but represent the transport or reorientation of existing vorticity.

[9] All references to "streamwise" and "crosswise" hereafter are in the storm-relative framework (i.e., streamwise is considered to be in the direction of the local model-predicted wind).

equations for the streamwise horizontal vorticity ω_s and crosswise horizontal vorticity ω_c are, respectively:

$$\frac{D\omega_s}{\mathrm{Dt}} = \boldsymbol{\omega} \cdot \nabla \mathrm{V}_h + \frac{\partial \mathrm{B}}{\partial \mathrm{n}} + \frac{1}{\rho}\left(\frac{\partial F_z}{\partial \mathrm{n}} - \frac{\partial F_n}{\partial \mathrm{z}} - F_s \frac{\partial \psi}{\partial z}\right) + \omega_{hc} \frac{\mathrm{D}\psi}{\mathrm{Dt}}, \tag{3.9}$$

$$\frac{D\omega_c}{\mathrm{Dt}} = \boldsymbol{\omega} \cdot \mathrm{V}_h \nabla \psi - \frac{\partial \mathrm{B}}{\partial \mathrm{s}} + \frac{1}{\rho}\left(\frac{\partial F_s}{\partial \mathrm{z}} - \frac{\partial F_z}{\partial \mathrm{s}} - F_n \frac{\partial \psi}{\partial z}\right) - \omega_{hs} \frac{\mathrm{D}\psi}{\mathrm{Dt}}, \tag{3.10}$$

where $\boldsymbol{\omega}$ is the 3D relative vorticity vector; V_h is the horizontal wind magnitude; $\psi = \tan^{-1}(v/u)$ is the horizontal wind direction; B is the buoyancy (including the weight of hydrometeors); and F_s, F_n, and F_z are, respectively, the horizontal streamwise, horizontal crosswise, and vertical components of the frictional force[10]. In both (3.9) and (3.10), the right-hand side (rhs) terms represent, in order, generation by: stretching and tilting; baroclinity; friction/mixing; and exchange of vorticity between the streamwise and crosswise directions. Equations (3.9) and (3.10) are the same as those given in Mashiko et al. (2009) and S14, except that the last term involving $\frac{\partial \psi}{\partial \mathrm{z}}$ in the frictional term in both equations was missing in their papers. In the case of S14, this was simply an error in the written equations; the calculations used for vorticity budgets employed the correct formulation, and the same code was also used in the present study. Note that we neglect the effects of Coriolis in (3.9) and (3.10), since the time scale to produce tornado-strength vorticity from Earth's vorticity is much longer than our trajectory calculations (e.g., Davies-Jones 2014).

Time series of total (3D), crosswise horizontal, and streamwise horizontal vorticity for the RP between 1140 s and 1470 s are presented in Fig. 3.12a. Initially, the

[10] Note that the frictional force represents the combined effects of numerical diffusion and subgrid scale turbulence mixing. The frictional force is actually the result of turbulence momentum flux or stress tensor divergences and the surface drag enters the governing equations as the lower boundary condition of the vertical turbulence flux for momentum; see Section 3.1.1 for further details.

magnitude of the streamwise component is considerably larger than the crosswise component owing to the large, clockwise-curving hodograph of the background environment (c.f. Fig. 3.1). Between 1140 s and 1400 s, the total horizontal vorticity magnitude for the RP approximately doubles, and the parcel remains near 50 m AGL. During this pre-ascent period, the crosswise component of horizontal vorticity experiences a larger relative increase than the streamwise component. A time series of the horizontal crosswise vorticity source terms for the RP (Fig. 3.12b) reveals that the frictional mixing term is responsible for much of this increase, with stretching playing a secondary role (the flow accelerates horizontally before it gets very close to the convergence zone). The magnitude of crosswise mixing generation is largest between 1300-1400 s, then starts to decrease after 1400 s; partially as a result, the crosswise horizontal vorticity also begins to decrease after 1400 s. The loss of positive crosswise to streamwise vorticity through the exchange term is significant from 1220 s onward, and becomes much larger after 1400 s.

Fig. 3.12c shows that exchange of crosswise vorticity into the streamwise direction is the dominant source of positive generation for horizontal streamwise vorticity. The exchange term in Fig. 3.12c is maximized between 1400-1450 s, after the horizontal crosswise vorticity has reached its peak value, highlighting that horizontal vorticity initially created in the crosswise direction is converted to streamwise vorticity (especially when the parcel is close to the incipient tornado). Baroclinic generation of horizontal vorticity is negligible throughout the RP's approach.

Given that the RP is located around 30-50 m AGL (near the second grid level AGL) while the mixing term for crosswise vorticity is relatively large (Fig. 3.12b),

surface drag should be regarded as the dominant physical mechanism by which the mixing term generates crosswise horizontal vorticity (vorticity pointing to the left of the flow). Indeed, in the presence of surface drag, accelerating near-ground flow must experience negative stress from below that generates positive crosswise vorticity. Thus, a clear picture emerges for how horizontal vorticity becomes substantially larger than its environmental value and ultimately is tilted into the vertical.

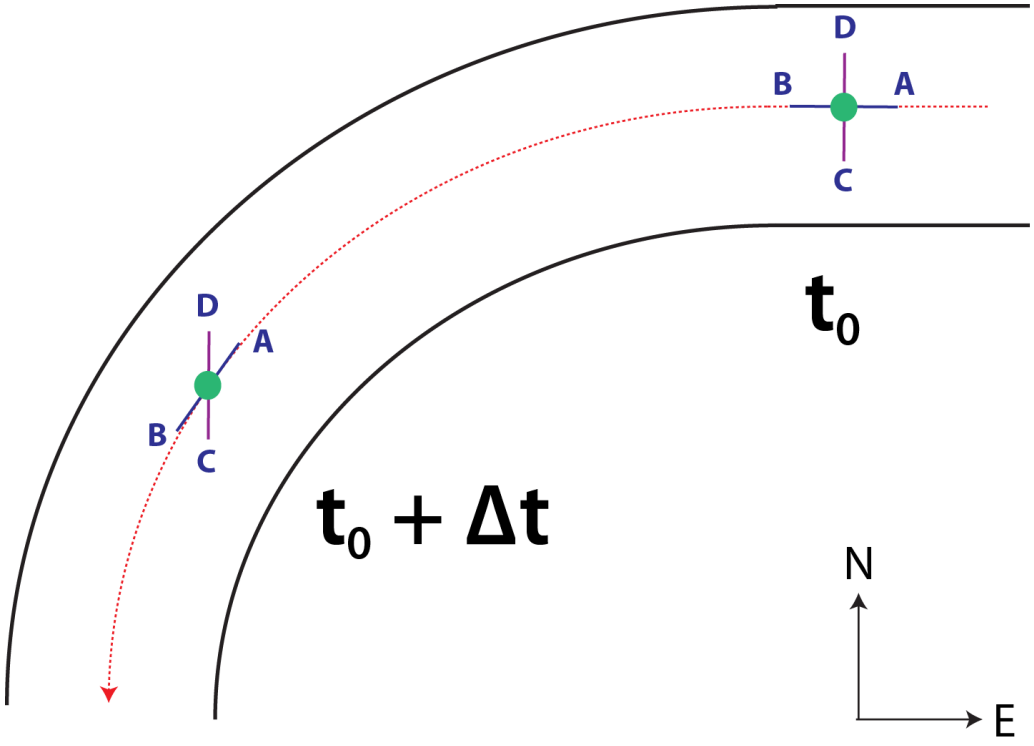

Fig. 3.13. Diagram of flow around a riverbend, demonstrating the development of streamwise vorticity from preexisting crosswise vorticity. The black curves represent the edges of the "river;" green circles represent the location of a representative parcel at times t_0 and $t_0+\Delta t$; red dotted arrow represents the streamline along which the parcel travels; purple line segment CD represents the vortex line in which the parcel lies; and blue line segment AB represents the parcel's instantaneous horizontal velocity vector. As the parcel enters the riverbend at time t_0, its horizontal vorticity is entirely crosswise. Because flow around the bend generates no vertical vorticity to a first approximation, AB and CD must rotate in opposite directions. Adapted from Davies-Jones et al. (2001) Fig. 5.15.

First, horizontal crosswise vorticity is generated by surface drag as the parcels originating from the inflow region accelerate near the ground and flow into the low-level convergence center along cyclonically curved paths (c.f. Fig. 3.9). Along the paths and especially as the parcels get close to the convergence center, a significant portion of this crosswise vorticity is exchanged into the streamwise direction. This exchange appears to be an example of the so-called "riverbend effect" described in Davies-Jones et al. (2001) whereby crosswise vorticity is converted to streamwise vorticity within cyclonically-curved flow (Fig. 3.13). Finally, as the parcels enter the convergence zone, horizontal streamwise vorticity is tilted into the vertical and the vertical vorticity is rapidly amplified through stretching as the parcels ascend (Fig. 3.11a). Very similar processes were found in the simulation of a real supercell storm in S14.

To ensure the representativeness of the vorticity budgets for the RP, vorticity source terms are calculated for a large sample of vortex-entering parcels; specifically, we analyze a subset (n=442 for 1440 s, n=694 for 1500 s, n=469 for 1560 s) of the parcels whose paths are displayed in Fig. 3.9. These parcels are initialized in a dense grid pattern (dx = 25 m) of size 1x1 km centered on the vortex at 400 m AGL, and those with $\zeta \geq 0.1$ s^{-1} at the initialization time are integrated backward in time for 900 s; this is the set of parcels plotted in Fig. 3.9. For our analysis, parcels which descend below 10 m AGL at any point in the integration are excluded from further analysis. We also exclude those parcels with $\zeta \geq 0.025$ s^{-1} at any time earlier than 60 s before initialization (to exclude parcels which were circling the vortex for an extended time, rather than entering it 60 s or less prior to our initialization time).

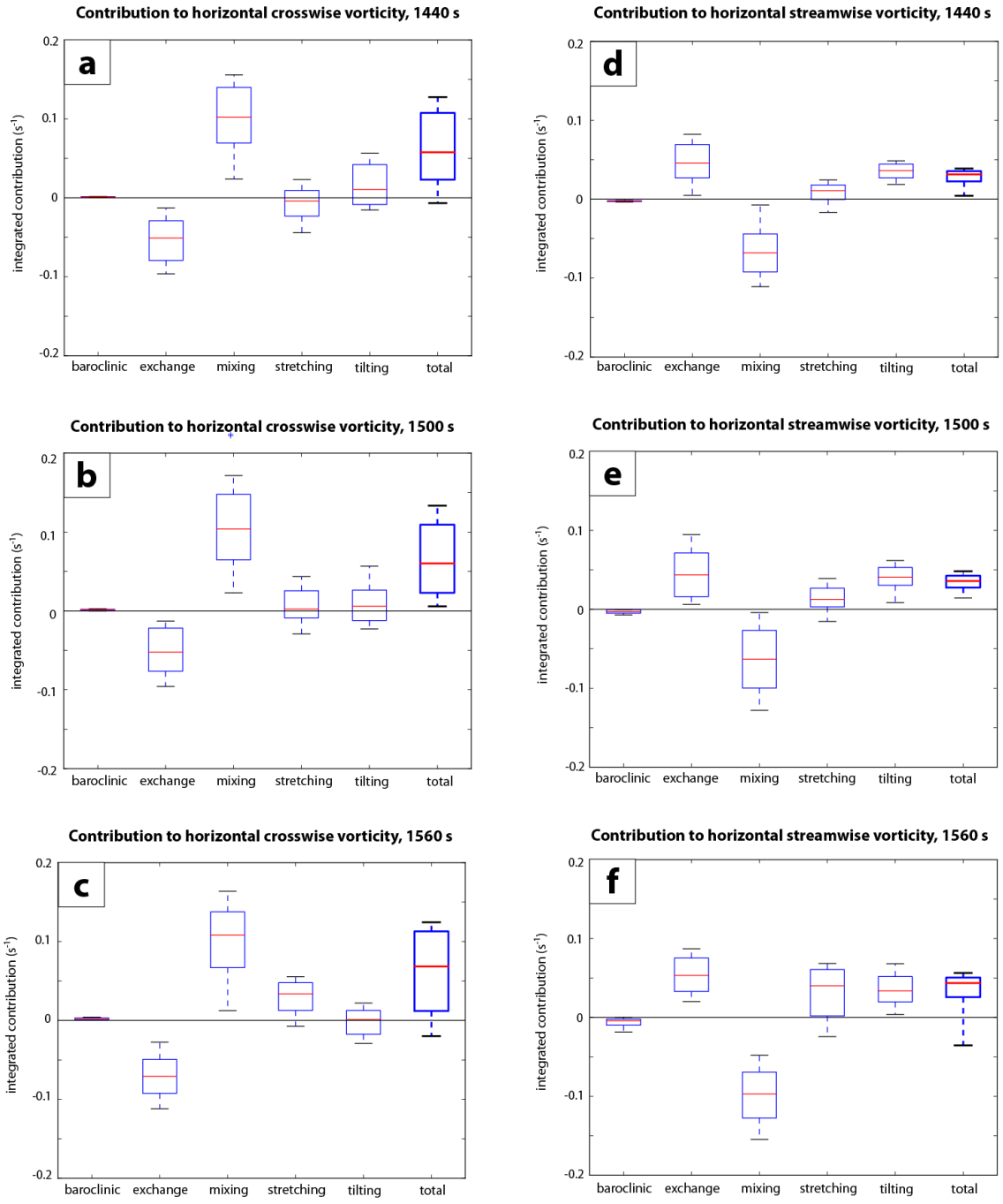

Fig. 3.14. Box-and-whisker plot of the time-integrated contributions of source terms to horizontal crosswise vorticity for parcels entering the (a) PTV at 1440 s, (b) tornado at 1500 s, and (c) tornado at 1560 s. (d-f) As in (a-c), except for horizontal streamwise vorticity. The terms are integrated beginning 900 s before, and ending 60 s before, the trajectories' initialization within the PTV/tornado (1440 s, 1500 s, and 1560 s, respectively). For each source term on a plot, the red line denotes the median value; the box encompasses the interquartile range; and the whiskers extend outward to the 10th (on the bottom) and 90th (on the top) percentile values.

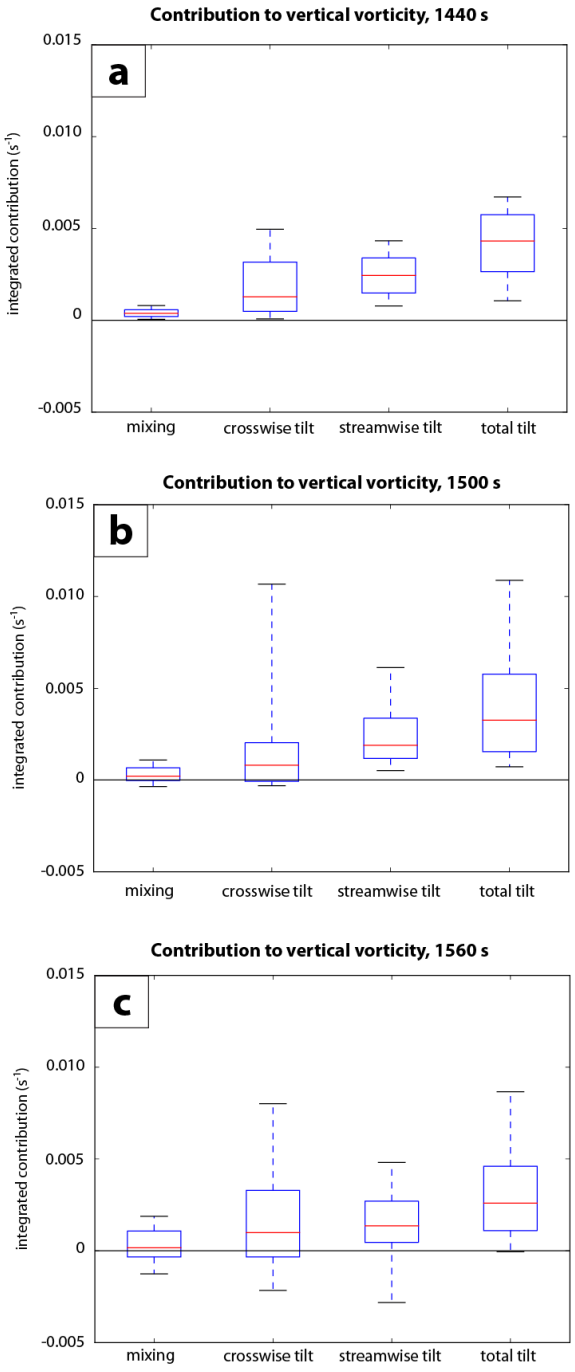

Fig. 3.15. Box-and-whisker plot of the time-integrated contribution to vertical vorticity for parcels entering the (a) PTV at 1440 s, (b) tornado at 1500 s, and (c) tornado at 1560 s. The plot details and time periods of integration are the same as described in Fig. 3.14.

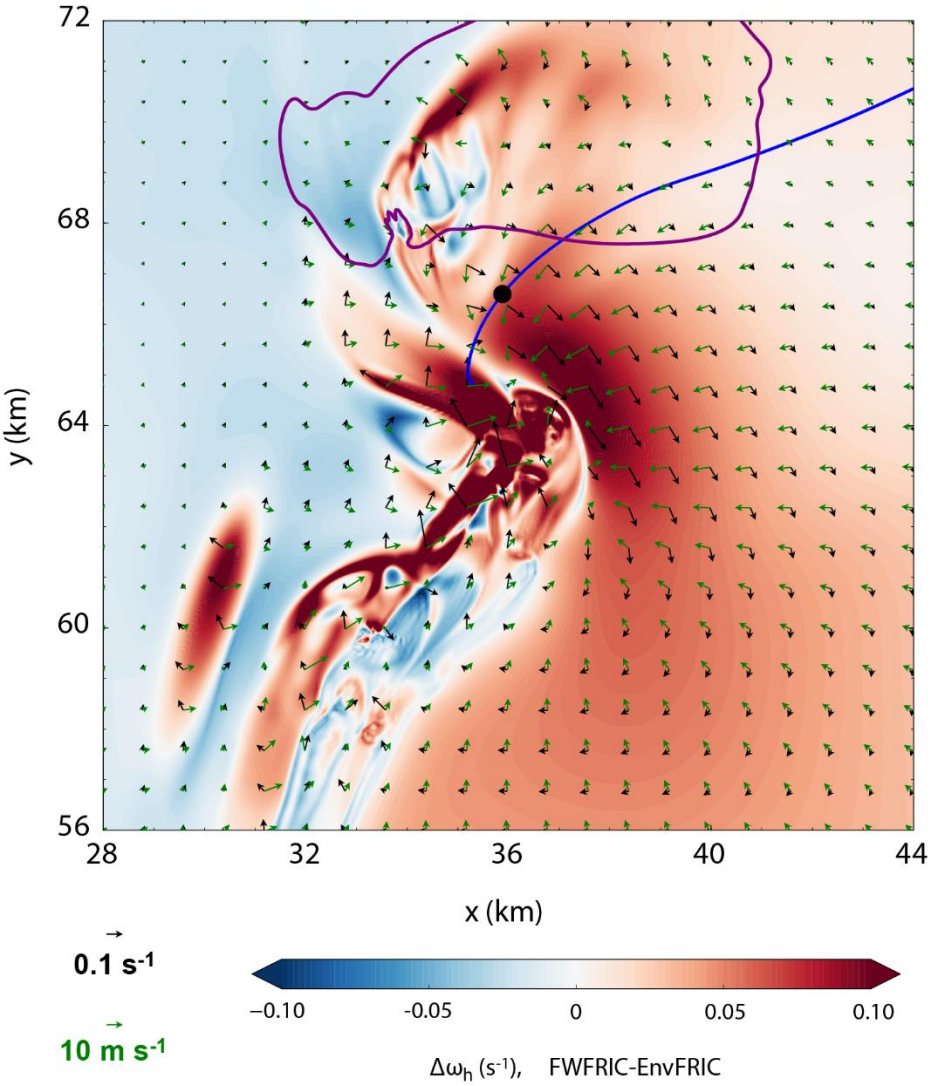

Fig. 3.16. Experiment difference fields (FWFRIC-EnvFRIC) at 1410 s for total horizontal vorticity at 10 m AGL (black vectors), with the magnitude shaded. Horizontal ground-relative wind vectors (green) for the FWFRIC experiment (*not* the vector wind difference) are overlaid for context. The heavy purple contour is the 0.3 g kg^{-1} contour for rainwater mixing ratio in FWFRIC, indicating the position of the precipitation-driven downdraft; the contour for EnvFRIC (not shown) is qualitatively similar. The horizontal path of the RP (which enters the tornado in FWFRIC at 1500 s) is overlaid as a blue curve; its position at 1410 s is denoted by the black dot.

Fig. 3.14 presents box-and-whisker plots for the time-integrated contribution of source terms to horizontal crosswise (a-c) and streamwise (d-f) vorticity; note that these values represent the *change* in vorticity owing to each term during the period beginning 900 s before initialization within the vortex, and ending 60 s before initialization. The

60 s before initialization is, on average, approximately the time at which stretching becomes the dominant source of cyclonic ζ generation for a parcel; we are interested in the vorticity evolution *before* stretching increases ζ exponentially[11]. For both horizontal crosswise and streamwise vorticity, and for all three trajectory initialization times, the signs of the median value for all five source terms agree with the terms presented for the RP; furthermore, their relative magnitudes are also qualitatively similar to those for the RP. In particular, mixing is the dominant source of positive crosswise generation, while exchange is the dominant source for positive streamwise generation. Baroclinic generation is at least an order of magnitude smaller than mixing and exchange in all cases.

Fig. 3.15 presents analogous box-and-whisker plots for source terms of ζ. For all initialization times, tilting of streamwise vorticity has a positive contribution to cyclonic ζ for at least 75% of the parcels. Tilting of crosswise vorticity also has a positive contribution to cyclonic ζ which tends to be smaller for most parcels, although it is quite large for a small minority of parcels. Thus, tilting of streamwise vorticity is an important source of vertical vorticity for virtually all parcels, while tilting of crosswise vorticity is also important for a smaller subset of parcels. It should be emphasized that the values in Fig. 3.15 represent an *integrated* contribution that includes a long period during which parcels are approaching the vortex from the far field. As such, a series of different physical processes occurring at different stages of a parcel's approach may be represented; for example, tilting of crosswise vorticity into cyclonic vorticity is unlikely

[11] Also, once a parcel enters the vortex, the horizontal source terms often become both large in magnitude and erratic; including the integrated contributions from this period can overwhelm the signal from the preceding physical processes we aim to quantify.

to occur within or very near the vortex[12], but may occur earlier during the parcel's approach. It is worth noting that among three pre-tornadic areas of vorticity preceding a tornado simulated in S14, one area of positive vertical vorticity (called V2 in their paper) mainly arose from the tilting of crosswise vorticity, suggesting that the role of the direct tilting of crosswise vorticity can be case-dependent. In general, Fig. 3.14 and Fig. 3.15 instill confidence in the conclusions we obtain based on the analyses of the RP, and similar processes appear to persist from the PTV stage (1440 s) through the mature tornado stage (1560 s).

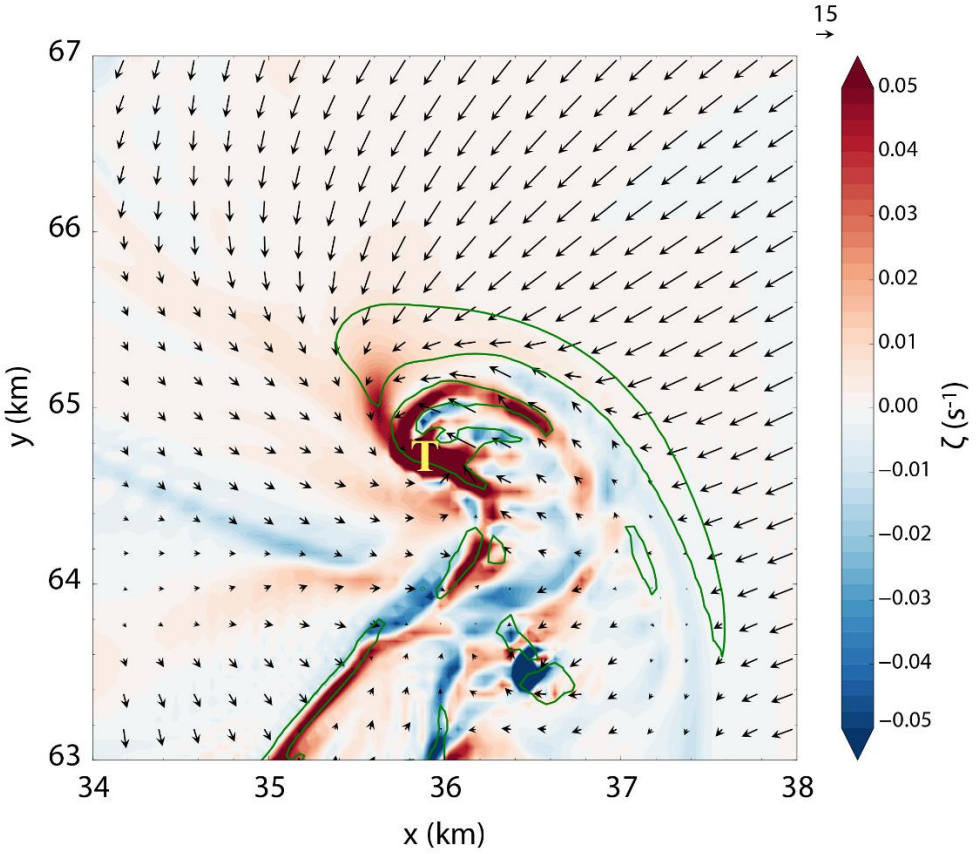

Fig. 3.17. Vertical vorticity (shaded), 0.05 s^{-1} horizontal convergence contour (green), and storm-relative horizontal wind vectors at 10 m AGL and 1500 s in FWFRIC. Tornado location is denoted by the yellow "T."

[12] It should be expected that most of the parcel's horizontal vorticity is streamwise as it ascends into the tornado. In the case of substantial crosswise vorticity, a dipole of cyclonic and anticyclonic vorticity would be expected instead of the strong cyclonic vortex which occurs in FWFRIC.

Fig. 3.16 presents the total horizontal vorticity vector difference between the two experiments (FWFRIC-EnvFRIC) at 10 m AGL and 1410 s (PTV stage), with the horizontal path of the RP and the horizontal wind vectors from FWFRIC overlaid for context. It is apparent that the horizontal vorticity magnitude is substantially larger in FWFRIC than in EnvFRIC throughout most of the low-level mesocyclone, and the difference vectors are predominantly crosswise. The RP, along with a large majority of the tornado-entering trajectories in Fig. 3.9, pass through the northwestern extent of this frictionally-enhanced vorticity region during the final several minutes of their approach to the vortex.

Fig. 3.17 presents the vertical vorticity field at 10 m AGL at 1500 s in the region immediately surrounding the incipient tornado. At least two "feeder bands" of enhanced vertical vorticity, analogous to those presented in D14 and Nowotarski et al. (2015), can be seen extending radially outward to the north from the vortex. The leftmost band, which protrudes northwestward from the tornado, is a persistent feature feeding into the PTV at 10 m AGL for at least 180 s prior to tornadogenesis (not shown). Its location corresponds to the area through which many of our vortex-entering parcels translate along the ground during the 60-120 s immediately prior to ascending, providing evidence that even parcels which enter the vortex at lower heights than our trajectories (i.e., below 400 m AGL) are gaining cyclonic vorticity near the ground as they approach. This helps to bolster confidence that our vorticity budgets for vortex-entering parcels at 400-600 m AGL should qualitatively resemble those for parcels entering the vortex at heights closer to the ground. The cyclonic vorticity in the "feeder bands"

likely originates from the tilting of horizontal vorticity primarily generated by friction as parcels approach the developing tornado, based on our earlier analysis.

3.2.3 Origin of near-ground vertical vorticity

To this point, our trajectory analysis has addressed the dominant sources for tornadic vorticity in FWFRIC; we now turn our attention to a slightly earlier time in the simulation to examine the initial development of cyclonic ζ near the ground. In the absence of pre-existing vertical vorticity, horizontal vorticity generated by surface drag, baroclinity, or any other mechanism must be tilted into the vertical before it can be stretched into tornado intensity. Davies-Jones (1982) (hereafter DJ82) argued that in the absence of an extreme preexisting horizontal gradient of vertical velocity (*w*), tilting of horizontal vorticity by an updraft alone cannot produce tornado-strength ζ near the ground, as the tilting occurs while parcels move away from the ground. This thinking has influenced subsequent studies concerning tornadogenesis dynamics and was reiterated by Davies-Jones and Markowski (2013), who demonstrated numerically and analytically the inefficiency of upward vorticity tilting near the ground even for their "worst-case scenario" with strong baroclinity and abruptly-changing *w* along a gust front. In the present study, much of the cyclonic ζ generation by tilting occurs during ascent into the vortex. However, nearly all vortex-entering parcels experience a shallow descent (on the order of 10 m vertical displacement) several minutes prior to entering the vortex, which we will now analyze. Fig. 3.18a presents a time series of ζ and height AGL for the RP between 1140-1380 s. The parcel descends gradually from 48 m AGL to 36 m AGL between 1140-1320 s. While a tendency toward anticyclonic ζ is evident initially, this trend reverses around 1260 s, after which time cyclonic ζ generation

continues through the remainder of the descent. Crucially, the increase in ζ seen in Fig. 3.18a from 1260 s onward does not await ascent into the vortex, but instead begins during this shallow descent[13].

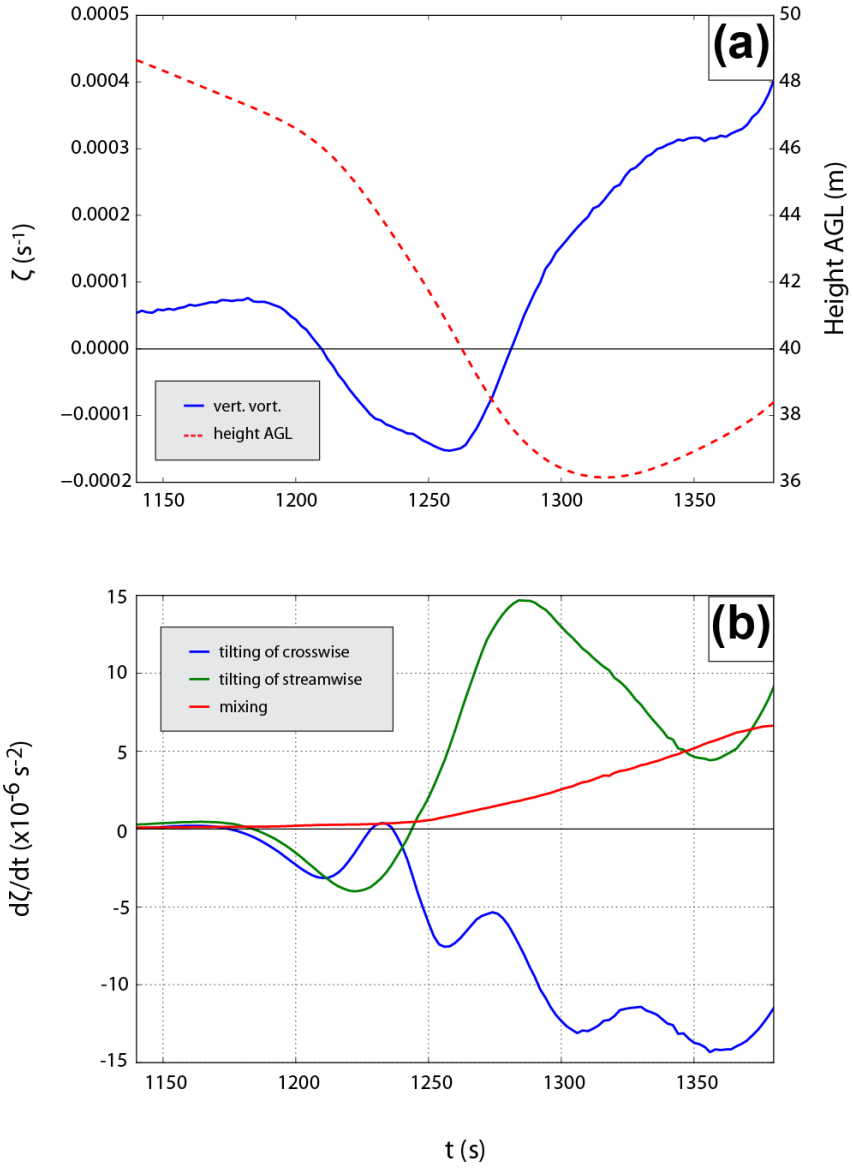

Fig. 3.18. Along-trajectory time series for the RP of (a) vertical vorticity (solid blue) and height AGL (dashed red), and (b) vertical vorticity generation owing to tilting of crosswise vorticity (blue), tilting of streamwise vorticity (green), and mixing (green). The time series is from 1140-1380 s.

[13] While the parcel does not acquire large cyclonic vorticity ($\zeta > 0.01$ s^{-1}) until its ascent is underway, cyclonic vorticity initially develops near the ground during descent, allowing for subsequent amplification by stretching.

A time series of ζ source terms between 1140-1380 s is presented in Fig. 3.18b. Early in the descent period, between 1180-1240 s, tilting of both streamwise and crosswise components result in a negative time tendency for ζ. However, the streamwise term becomes positive around 1240 s and increases in magnitude thereafter until around 1300 s. The crosswise term remains negative and also increases in magnitude, but its magnitude is smaller than the streamwise term from 1250-1300 s. Thus, during the RP's descent, it is primarily tilting of the streamwise component of horizontal vorticity which enables the development of cyclonic ζ, with mixing generation playing a secondary role (details of which are left for future work).

If the RP's vorticity during descent owed its existence entirely to the background environmental wind shear (which is associated with purely horizontal vorticity that is predominantly streamwise near the ground), one would not expect cyclonic ζ to develop until the parcel reached its nadir and began ascending[14]. However, in Fig. 3.18a, ζ first becomes cyclonic around 1280 s as descent is still ongoing. This suggests horizontal streamwise vorticity is being generated during descent. Davies-Jones and Brooks (1993) (hereafter DB93) described a mechanism by which "slippage" of vortex lines with respect to the parcel trajectory allows ζ to develop during descent. In DB93, baroclinic generation of streamwise horizontal vorticity acts to "peel" a vortex line passing through the parcel upward off the local streamline during descent, which in turn allows the surrounding flow to increase the inclination angle of the vortex line via tilting. In this way, cyclonic ζ may develop during descent. More recently, S14

[14] In the approximation of inviscid, steady flow subject only to conservative body forces, Helmholtz's first vorticity theorem states that vortex lines are material lines. As such, initially streamwise parcel vorticity cannot be tilted upward while the parcel is descending, as this would require the vortex line through the parcel to separate from its original material line.

identified an analogous effect which relies upon initially-crosswise frictionally-generated vorticity that is subsequently exchanged into the streamwise direction. The authors of S14 did caution that while evidence for a dominant frictional role was compelling for their case, the limited time window of their vorticity budgets left open the possibility of important baroclinic generation (as described by DB93) earlier in the parcel's history. In the present study, it is clear from Fig. 3.12c that baroclinic generation is negligible relative to other terms throughout the RP's descent. Instead, Fig. 3.12b and c suggest the S14 mechanism whereby horizontal crosswise vorticity is generated frictionally and then exchanged into the streamwise direction as the parcel curves cyclonically. This generation of new horizontal streamwise vorticity allows the parcel's vorticity vector in the streamwise-height plane to peel upward off the trajectory during the early part of the RP's descent period (via tilting), and ultimately gain a cyclonic component later in the period (Fig. 3.19). By the time the parcel reaches its nadir, cyclonic ζ is already established. Regarding the role of baroclinic vorticity generation, the tornado forms in FWFRIC before a strong cold pool is established, increasing our confidence that it did not play a substantial role in tornadogenesis in this simulation.

Details of the formation of the weak downdraft traversed by vortex-entering parcels are left for future work. Many vortex-entering trajectories (including the RP) briefly traverse the first precipitation to reach the ground for a period of 30-60 s, coincident with their steepest period of descent; nonetheless, the RP never encounters cold outflow ($\theta' < -1$ K) during its approach to the tornado.

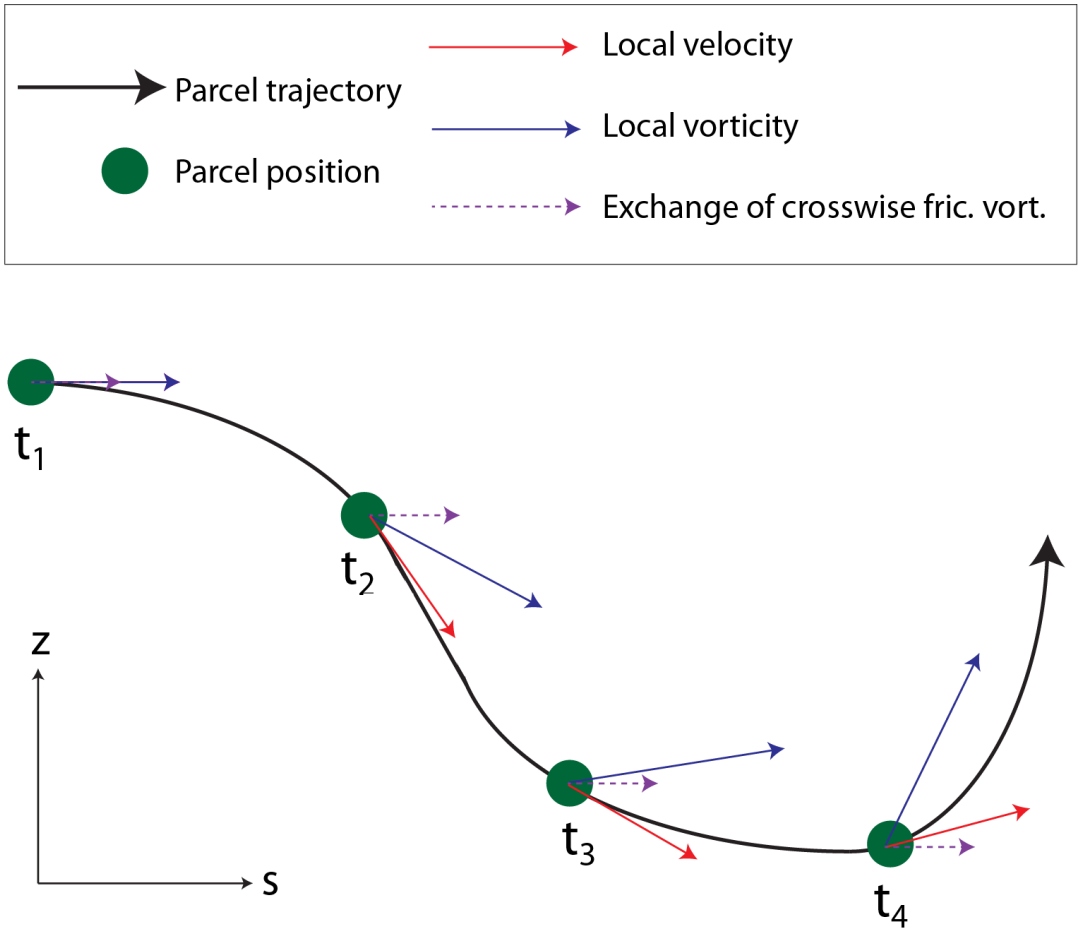

Fig. 3.19. Conceptual schematic depicting the evolution of parcel vorticity along a descending, vortex-entering trajectory. At times t_1 through t_4 (higher subscript indicates later in time), the parcel position (green dot), local velocity vector (solid red), local vorticity vector (solid blue), and local vorticity generation by crosswise-streamwise exchange (dashed purple) are illustrated in the s-z plane. Between t_1 and t_3, the change in the trajectory-relative vorticity vector is due to the generation of new horizontal streamwise vorticity (primarily the exchange of frictionally-generated horizontal crosswise vorticity into the streamwise direction by the riverbend effect). Tilting during descent allows the vorticity vector to acquire a vertical component. Note that the vorticity and vorticity generation vectors represent projections into the s-z plane and neglect any crosswise component. Note also that the vorticity generation denoted by the dashed purple vectors is due to the conversion of initially-crosswise vorticity (generated directly by friction) into streamwise vorticity via the riverbend effect.

3.3 Summary and conceptual model

In two idealized supercell experiments differentiated solely by the surface drag formulation, a strong tornado develops only in the experiment where the surface drag is

applied to the storm-induced perturbation wind field. In the experiment with drag applied only to the background environmental wind, transient and shallow vortices develop along a convergence boundary, but no sustained tornado develops. Based on the analysis of the simulations, a conceptual model that highlights the possible roles of surface friction in tornadogenesis through three mechanisms is proposed (Fig. 3.20):

Mechanism I: Generation of near-surface horizontal vorticity in the environment. The existence of surface drag creates substantial background environmental wind shear at the low levels, especially within the lowest 200 m AGL. Associated with this shear is large horizontal vorticity, which can be tilted into the vertical and stretched to produce a low-level mesocyclone. This horizontal vorticity can also contribute to the vorticity within a tornado when a low-level inflow parcel eventually enters the tornado vortex. This frictional effect acts primarily on the synoptic scale, impacting the storm environment by creating an Ekman spiral type wind profile in the boundary layer.

Mechanism II: Generation of near-surface horizontal vorticity within and around the convective storm. Surface drag locally enhances horizontal vorticity within the lowest 100 m AGL within the convective storm and in the vicinity of the low-level mesocyclone. Here, horizontal accelerations associated with strong low-level convergence underneath the storm updraft enable surface drag to generate new horizontal crosswise vorticity. The vortex-entering parcels typically have cyclonically-curved paths during their approach to the mesocyclone, and crosswise vorticity is continuously exchanged into the streamwise direction via the "riverbend effect;" this vorticity can subsequently be tilted into the vertical and be stretched. For descending

parcels, such tilting into the vertical can occur even before they reach their minimum height, creating cyclonic vorticity before the trajectory turns abruptly upward (very near the ground, in some cases). The tilting of frictionally-generated horizontal vorticity into the vertical can also contribute to the enhancement of the low-level mesocyclone in the pre-tornadic phase; the mesocyclone and associated low-level updraft in turn modulate the above processes.

Mechanism III. Enhancement of low-level convergence beneath the mesocyclone. During the development of the low-level mesocyclone, a stronger and more concentrated region of low-level convergence is found in the presence of surface drag. This strengthens the low-level updraft, setting up a favorable configuration for stretching to amplify cyclonic vorticity to tornado strength. This mechanism also acts on the storm scale.

Mechanism I is inherent in the friction-balanced sounding used to initialize both EnvFRIC and FWFRIC, and thus operates in both. By contrast, Mechanisms II and III each require surface drag to operate on storm-generated perturbation wind components, and thus are present only in FWFRIC. Because a strong tornado develops in FWFRIC while only a brief, sub-tornadic vortex develops in EnvFRIC, we conclude that some combination of Mechanisms II and III is responsible for instigating tornadogenesis in this case. In fact, both processes may be *necessary* for the tornado to form in FWFRIC. One fortuitous property of these results is that the tornado develops quite early relative to the parent supercell's lifecycle. At this early stage, discrepancies between the model fields in FWFRIC and EnvFRIC are still minor away from the low-level mesocyclone; nonlinear effects have not yet amplified these discrepancies into important differences

at the storm scale. As a result, comparison between the results of the two experiments is relatively straightforward and can confidently be attributed to the difference in friction.

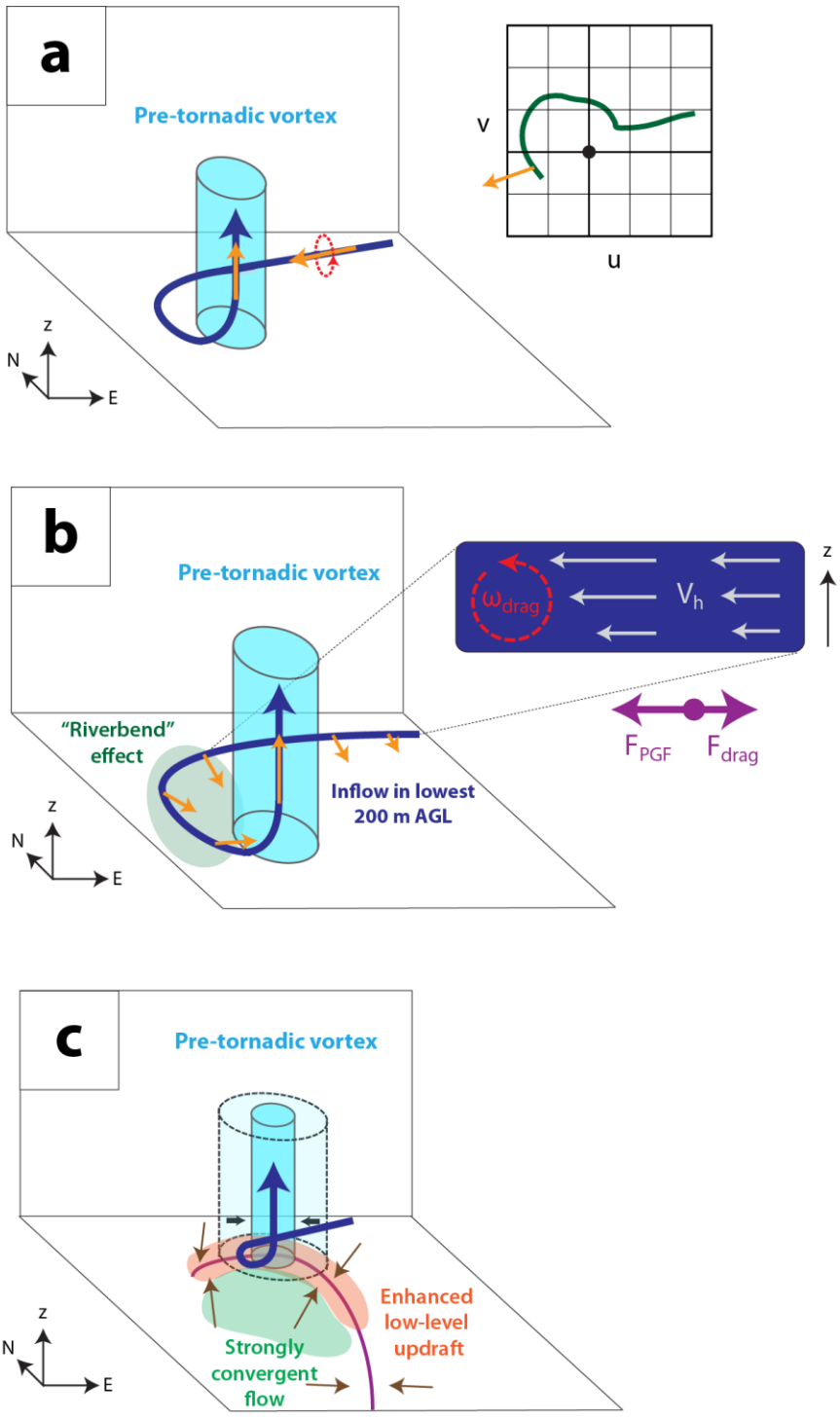

Fig. 3.20. Schematic illustrating physical mechanisms by which drag influences tornadogenesis in FWFRIC: (a) Mechanism I, (b) Mechanism II, and (c) Mechanism III.

For all three panels, the heavy dark blue curve with arrow is a representative storm-relative parcel trajectory entering the PTV below 500 m AGL. In (a), orange vectors are environmental vorticity vectors, with an accompanying red rotational vector denoting the sense of rotation; subplot on right is a representative storm-relative environmental hodograph (green) and associated near-ground vorticity vector (orange). In (II), orange vectors are the frictionally-generated vorticity vectors along the trajectory; for inset vertical cross-section on right, gray vectors represent horizontal wind, dashed red rotational arrows denote sense of vorticity, and purple arrows denote forces acting upon a parcel. In (III), purple curve denotes the low-level convergent boundary; the larger light blue cylinder (enclosed in dashed lines) is PTV at some initial time, while the narrower medium blue cylinder (enclosed in solid lines) is PTV at some later time; inward-pointing black arrows denote contraction of vortex with time; beige arrows denote low-level horizontal flow; orange shading denotes enhanced low-level updraft above the boundary; green shading denotes the region of more convergent flow towards the boundary in presence of surface friction.

Of notable absence is baroclinic vorticity generation as an important mechanism for vortex-genesis in our case. In fact, backward trajectories for parcels entering the tornado incur negligible baroclinic generation of horizontal vorticity during their approach. This result should be interpreted as evidence that a combination of environmental and locally-generated frictional horizontal vorticity potentially *can* be sufficient for tornadogenesis under certain circumstances. This does not, however, preclude the likely existence of other modes for supercell tornadogenesis; indeed, it should be expected that the mechanisms for tornadoes forming within more mature storms featuring well-developed RFDs will differ at least in some details, including the role of baroclincally-generated vorticity. Even so, this study corroborates the mechanism identified in S14 in which horizontal vorticity generated by surface drag can be a significant or even dominant contributor to tornadic vorticity. Note that even in our case, where baroclinic vorticity is shown to play a negligible role in tornadogenesis, a downdraft (albeit shallow) is still necessary for developing meaningful cyclonic vorticity very close to the ground. It is also worth noting that Markowski et al. (2015) recently presented preliminary results from highly idealized “toy model” pseudo-storm

simulations that included drag. One of their simulations produced an early tornado away from the cold pool with striking similarities to the tornado in FWFRIC herein; tilting of frictionally-enhanced horizontal vorticity by a downdraft near the ground (speculated to represent "compensating subsidence" on the periphery of the updraft) was implicated in vortex-genesis.

In FWFRIC, the tornado formed very quickly, and at a large distance from any precipitation or baroclinic gradients: while such occurrences may be atypical among observed supercell tornadoes, they are not without precedent. For example, Palmer et al. (2011) documented a strong tornado (denoted "B2" in their Fig. 7a) during the 10 May 2010 Oklahoma outbreak located several kilometers east-southeast of the parent storm 35 dBZ reflectivity contour which occurred within 30 min of the storm's first radar echoes. For some cases with a similar apparent lack of baroclinic vorticity, preexisting cyclonic ζ in the local environment (e.g., associated with a surface boundary or low pressure center) could plausibly be an important source of tornadic vorticity. In our idealized simulations, however, no such direct sources of vertical vorticity exist in the pre-storm environment. Perhaps given sufficiently strong low-level shear and/or surface roughness, tornadoes qualitatively similar to the tornado in FWFRIC can develop in the real world, even if they do not represent the most common mode of supercell tornadogenesis.

In order to highlight potential influences of drag upon tornadogenesis, we deliberately chose a drag coefficient C_d = 0.01 which is a relatively large value over land. Furthermore, in our simulation, the subgrid-scale turbulence mixing is parameterized by a 1.5-order TKE closure scheme at a large-eddy simulation (LES)

resolution. As described by Mason and Thomson (1992) and Brasseur and Wei (2010), LES turbulence schemes tend to overestimate the velocity gradient near a rigid wall (in this case, the vertical gradient of horizontal velocity at the lowest few grid levels above ground). With these considerations in mind, it is probable that our simulations exaggerate the effect of drag to some extent, relative to a typical supercell case over land. The quantitative treatment of surface drag and near-surface turbulence mixing will require further research. Still, qualitatively, we believe the effects of surface drag on tornadogenesis investigated herein should be valid.

This study uses two idealized experiments to illustrate mechanisms by which surface drag *can* instigate tornadogenesis, so additional work is needed to clarify these mechanisms' relative importance and under which conditions they operate most effectively. When a classical precipitation-loaded RFD is present and tornado-entering parcels traverse regions of significant baroclinity, will storm-scale frictional generation still be a dominant source of tornadic vorticity? Is there a threshold on the drag coefficient required for Mechanisms II and III to enter a positive feedback cycle that produces a sustained tornado? How, if at all, do the qualitative results presented herein change when a much finer vertical grid spacing is used near the ground? What were the primary forces driving the descent and ascent of the vortex entering parcels? These are some of the questions which will be addressed in future work.

Chapter 4 The Role of Surface Drag in Mesocyclogenesis Preceding Tornadogenesis[15]

4.1 Methodology

This study is an extension of the analysis in Chapter 3 and utilizes data from the same simulations, FWFRIC and EnvFRIC, described therein. Details of the model configuration and experimental design are found in Section 3.1. As a brief summary, the simulations are conducted using the Advanced Regional Prediction System (ARPS) (Xue et al. 2000; Xue et al. 2001) on a grid with 50-m spacing in the horizontal. The vertical grid is stretched, with a grid spacing of 20 m near the ground that increased to 400 m above 10 km AGL. The initial condition is horizontally homogeneous, except for an artificial thermal bubble near the center of the domain used to instigate deep moist convection.

The background sounding is based on a sounding used by Dawson et al. (2010) (hereafter DA10); it was extracted from a real data 3-km simulation of the 3 May 1999 tornado outbreak in central Oklahoma, as documented in Dawson et al. (2015) (hereafter DA15). This sounding is further modified such that the wind profile is in a three-force balance among the horizontal pressure gradient force (PGF), Coriolis force, and parameterized surface drag in the model. The procedure used to attain this balance and its implications were described at length in Section 3.1.2. In summary, the original sounding profile used in DA10 (hereafter, this sounding profile is referred to as MAY3) is used to initialize a 1D column run in ARPS with surface drag enabled and the drag

[15] Adapted from publication: Roberts, B., and M. Xue, 2017: The Role of Surface Drag in Mesocyclone Intensification Leading to Tornadogenesis within an Idealized Supercell Simulation. *J. Atmos. Sci.*, in press.

coefficient C_d = 0.01, as in the full 3D experiments of Chapter 3 (whose data are further analyzed in this paper). The 1.5-order TKE-based subgrid-scale (SGS) turbulence mixing parameterization is also used, as in the full 3D simulations (note that the original extracted sounding profile had already been subject to the 1.5-order TKE-based PBL parameterization mixing in the 3-km real data simulation, as described in DA15). The column run is integrated for 48 h in order for the profile to reach a steady state that is in a three-force balance (among the horizontal PGF, Coriolis and internal frictional forces). The final profile at the end of this run (hereafter MAY3B) is used to initialize the 3D simulations in Chapter 3. As discussed in Chapter 3, one drawback of this methodology is that it effectively assumes the wind profile in MAY3 is geostrophic. In Section 3.1.2, we estimated that the 0-1 km storm-relative helicity (SRH) in profile MAY3B is approximately 20% larger than it would have been had the 1D column run been initialized with a better-estimated (but unknown) geostrophic wind profile.

As described in Chapter 3, in the ARPS model, the surface drag comes into the model in the form of horizontal momentum stresses defined at the ground surface (Eqs. (3.1) and (3.2)), and the parameterized stresses are proportional to the drag coefficient C_d, the surface wind speed, and the wind component that the stress acts on. Such parameterized stresses at the lower boundary replace stress tenors that would otherwise be calculated using the SGS turbulence parameterization scheme; therefore, they serve as the lower boundary conditions for the vertical fluxes of horizontal momentum within the turbulence mixing terms of the horizontal momentum equations. The effects of surface drag are propagated upward into the flow mainly through the turbulence mixing terms, which can also be called the internal frictional force.

The sole difference between experiments FWFRIC and EnvFRIC lies in the formulation of parameterized surface drag. In FWFRIC, surface drag is proportional to the full ground-relative wind speed; i.e., the drag acts on the full wind, including any perturbation wind introduced by the convective storm. In EnvFRIC, however, surface drag is only applied to the environmental base-state wind (defined by our initial balanced sounding); it does not act on perturbation winds induced by the simulated storm. The drag in EnvFRIC therefore acts strictly to maintain the three-force balance implicit in the environmental sounding, while leaving storm-induced perturbation wind unaffected. The direct effect of surface drag on the simulated storm itself is excluded in EnvFRIC. More discussions on this methodology can be found in Section 3.1. In practical terms, FWFRIC is designed to illustrate how the simulated storm evolves when drag acts as it does in nature, while EnvFRIC is designed to illustrate how the storm evolves when drag only acts to create the background wind profile.

It should be noted that given the grid spacing we use (50-m in the horizontal and 20-m in the vertical near the ground), our simulations are essentially large eddy simulations (LESs). The 1.5-order TKE-based SGS-turbulence mixing scheme within ARPS, that is primarily based on Moeng and Wyngaard (1988), is therefore appropriate for our simulations. The mixing terms act to propagate the effects of surface drag into the flow interior, and appear as fictional force terms on the right hand side of the horizontal momentum equations. It is known that SGS turbulence closure schemes in LES often have issues near a rigid wall as the turbulent eddies become increasingly smaller near the wall; a special near-wall stress model has been designed to deal with such issues (Chow et al. 2005), but is not yet in common use for convective storm

simulations such as those in the present study. Mason and Thomson (1992) show that typical LES schemes often overestimate the gradient of parallel velocity components near a rigid wall; this suggests that the vertical shear of the horizontal wind very close to the ground (the lowest 50 m AGL or so) may be overestimated somewhat in our simulation, but we believe the results obtained in this study should still be qualitatively valid. We also note that Markowski and Bryan (2016) (hereafter MB16) examine potential problems in LES simulations where the environmental inflow is laminar and subject to surface drag, starting from an initial wind profile that is constant with height. In such a scenario, owing to the absence of sufficient vertical turbulence mixing, the vertical shear near the ground can be excessively large within a few hours of model integration. In our simulations, because the initial sounding has already been subject to surface drag and is in a three-force balance, the primary issue highlighted in MB16 should not apply; a more detailed discussion is given in Section 4.2.4.

4.2 Simulation results

4.2.1 Overview of mesocyclone evolution in FWFRIC and EnvFRIC

A more complete overview of experiments FWFRIC and EnvFRIC can be found in Section 3.2.1. In this subsection, we will focus specifically on the mesocyclone evolution.

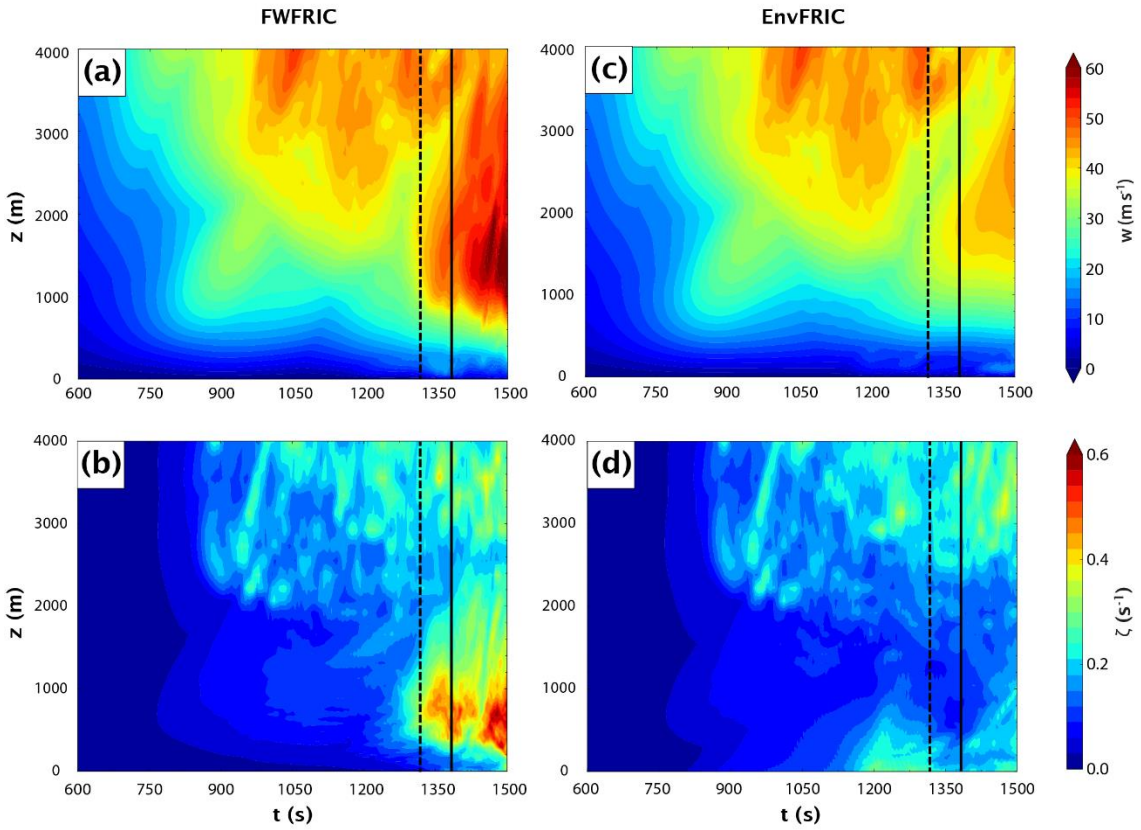

Fig. 4.1. Domainwide time-height cross sections between 600-1500 s for FWFRIC of (a) maximum updraft and (b) maximum vertical vorticity. The dashed and solid black lines denote times t = 1320 s and t = 1380 s, respectively. (c-d) as in (a-b), but for EnvFRIC.

Time-height sections of horizontal domainwide maximum vertical velocity are presented for FWFRIC (Fig. 4.1a) and EnvFRIC (Fig. 4.1c) for the mesocyclone development and intensification period. Beginning around 1200 s, the 20 m s^{-1} maximum updraft contour lowers toward the ground more rapidly in FWFRIC than in EnvFRIC. After 1320 s, maximum updraft below 1 km AGL strengthens rapidly in FWFRIC while remaining nearly steady in EnvFRIC. By 1350 s, the 16 m s^{-1} maximum updraft has descended below 100 m AGL; by 1400 s, updraft exceeding 50 m s^{-1} exists below 1 km AGL (Fig. 4.1a).

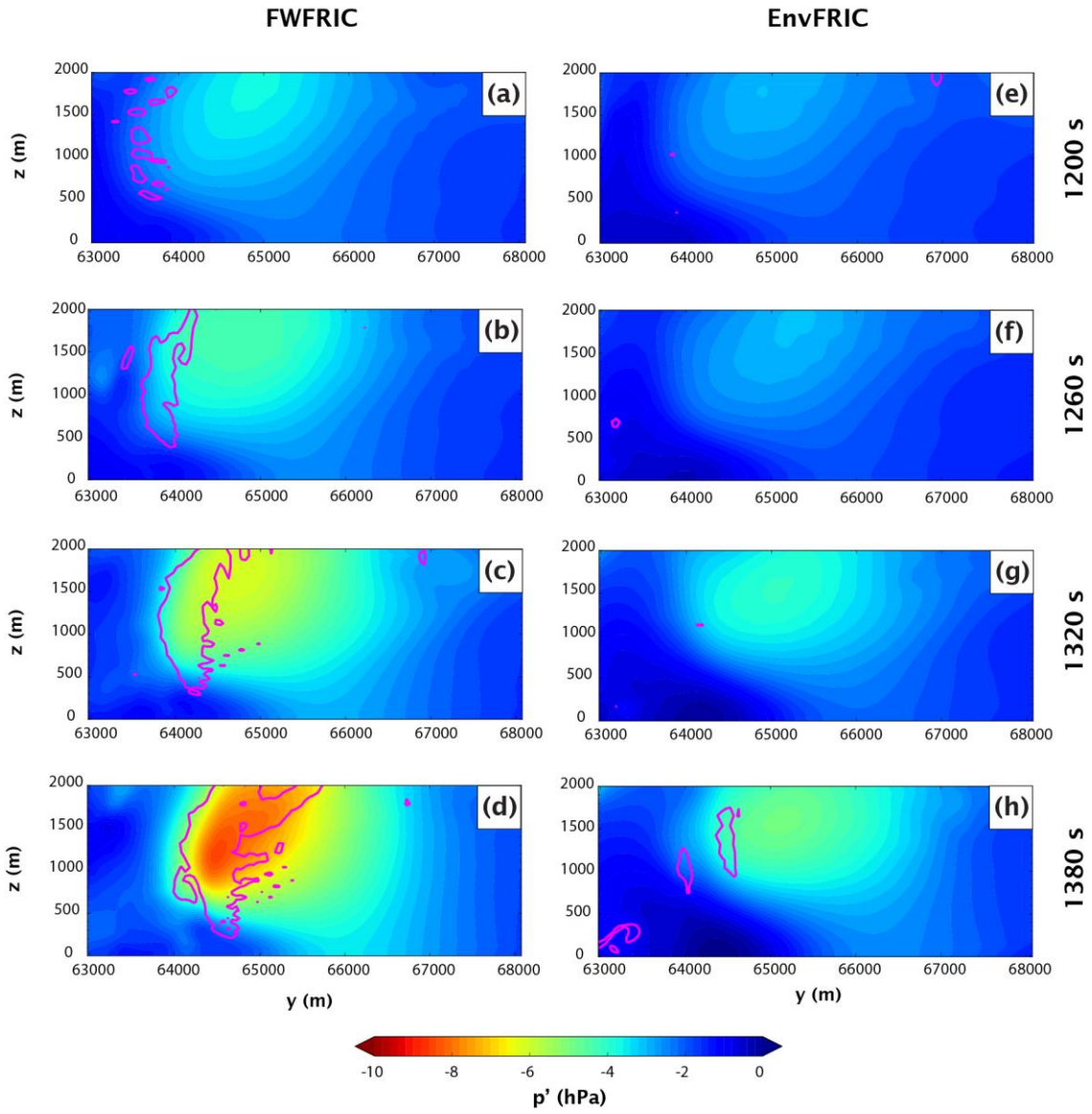

Fig. 4.2. Vertical meridional cross-section through the mesocyclone center in FWFRIC of perturbation pressure (shaded) and the 0.05 s^{-1} vertical vorticity contour (magenta) at (a) 1200 s (x = 35875 m), (b) 1260 s (x = 35875 m), (c) 1320 s (x = 35875 m), and (d) 1380 s (x = 35775 m). The corresponding plots for EnvFRIC are given for (e) 1200 s (x = 35775 m), (f) 1260 s (x = 35625 m), (g) 1320 s (x = 35625 m), and (h) 1380 s (x = 35525 m).

The domainwide maximum vertical vorticity begins to attain larger values in FWFRIC (Fig. 4.1b) than in EnvFRIC (Fig. 4.1d) at around 1280 s below 1 km AGL, with the values in FWFRIC becoming much larger by 1320 s. Overall, the mesocyclone below 1 km AGL in FWFRIC intensifies markedly during the period from 1200-1380 s,

with the most rapid intensification occurring after 1320 s. By 1500 s, vertical vorticity exceeding 0.5 s^{-1} has descended to about 100 m AGL (Fig. 4.1b). By comparison, the low-level mesocyclone in EnvFRIC exhibits much more modest intensification that occurs gradually from 1200-1500 s; by 1500 s, the maximum below 2 km AGL is only about 0.25 s^{-1} (Fig. 4.1d).

Vertical cross-sections of perturbation pressure and vertical vorticity through the center of the low-level mesocyclone[16] are presented in Fig. 4.2 for four times at one minute intervals during the mesocyclone intensification period. For context, horizontal cross-sections of updraft, rainwater mixing ratio, and vertical vorticity are presented in Fig. 4.3 at the first and last of these four times, with heavy dashed lines highlighting the x-z planes of the corresponding vertical sections in Fig. 4.2. At 1200 s, the pressure and vorticity fields are qualitatively similar between the two experiments (Fig. 4.2a and Fig. 4.2e), and this similarity continues through 1260 s (Fig. 4.2b and f), although somewhat larger cyclonic vorticity has begun to develop in FWFRIC. By 1320 s, a vertically coherent region of enhanced cyclonic vorticity is apparent in FWFRIC around y = 64000 m; pressure deficits larger than 4 hPa extend substantially lower toward the ground in FWFRIC than EnvFRIC (Fig. 4.2c and g). Finally, at 1380 s, the negative perturbation pressure at the center of the mesocyclone has become much stronger in FWFRIC than in EnvFRIC (Fig. 4.2d and h). The zone of relatively small pressure deficits near the ground centered around y = 64500 m in both experiments is the storm-scale convergence boundary, directly above which the strongest cyclonic vorticity exists in the mesocyclone. It is noteworthy that the perturbation pressure contours above the

[16] The center point was chosen manually at each plotted time by identifying the mesocyclone's center of circulation at 1000 m AGL.

boundary are oriented more horizontally in FWFRIC (d) than in EnvFRIC (Fig. 4.2h), illustrating that the mesocyclone in FWFRIC is not only stronger overall, but has more effectively lowered toward the ground over a broad extent.

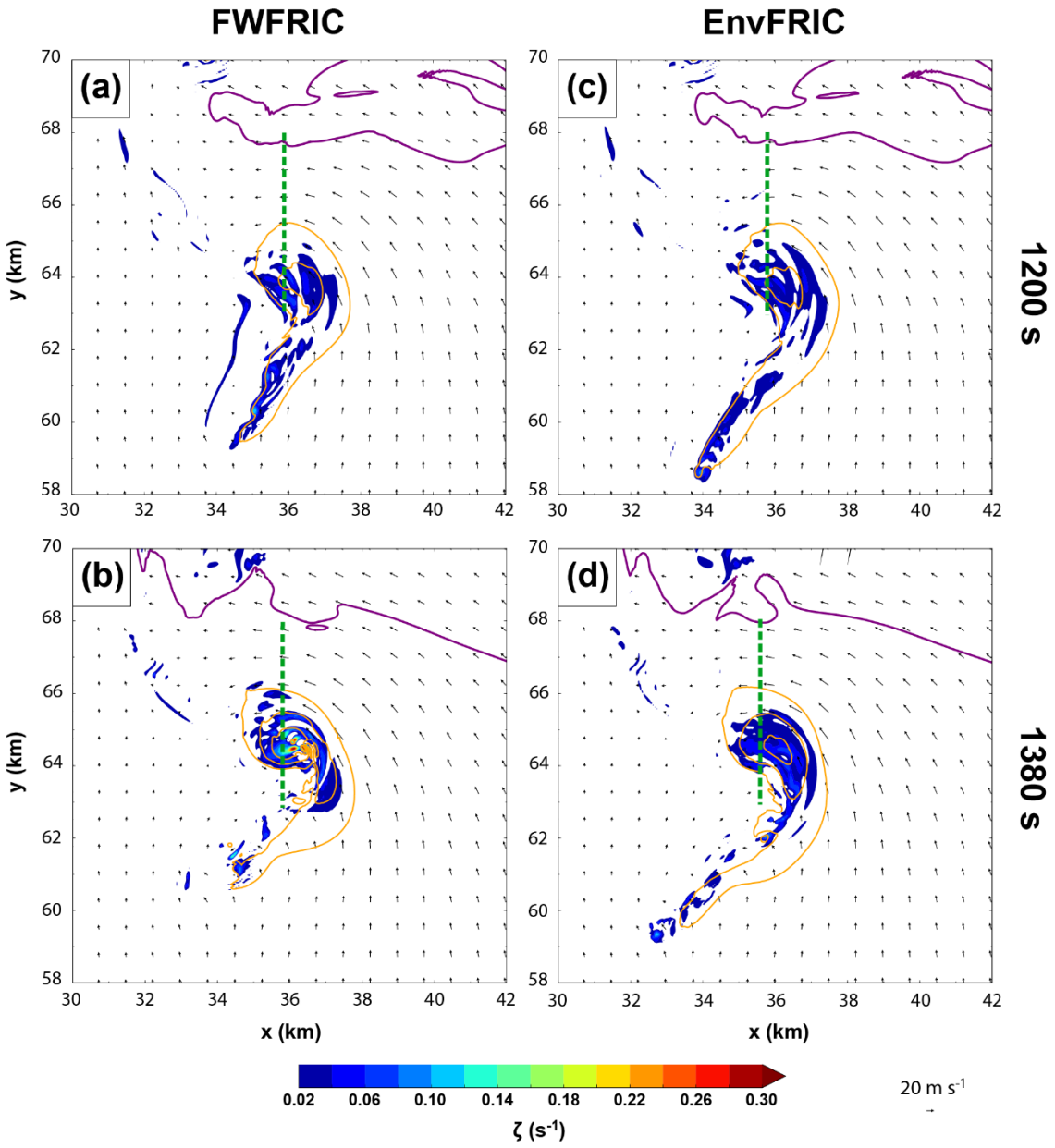

Fig. 4.3. Horizontal cross-section at 1000 m AGL displaying the 0.3 g kg-1 rainwater mixing ratio contour (purple), vertical velocity contours (orange; every 10 m s^{-1} for w ≥ 10 m s^{-1}), vertical vorticity (shaded), and wind vectors; for FWFRIC at (a) 1200 s and (b) 1380 s, and for EnvFRIC at (c) 1200 s and (d) 1380 s. The heavy dashed green line in each panel denotes the plane of the vertical cross-section for the corresponding time in Fig. 4.2 and Fig. 4.4.

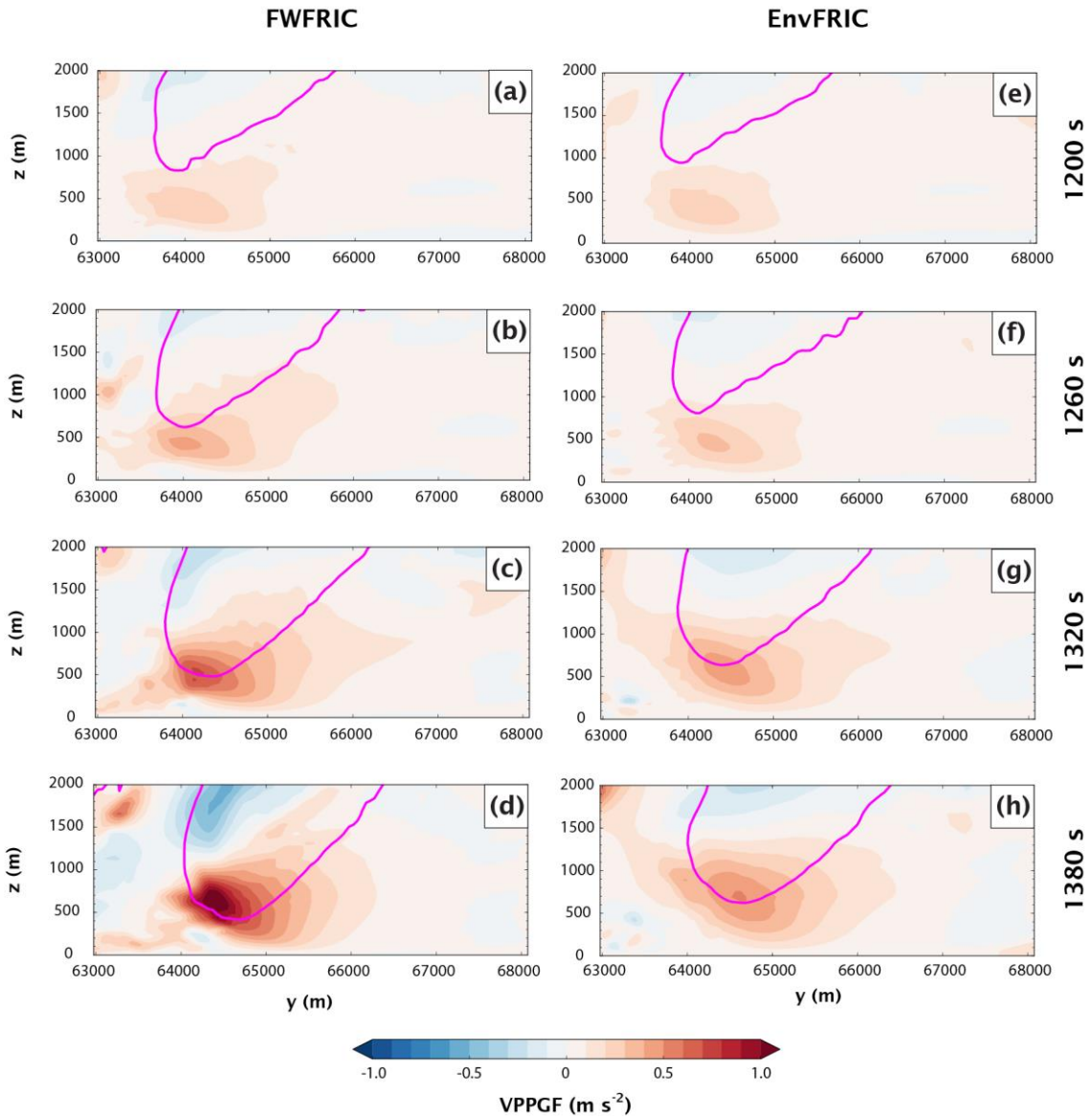

Fig. 4.4. As in Fig. 4.2, but the shaded quantity is the vertical perturbation pressure gradient force, and the magenta contour is the 20 m s^{-1} vertical velocity contour.

Corresponding vertical cross-sections of vertical perturbation pressure gradient force (VPPGF) and vertical velocity are presented in Fig. 4.4. From 1200-1260 s, these fields are quite similar in the two experiments (Fig. 4.4a-b and e-f). At 1320 s, the upward-directed VPPGF around 500 m AGL has become modestly stronger in FWFRIC than in EnvFRIC (Fig. 4.4c and g). By 1380 s, this discrepancy has become much larger, with VPPGF values at 500 m AGL in FWFRIC more than double those in

EnvFRIC (Fig. 4.4d and h). The 20 m s^{-1} updraft contour has also descended to 400 m AGL in FWFRIC, while it remains at around 600 m AGL in EnvFRIC. Based on these vertical sections, it is apparent that the larger VPPGF is dominantly driving the enhanced updraft below 1 km AGL in FWFRIC, particularly as thermal buoyancy is negligible in this region at this stage of the simulation in both experiments (not shown).

Based on the analysis above, the intensification of the low-level mesocyclone in FWFRIC appears to involve a positive feedback cycle. This cycle consists of two processes. Firstly[17], the stronger updraft above the sharper surface convergence boundary in FWFRIC (c.f. Fig. 3.4) enhances vertical stretching of environmental vorticity (after it is tilted) and leads to a stronger mesocyclone. Larger vorticity within the stronger mesocyclone produces larger pressure deficits via the "spin" term of the dynamic pressure equation. Secondly, the reduced pressure around 1 km AGL in FWFRIC increases the VPPGF immediately below, further augmenting the updraft and intensifying the vertical vorticity through stretching. This process also effectively lowers the base of the mesocyclone and further increases the near-ground VPPGF. Thus, a positive feedback exists between the intensification of updraft and vertical vorticity in the low-level mesocyclone. This type of feedback is common in the midlevel mesocyclone as a supercell develops and intensifies, but in this case, the feedback appears also to occur closer to the ground where environmental vorticity is a less effective source of vertical vorticity (Davies-Jones 1984). The vorticity dynamics of the mesocyclone intensification will be analyzed in the following subsection. We will

[17] We do not use "first" or "second" in a chronological sense here, as it is not entirely clear which of the two processes initiates the feedback cycle.

see that the tilting of horizontal vorticity generated by surface friction also plays an important role in the mesocyclone intensification.

4.2.2 Circulation analyses of material circuits enclosing the mesocyclone

To clarify the physical processes contributing to vertical vorticity in the low-level mesocyclone, material circuits are initialized within horizontal planes at various heights; the circuits are constructed such that they closely enclose the mesocyclone at various times. Rotunno and Klemp (1985) first employed material circuits to analyze mesocyclone dynamics within a supercell simulation. In the present study, the material circuits are formed by individual parcels whose trajectories are integrated backward in time using the fourth-order Runge-Kutta method (as in Section 3.2.2) using a 0.5 s integration time step (via temporal interpolation of model output wind fields, which are available every 2 s). When a material circuit is initialized, parcels are placed along the circuit approximately 19 m apart. The initial circuits are circular and contained within a horizontal plane. During backward integration of the trajectories, at each time step, the three-dimensional distance between each pair of adjacent parcels is checked. If this distance exceeds 25 m, a new parcel is initialized at the midpoint of the line segment joining the two parcels. As such, the number of parcels comprising the circuit can increase during integration as needed. This technique of parcel addition for circuit analysis was also employed by Markowski and Richardson (2014); its purpose is to ensure that the circuit is properly sampled along its entire extent, avoiding the development of large gaps between parcels on the circuit.

The circulation about a material circuit is defined as:

$$C = \oint \boldsymbol{v} \cdot d\boldsymbol{l} \qquad (1)$$

where $\boldsymbol{v}$ is the velocity vector and $d\boldsymbol{l}$ is a segment of circuit (directed counterclockwise). Kelvin's Circulation Theorem states that in the barotropic limit and with conservative body forces, circulation is a conserved quantity for a material circuit. In other words, only baroclinity or nonconservative body forces (such as viscous effects) can modify the value of circulation as a circuit evolves over time. In our case, the prognostic equation for circulation can be written as:

$$\frac{dC}{dt} = \oint \boldsymbol{F} \cdot d\boldsymbol{l} + \oint B\, dz \qquad (2)$$

where $\boldsymbol{F}$ is the internal frictional force given by the SGS mixing terms. In our case, the mixing terms include both SGS turbulence mixing and computational diffusion terms; they arise out of physical and computational considerations and they act together to propagate the effect of surface drag into the flow interior. B in (2) is buoyancy. From Stokes' Theorem, circulation about a circuit is equal to the integral of vorticity over a surface bounded by the circuit, which implies that the *average* vorticity normal to the surface bounded by the circuit is proportional to its circulation. In the case of a purely horizontal circuit, then, the average vertical vorticity within the enclosed area is proportional to circulation. With this in mind, initializing horizontal material circuits enclosing the mesocyclone and tracing them backward in time enables us to trace the evolution of the bulk vorticity within the mesocyclone through circulation budgets. This not only provides a holistic assessment of the mesocyclone, but by utilizing many parcels also reduces the opportunity for the type of rapid error growth that budget calculations along individual trajectories are prone to.

For the analysis herein, we construct circular material circuits with a radius of 1.5 km and center them on the wind field's center of circulation (which is identified

subjectively based on plotted wind vectors, and is not necessarily coincident with vorticity maximum) at the height and time of initialization. This radius allows the circuits to enclose the core of the low-level mesocyclone completely, but also tends to keep constituent parcels far enough radially outward from the chaotic wind field near vorticity maxima to avoid rapid error growth in trajectory calculations. We integrate the trajectories for parcels comprising the circuits backward for 10 min (600 s), as integrating further backward in time tends to result in extremely complex circuit shapes with unreliable circulation budgets in some cases. Here we note that when circuit parcels pass below the lowest scalar grid level in the model (10 m AGL), all quantities (besides vertical velocity *w* and its mixing term, which are defined at the ground level) used in the circulation budget calculations are held constant vertically within the 0-10 m AGL layer. Complications related to the treatment of near-ground parcels were discussed at length in Section 3.2.2; in the present study, because we analyze material circuits consisting of many parcels, discarding those which pass below the lowest scalar level is impractical. Instead, we accept the uncertainty associated with the simplistic treatment below 10 m AGL, while expecting that the resulting circulation budgets will still be qualitatively correct if the integrated circulation budgets agree well with model-predicted circulation values.

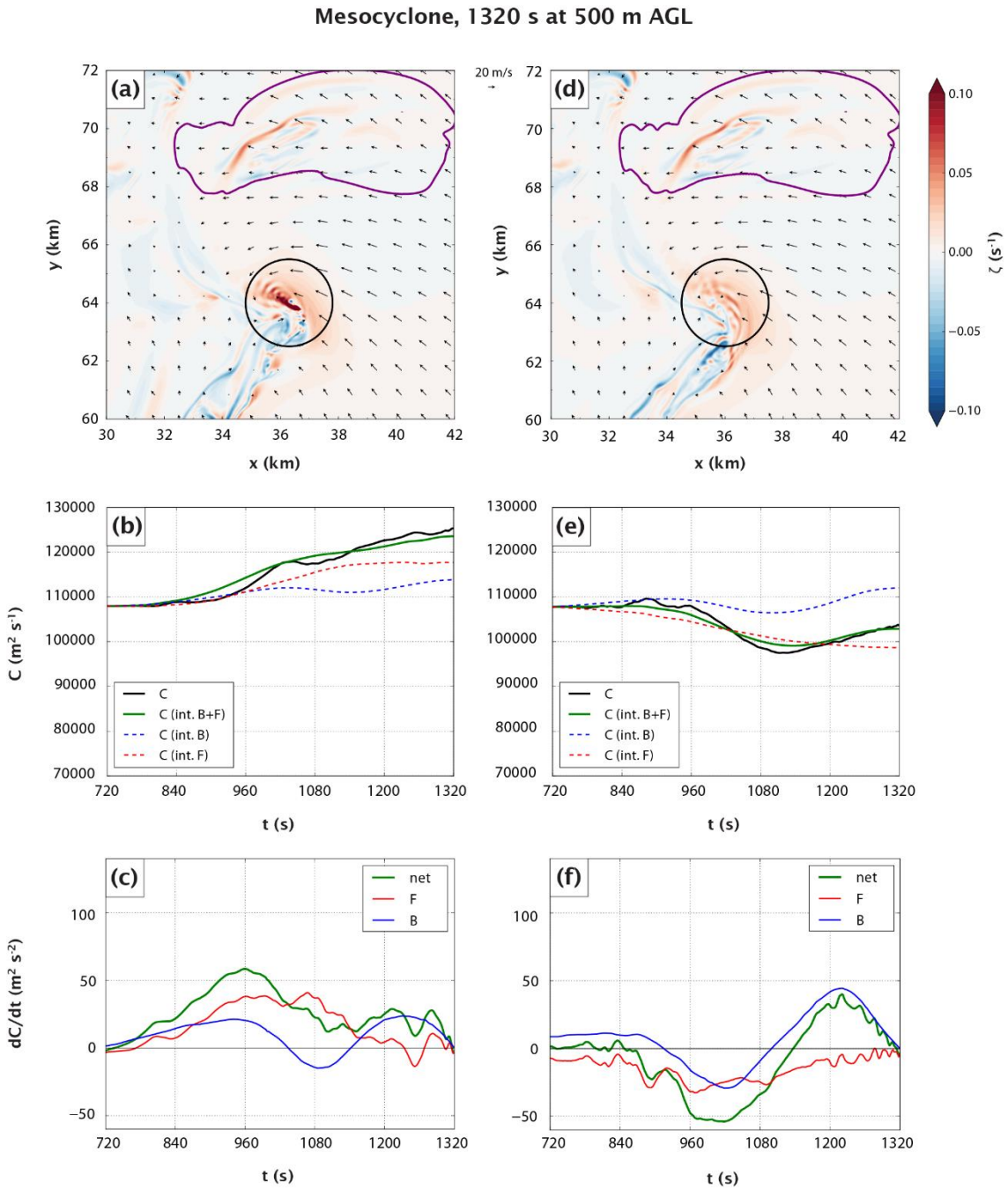

Fig. 4.5. Overview of material circuits initialized enclosing the mesocyclone at 500 m AGL and 1320 s. Horizontal cross-section of vertical vorticity (shaded), the 0.3 g kg^{-1} rainwater mixing ratio contour (purple), wind vectors, and the initial material circuit (black contour) at 1320 s and 500 m AGL in (a) FWFRIC and (d) EnvFRIC. Time series of circulation about the material circuit interpolated from model wind field (solid black), integrated from forcing terms (solid green), integrated from mixing forcing only (dashed red), and integrated from baroclinic forcing only (dashed blue) for (b) FWFRIC and (e) EnvFRIC. Time series of circulation tendency owing to mixing forcing (red), baroclinic forcing (blue), and net forcing (green) for (c) FWFRIC and (f) EnvFRIC.

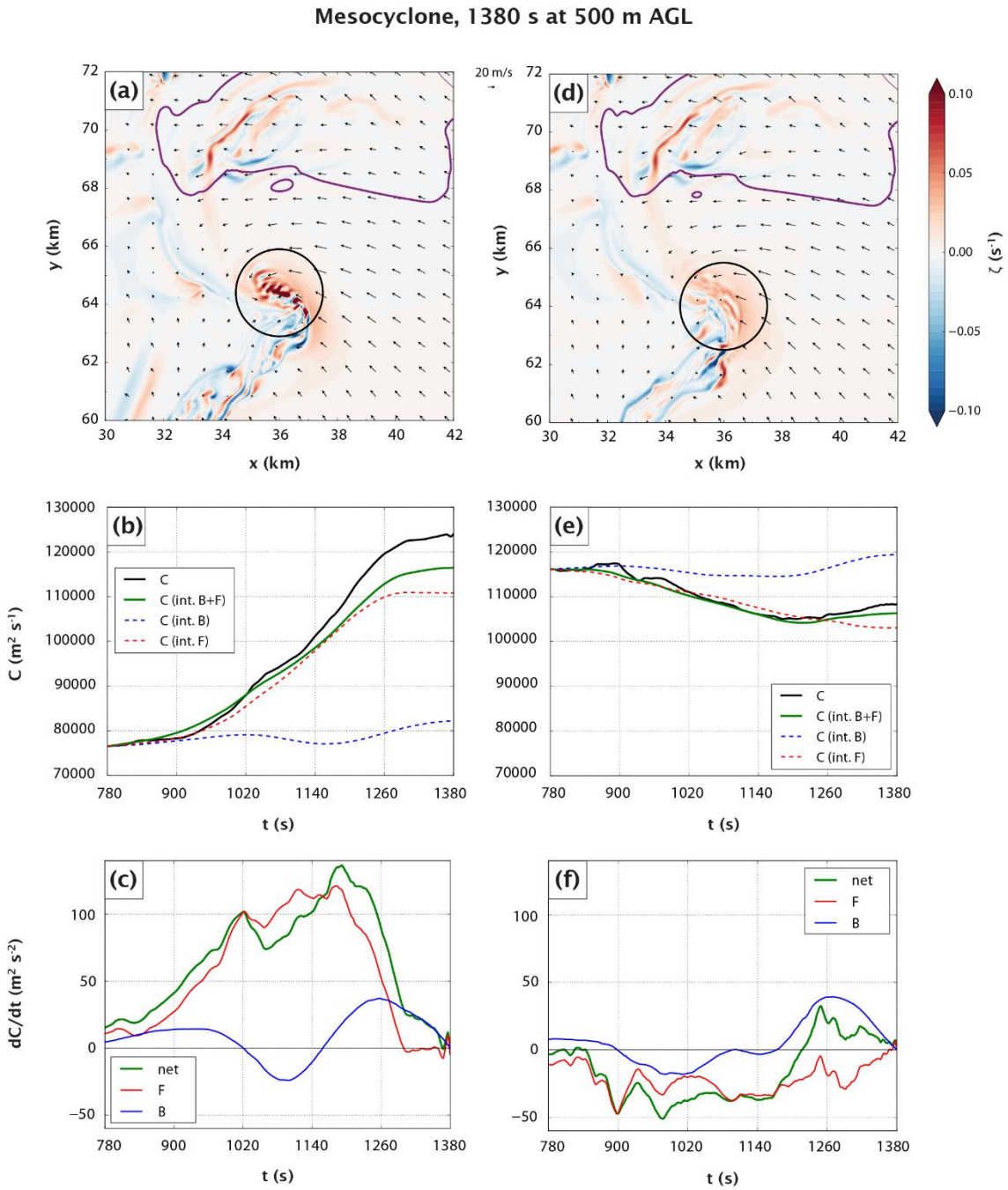

Fig. 4.6. As in Fig. 4.5, but for circuits initialized at 500 m AGL and 1380 s. The integration window begins at 780 s for these circuits.

Fig. 4.5a (Fig. 4.5d) presents an overview of circuits initialized in FWFRIC (EnvFRIC) around the mesocyclone at 500 m AGL at 1320 s. At this time, intensification of the low-level mesocyclone in FWFRIC has just begun. Over the

preceding 10 min, circulation for the circuit in FWFRIC has increased by about 10%, with mixing accounting for most of the increase (Fig. 4.5b). Circulation about the circuit in EnvFRIC has decreased by about 5% over the same period, with mixing again playing a more prominent role than baroclinic forcing (Fig. 4.5e). The mixing forcing term tends to be most positive (negative) in FWFRIC (EnvFRIC) from around 960-1200 s, while the baroclinic term oscillates from positive to negative with a small net impact in both experiments (Fig. 4.5c and Fig. 4.5f). Overall, the change in circulation for these circuits is small in a relative sense, implying that most of the mesocyclone vorticity at 1320 s is barotropic in origin[18].

Fig. 4.6a and Fig. 4.6d present an overview for analogous circuits at 500 m AGL, but initialized at 1380 s. The cyclonic vorticity maxima inside the circuit in FWFRIC (Fig. 4.6a) have intensified relative to those initialized a minute earlier (Fig. 4.5a), indicative of the rapid low-level mesocyclone intensification underway. The time series of circulation for the FWFRIC circuit (Fig. 4.6b) exhibits a dramatic change from that in Fig. 4.5b: circulation nearly doubles during the 10 min preceding the circuit initialization at 1380 s, and a large majority of this increase is due to mixing (Fig. 4.6c). For the circuit in EnvFRIC, the evolution of circulation is quite similar to the circuit initialized a minute earlier, with a small (< 10%) decrease over the period owing primarily to mixing (Fig. 4.6e). A time series of the circulation forcing terms for the circuit in FWFRIC indicates that mixing forcing rapidly increases between 900-1020 s, then remains large and positive until 1260 s (Fig. 4.6c). As such, mixing augments

[18] This is true to the extent that circulation about the circuit at the beginning of the integration period is entirely barotropic; that is, that baroclinic and mixing forcing have not acted on the circuit during the very early part of the simulation. In reality, friction likely has contributed some small portion of this circulation.

circulation rapidly from about 6 min to 2 min prior to the circuit reaching the periphery of the mesocyclone. For EnvFRIC, the mixing term is once again weakly negative during this same period (Fig. 4.6f). In both simulations, baroclinic forcing again oscillates between weakly positive and negative values.

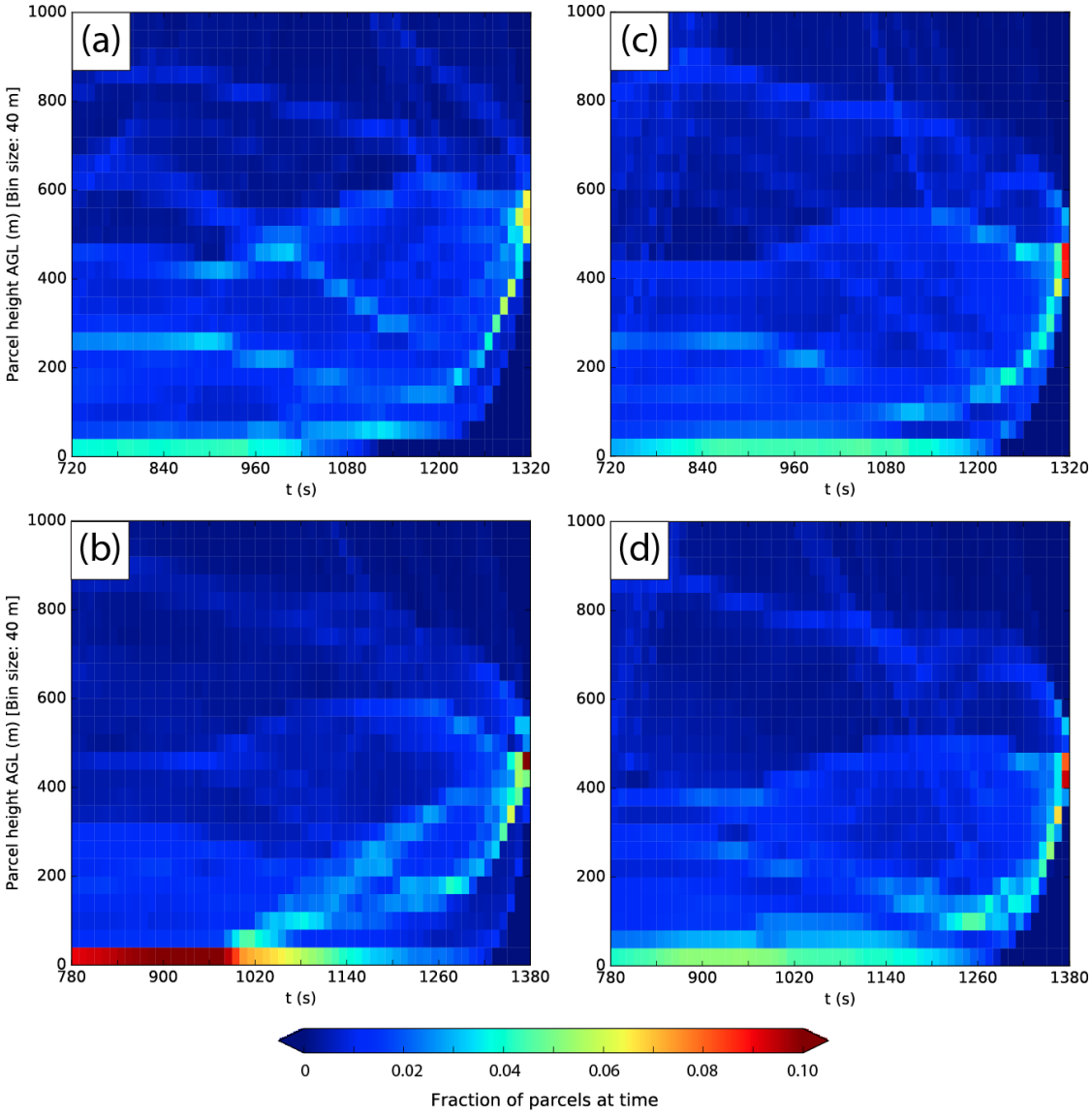

Fig. 4.7. Heat map of parcel height distribution over the integration period for the circuit initialized (a) in FWFRIC at 1320 s, (b) in FWFRIC as 1380 s, (c) in EnvFRIC at 1320 s, and (d) in EnvFRIC at 1380 s. The bins are 10 s along the abscissa and 40 m along the ordinate. In each bin, the shading represents the fraction of all parcels at that time which lie within the height bin (note that the total number of parcels comprising the circuit varies in time, so the shading does not correspond to an absolute number of parcels).

The mixing term's relative contribution to the final value of circulation for the circuit in FWFRIC initialized at 1380 s is much larger (~50%) than in the circuit initialized at 1320 s (~10%). Between 1320-1380 s, the low-level mesocyclone also intensifies and lowers toward the ground. Thus, the introduction of large vorticity generated by surface drag via the mixing term[19] into the mesocyclone seems to be an important component in the intensification and lowering of the mesocyclone. Fig. 4.7 displays time series of circuit parcel height distribution (below 1 km AGL) as heatmaps. The circuit in FWFRIC initialized at 1320 s (Fig. 4.7a) contains a substantially smaller fraction of parcels lying below 40 m AGL throughout the integration period when compared with the circuit initialized at 1380 s (Fig. 4.7b). Physically, this implies that the low-level mesocyclone is drawing a larger proportion of its air from the near-ground layer at 1380 s than it had been a minute earlier at 1320 s; in turn, this allows surface drag to have a larger impact on the circuit at 1380 s. By contrast, when considering the circuits in EnvFRIC, the fraction of parcels in the lowest 40 m AGL remains similar for circuit initialized at 1320 s (Fig. 4.7c) and 1380 s (Fig. 4.7d). This result is more in line with the anemic mesocyclone intensification seen in EnvFRIC during this period.

To clarify the physical mechanisms driving this change in circulation, it is helpful to visualize the spatial evolution of the material circuit and the forcing terms along it. Note that in the following figures, we shade "forcing per unit length" along the circuit to illustrate where forcing terms are the most prominent in a spatial sense. The quantities shaded in these figures are, for mixing (3) and baroclinic (4) forcing:

[19] The mixing term is large near ground because of the strong vertical gradient of the horizontal wind created by surface drag.

$$\frac{\boldsymbol{F}\cdot d\boldsymbol{l}}{|d\boldsymbol{l}|} \quad (3)$$

$$\frac{B\ dz}{|d\boldsymbol{l}|} \quad (4)$$

where $\boldsymbol{F}$ and B are mean values along a line segment connecting two adjacent parcels along the circuit, and $|d\boldsymbol{l}|$ is the length of the line segment.

Fig. 4.8 illustrates the evolution of the material circuit initialized around the mesocyclone at 500 m AGL in FWFRIC at 1320 s. At 960 s (6 min prior to the circuit's initialization), the western portion of the circuit extends upward to nearly 2000 m AGL in height and exhibits a complex structure with many kinks. By contrast, the eastern half of the circuit contains large segments lying within the lowest 200 m AGL that feature only modest curvature, although the easternmost portion loops back upward to about 500 m AGL. At 1140 s, the circuit shape is qualitatively similar, although it has contracted slightly. Finally, at 1320 s, the circuit evolves into the circular shape we initialize it with at 500 m AGL. Circulation forcing from mixing remains relatively small in magnitude throughout the circuit's evolution, except for the vertical segments along its western extent. Here, diffusion within a region of compensating downdraft around the main storm updraft (not shown) tends to produce dipoles in the mixing term which largely offset one another (e.g., the forcing may be positive along portions of an "upward-pointing" segment of the circuit, but there tends to be similar-magnitude negative forcing along the adjacent segment that descends from the circuit's summit). Thus, the net mixing forcing remains relatively small at all times. This pattern of dipoles with offsetting forcings along the higher portions of the circuit on its northwest flank is also seen with the baroclinic forcing term, as well.

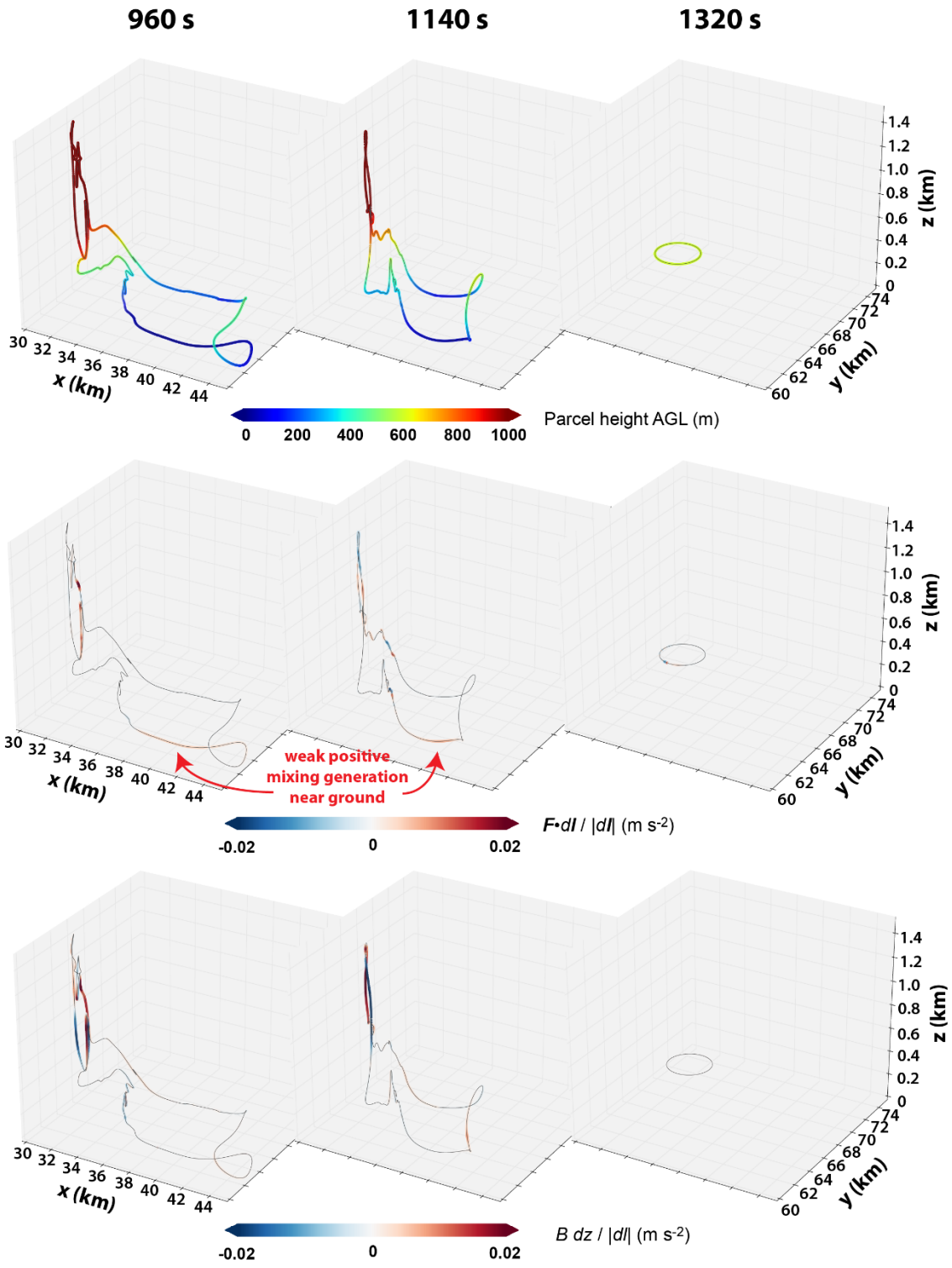

Fig. 4.8. Evolution of material circuit initialized at 1320 s around the low-level mesocyclone at 500 m AGL in FWFRIC. All panels represent the same circuit. In each row, the panels progress forward in time from left to right according to the labels at the top of the figure, concluding with the circular circuit at 1320 s on the right. In the top row, parcels along the circuit are colored by height to help clarify the circuit's 3D

structure. In the middle row, parcels are colored by $\mathbf{F}\cdot d\mathbf{l}/|d\mathbf{l}|$ (the "mixing term") for the adjacent circuit segment, which represents the local contribution to F*dl for that segment. In the bottom row, parcels are colored by B dz/$|d\mathbf{l}|$ (the "baroclinic term"), which represents the local contribution to B dz for the adjacent circuit segment.

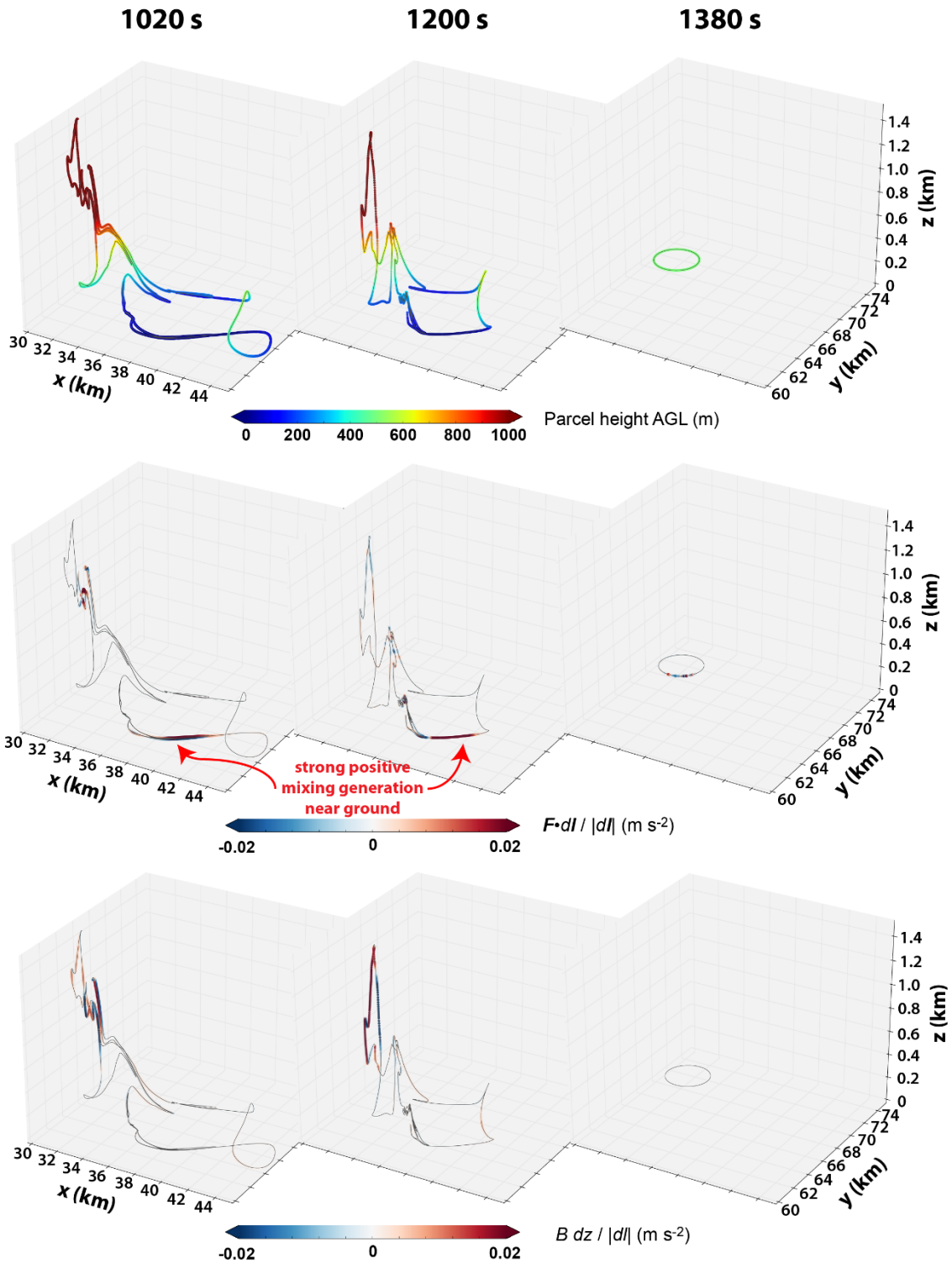

Fig. 4.9. As in Fig. 4.8, except for material circuit initialized around the low-level mesocyclone in FWFRIC at 500 m AGL at 1380 s.

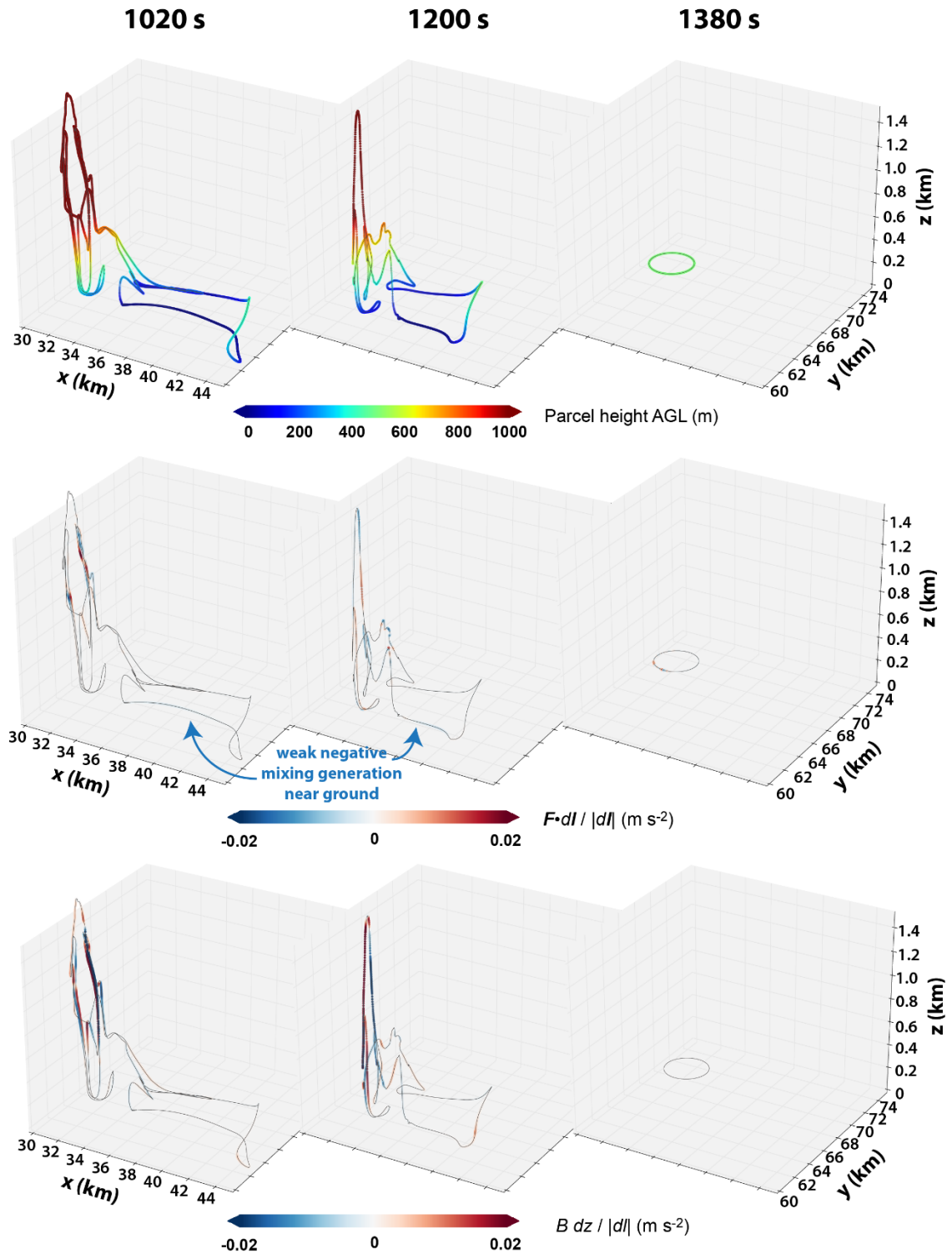

Fig. 4.10. As in Fig. 4.8, except for material circuit initialized around the low-level mesocyclone in EnvFRIC at 500 m AGL at 1380 s.

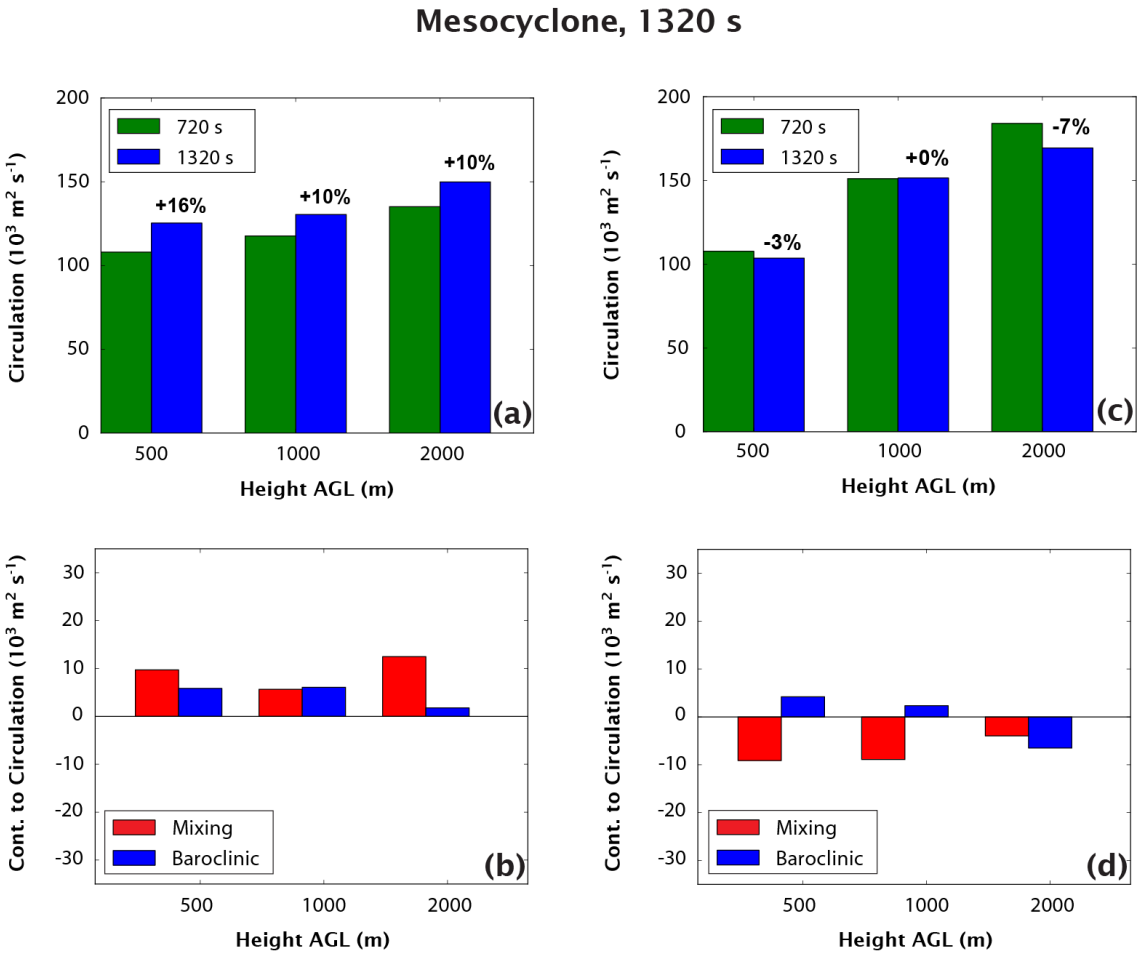

Fig. 4.11. (a) Circulation about the material circuits initialized at 1320 s in FWFRIC; values are presented at the beginning of the budget integration window (720 s, green) and the end of the window (1320 s, blue), and the percentage change over the period is given above the blue bar. These values are plotted for three separate circuits which were initialized surrounding the mesocyclone at 500 m, 1000 m, and 2000 m AGL. (b) Contribution to circulation from the mixing (red) and baroclinic (blue) forcing terms over the 10 min integration window for the same circuits in FWFRIC. (c) Same as (a), but for the equivalent circuits in EnvFRIC. (d) Same as (b), but for the equivalent circuits in EnvFRIC.

Fig. 4.9 illustrates the evolution for the circuit in FWFRIC initialized at 500 m AGL and at 1380 s, when rapid intensification of the low-level mesocyclone is underway. In terms of the shape and spatial distribution of the circuit, the evolution is qualitatively similar to the circuit in Fig. 4.8 which was initialized 1 min earlier, although we note that the total proportion of circuit lying very near the ground is larger

for the circuit initialized at 1380 s (c.f. Fig. 4.7a,b). Examination of the mixing term reveals a crucial difference for this later circuit: at 1020 s and 1200 s, the forcing is large and positive for much of the segment that lies along the ground along the circuit's southern extent. This segment exists within the inflow region east of the low-level mesocyclone, where Section 3.2.2 showed substantial crosswise vorticity generation by surface drag (e.g., Fig. 3.20). As such, it is straightforward to interpret the physical meaning of the large positive mixing forcing on this segment of the circuit. The mixing term, under the influence of surface drag, represents a force directed toward the east. This force opposes the local westward-directed flow (i.e., inflow air accelerating into the mesocyclone to the west). Because the local flow here contributes negatively to circulation (i.e., it is locally consistent with clockwise flow about the circuit), a force retarding the flow actually contributes positively to total circulation about the circuit. This is simply a manifestation of the frictionally-generated vorticity in the inflow region contributing to cyclonic vorticity in the low-level mesocyclone, much as it contributed to the tornado's vorticity for individual parcels analyzed in Chapter 3. For comparison, the evolution of the equivalent circuit (initialized at 500 m AGL, 1380 s) in EnvFRIC is presented in Fig. 4.10. While the spatial distribution of the circuit shares considerable similarity to that in Fig. 4.9, the main segment lying near the ground experiences weak *negative* mixing forcing at 1020 s and 1200 s. This result implies generation of antistreamwise vorticity for parcels in this region, as predicted by M16 for the case of a free-slip lower boundary (see their Fig. 24): in the absence of surface drag (on the perturbation wind) that acts to create large vertical shear, the mixing mainly acts to

reduce the magnitude of vorticity extrema (in the case of EnvFRIC, it reduces the large barotropic streamwise vorticity in the inflow region).

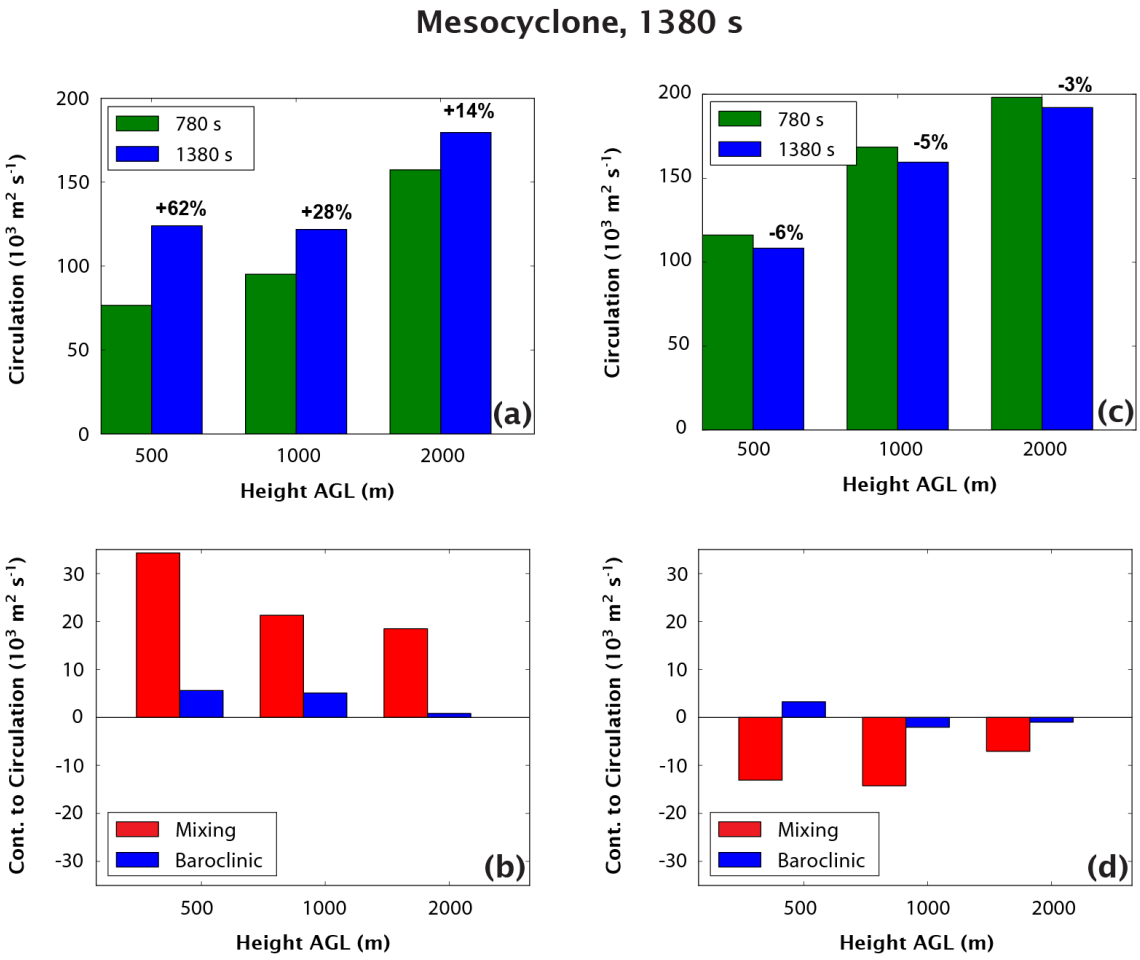

Fig. 4.12. As in Fig. 4.11, but for circuits initialized at 1380 s. The beginning of the budget integration window for these circuits is 780 s.

To evaluate the contribution of frictionally generated vorticity for air parcels at other heights in the mesocyclone, additional circuits were initialized surrounding the mesocyclone at 1000 m and 2000 m AGL in FWFRIC and EnvFRIC at the same times as the aforementioned circuits. Fig. 4.11 presents circulation budgets for circuits initialized at 1320 s. In FWFRIC, the circuits at 500 m, 1000 m, and 2000 m AGL all experience a similar relative increase over the preceding 10 min (Fig. 4.11a), with both mixing and baroclinic forcing representing positive contributions (Fig. 4.11b). In

EnvFRIC, the net changes in circulation over the preceding 10 min are relatively small for all heights (Fig. 4.11c), and the mixing force imposes small negative contributions in all cases (Fig. 4.11d).

Circulation budgets for circuits in FWFRIC initialized at 1380 s evolve much differently: the relative increase in circulation over the preceding 10 min is much larger at 500 m AGL (62%) than at 1000 m AGL (28%) and 2000 m AGL (14%) (Fig. 4.12a). This discrepancy with height owes primarily to the mixing term, whose integrated contribution becomes progressively smaller with height[20] (Fig. 4.12b). Because the *lowering* of the mesocyclone in FWFRIC seems to be a crucial difference relative to EnvFRIC immediately preceding tornadogenesis in the former, these circulation budgets further implicate frictional vorticity: at 500 m AGL, where the mesocyclone is *much* stronger in FWFRIC than EnvFRIC by 1380 s, the frictional contribution is substantially larger than at 1000-2000 m AGL. These results indicate that the contribution of frictionally generated vorticity is large for parcels entering the low-level mesocyclone in FWFRIC. It should be noted that while baroclinic forcing plays a much smaller role, it is still a non-negligible secondary positive contribution to the final circulation at 500 m and 1000 m AGL. For the circuits in EnvFRIC at 1380 s (Fig. 4.12c and d), the budgets at all heights are qualitatively similar to those at 1320 s, mirroring the relatively steady intensity of the mesocyclone over the interim period.

[20] The discrepancy in the mixing contribution over the 10 min integration window does not represent *all* generation that has occurred along the circuit since the beginning of the simulation; it is possible that the circuits initialized at 1000 m and 2000 m AGL experienced *some* mixing generation due to surface drag before the integration time window. However, earlier in the simulation, the storm-induced ground-relative perturbation wind tends to be weak; thus, frictional vorticity generation should be modest.

4.2.3 Circulation analyses of material circuits enclosing the tornado in FWFRIC

The circulation analyses presented above have established the important role of surface drag acting on the storm-induced flow for the intensification of the low-level mesocyclone which precedes tornadogenesis in FWFRIC. In Chapter 3, only trajectory-based vorticity budget analyses were performed. To clarify the results of Chapter 3 and increase their robustness, we apply the same circulation analysis techniques to the incipient tornado in FWFRIC. In this case, horizontal, circular material circuits of radius 1.5 km are initialized at six heights – 100 m, 200 m, 400 m, 600 m, 800 m, and 1000 m AGL – enclosing the incipient tornado at 1500 s. The 1.5 km radius, which was again chosen to keep circuit parcels away from strong wind gradients that greatly reduce the accuracy of trajectory calculations, encloses portions of the low-level mesocyclone immediately surrounding the tornado vortex; therefore, changes in circulation for these circuits may not always directly correspond to the evolution of vertical vorticity within the tornado itself. However, most of the circulation change over the budget period should be related to the rapidly-strengthening tornado vortex centered within the mesocyclone; this is particularly true because of the strongly convergent wind field, which tends to contract the circuits quickly toward the vortex center when integrated forward in time (not shown).

Fig. 4.13a compares the total circulation of these circuits 10 min prior to initialization (900 s) with the values at initialization (1500 s); this is the same integration window used for trajectories in Chapter 3 which were initialized within the tornado at 1500 s. A clear, stable trend is evident wherein the relative increase in circulation over the 10 min preceding tornadogenesis is larger at lower heights.

Circulation more than doubles over this period for the circuit initialized at 100 m AGL, while it increases by only 26% initialized at 1000 m AGL.

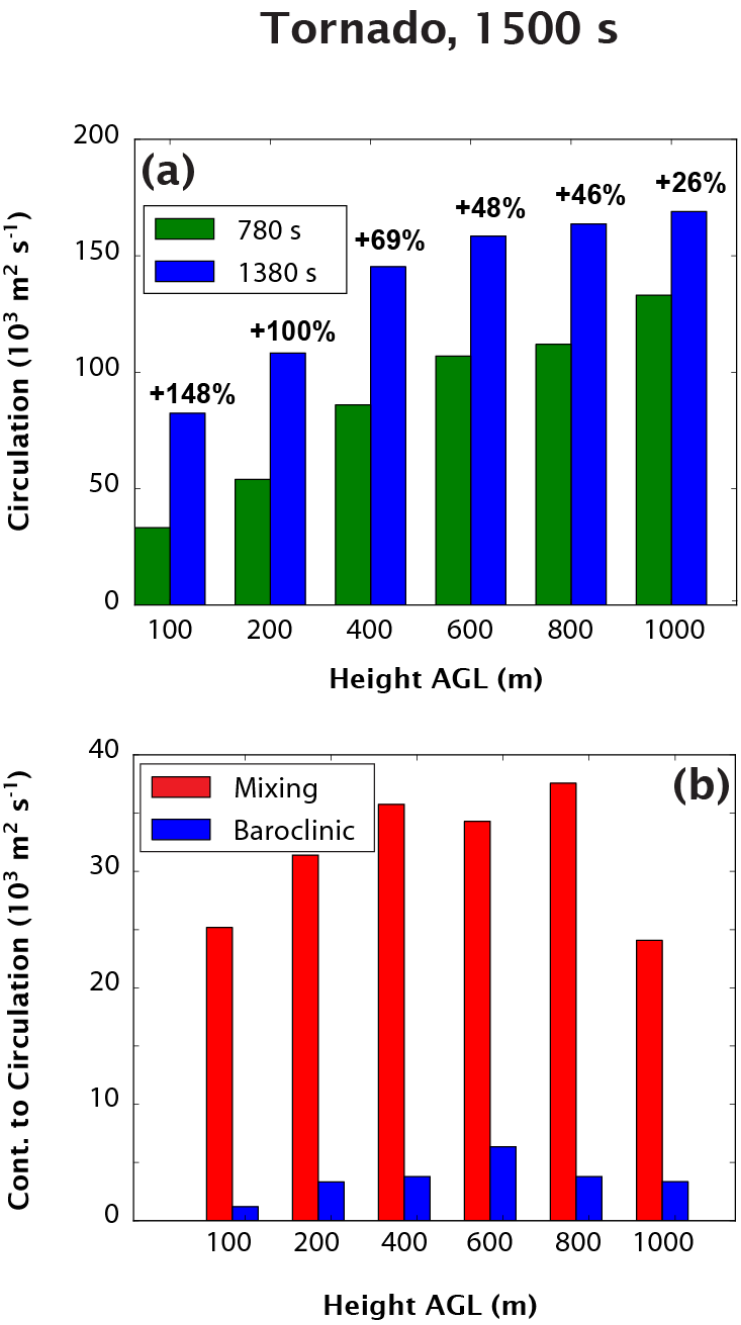

Fig. 4.13. (a) Circulation about material circuits initialized at six heights enclosing the incipient tornado in FWFRIC at 1500 s; values are presented at the beginning (900 s, green) and end (1500 s, blue) of the budget integration window, and the relative change over the period is given above each blue bar. (b) Contribution to circulation from the mixing (red) and baroclinic (blue) forcing terms over the 10 min integration window for the same circuits.

Fig. 4.13b presents the integrated contributions to circulation over the preceding 10 min by the mixing and baroclinic forcing terms for the same circuits in Fig. 4.13a. The contribution from mixing is approximately an order of magnitude larger than baroclinity for all circuit initialization heights in the tornado. As such, the increases in circulation between 900-1500 s seen in Fig. 4.13a are primarily from surface drag.

The dominance of frictional forcing in the circulation budgets for the tornado-enclosing circuits bolsters confidence in the narrative presented in Chapter 3 (c.f. Fig. 3.12, Fig. 3.14), particularly regarding what we termed therein as Mechanism II (the import of frictionally generated vorticity into the incipient tornado). A chief concern regarding the trajectory analysis in Chapter 3 was the limitation imposed by poor vorticity budget accuracy when parcels descended below the lowest scalar level (10 m AGL). This limitation forced us to exclude these parcels from our analysis, in effect placing a lower bound of about 400 m AGL on the height at which we could initialize trajectories in the tornado (trajectories initialized any lower tended to originate almost exclusively from below 10 m AGL). Thus, while we demonstrated conclusively that frictional vorticity was an important source of tornadic vorticity at 400 m AGL, a degree of speculative extrapolation was necessary in Chapter 3 to invoke this same mechanism near the ground. With the circulation analyses performed in the present study, frictional vorticity is clearly shown to play a crucial role in the tornado below 400 m AGL; in fact, its role is increasingly larger with decreasing height down to at least 100 m AGL. We are therefore much more confident that in FWFRIC, vorticity near the ground in the incipient tornado at 1500 s is overwhelmingly frictional in origin. The circulation analyses also show that the contribution of frictionally generated

vorticity within the incipient tornado is greater than for the preceding low-level mesocyclone; this appears to be a consequence of most air parcels entering the tornado originating from very near the ground, allowing surface drag to modify their vorticity over an extended duration.

Circuits are also initialized enclosing the strengthening tornado at 1560 s, but the circulation budgets are much less reliable and some circuits became excessively distorted only 5-7 min into the backward integration (not shown). In general, the source terms for circulation tendency along these circuits initialized at 1560 s suggest a somewhat greater role for baroclinic generation than for the circuits initialized at 1500 s, although frictional generation remains the largest contributor. This is in line with the theoretical arguments of Dahl (2015) as well as the simulation results of MS16b, which suggest the relative importance of baroclinic vorticity becomes greater as a tornado matures.

4.2.4 Near-ground vertical wind shear in the inflow region

MB16 raised concerns pertaining to the potential overestimation of near-ground wind shear in laminar flows for LES simulations, which was shown to be quite severe for their idealized case initialized with a background wind profile that was constant with height. We wish briefly to address the potential applicability of this issue to our simulations herein. It is important to emphasize that the original sounding (MAY3) extracted from a real data simulation had already been subject to parameterized PBL mixing, and is further spun up through 48 hours of a 1D column simulation that includes surface friction to reach a steady state three-force balance. Therefore, our environmental profile should not suffer from the problem highlighted in MB16, which

depicted a “worst-case scenario” where the model was forced to develop a PBL wind profile from an (unrealistic) initial profile with zero vertical shear. Thus, in our experiments, we do not expect the type of extreme near-ground shear overestimation seen in MB16.

In our experiment FWFRIC, the storm-induced flow is subject to surface drag. This means when the low-level inflow accelerates towards the storm, near-surface shear should increase. It is worthwhile to evaluate the magnitude of this increase to ensure it is physically reasonable. As a reference point, we look to Nowotarski and Markowski (2016) (hereafter NM16), who examined supercell simulations at 200-m horizontal grid spacing; unlike our simulations, they perturbed the initial PBL flow to induce the development of boundary layer eddies and rolls in the storm environment. Their simulations also included surface heating due to radiation. As such, their simulations should not be subject to the concerns raised in MB16. They found that the 0-1 km SRH calculated from a mean profile in their near-storm inflow environment exceeded that in the far field by as much as 76%, for experiments with convective rolls primarily perpendicular to the storm motion (see their Fig. 3 and Table 1). In Fig. 4.15a, we present a comparison of the MAY3B hodograph used to initialize our experiments against an average “near-storm” inflow profile in FWFRIC at 1080 s (during the time period in which we show important effects from surface drag in our circulation budgets). Fig. 4.15b shows the spatial context of this average profile within a horizontal cross-section at 10 m AGL, including the position of the circuit from Fig. 4.6 at that time. The 0-1 km SRH in our averaged inflow profile is approximately 79% larger than in MAY3B. The enhancement to the 0-1 km SRH by surface drag in our near-storm

environment (79%) is almost identical in magnitude to the perpendicular-roll CBL simulations of NM16 (78%), even though we do not explicitly introduce thermal perturbations to promote convective eddies and rolls within the boundary layer. In fact, even if we were to introduce such perturbations, we would not expect development of significant resolvable eddies in our simulations because no surface radiative heating is included (as in NM16's CBL experiments). The SGS turbulence mixing in our simulations is playing the role of shear-induced eddy mixing and keeping the resolved flow more or less laminar outside the storm.

4.3 Summary and discussion

In this study, the low-level mesocyclone evolution was examined in two supercell simulations differentiated solely by how the surface drag is applied. In the simulation with drag applied to the full wind (FWFRIC), the mesocyclone rapidly intensified and lowered below 1 km AGL between 1200-1500 s, leading to tornadogenesis; in the simulation with drag applied only to the base-state wind (EnvFRIC), the mesocyclone only intensified and lowered modestly during this period, and tornadogenesis did not occur.

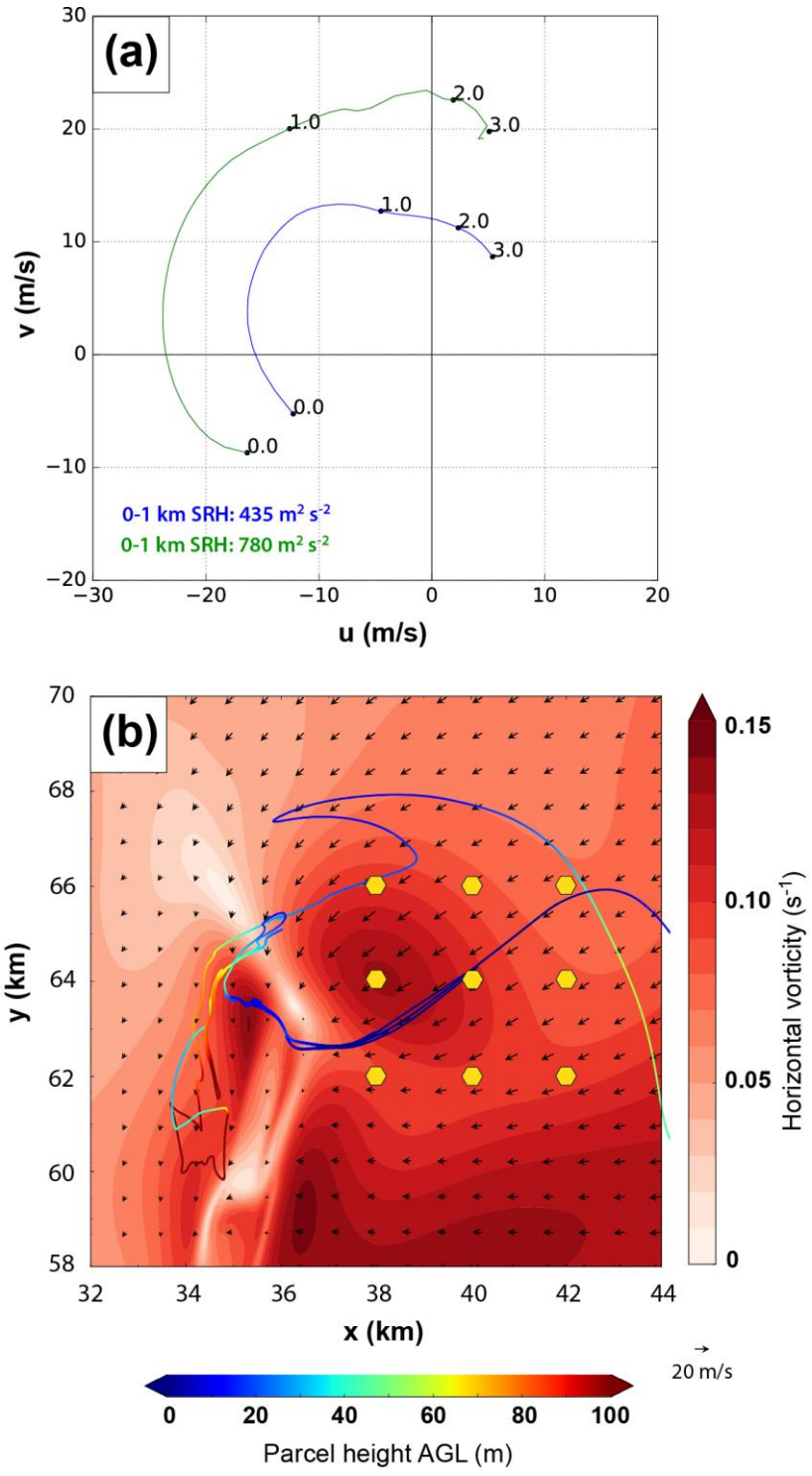

Fig. 4.14. (a) Comparison of hodographs for the initial sounding MAY3B (blue), and an average of nine points in the inflow region in FWFRIC at 1080 s (green). (b) Horizontal cross-section at 10 m AGL in FWFRIC at 1080 s of horizontal vorticity (shaded) and wind vectors. The nine yellow hexagons denote points from which the averaged "near-storm" hodograph in (a) is derived. The position at 1080 s for the circuit from Fig. 4.6 is overlaid for context, colored by the local parcel height AGL.

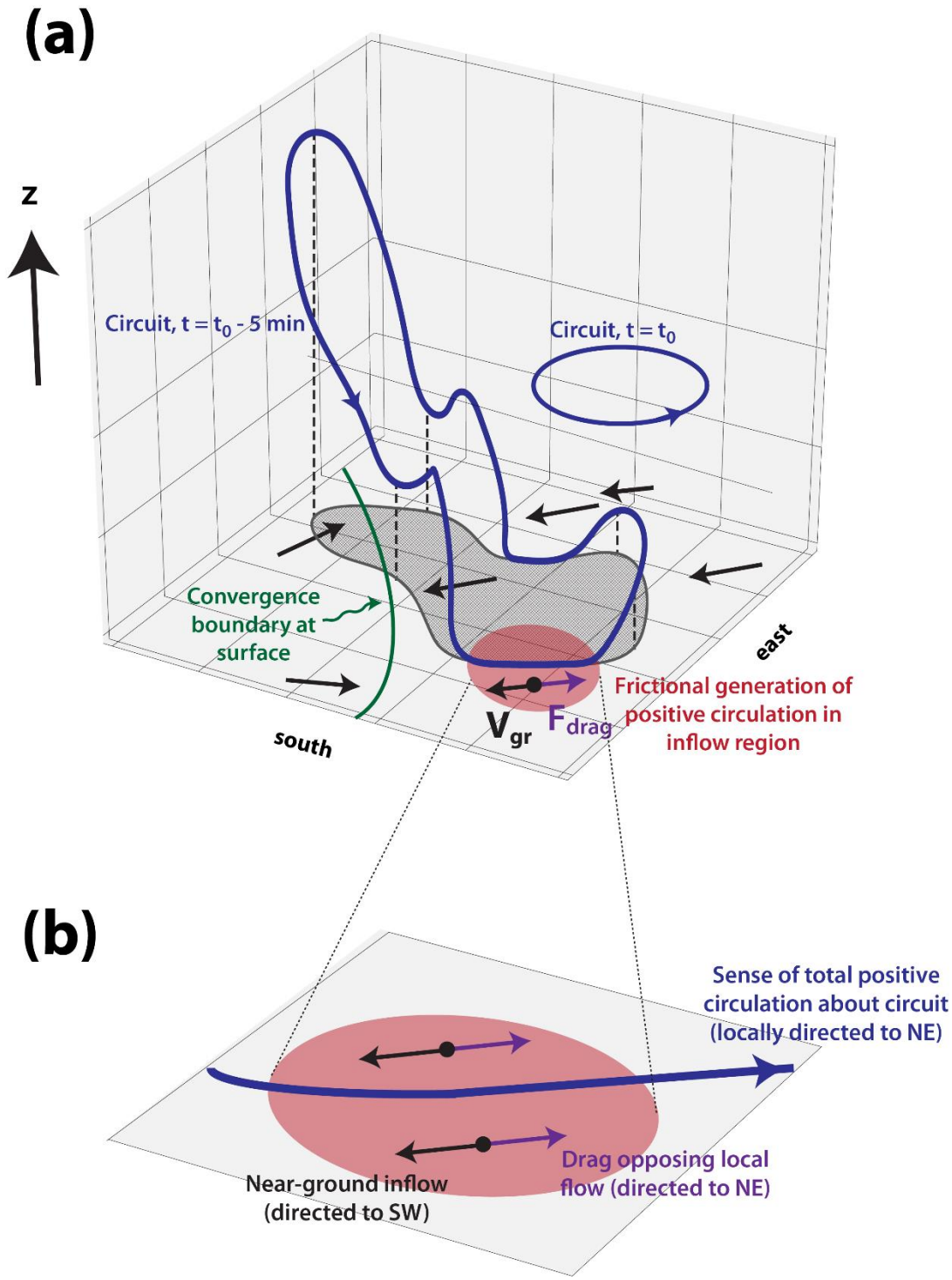

Fig. 4.15. (a) Conceptual model for evolution of a circuit which encloses the low-level mesocyclone in FWFRIC during rapid intensification. The partial cube in the background (light gray with gridlines) is viewed from above and the southeast, with walls drawn on its bottom, western, and northern faces. The circuit is denoted by a blue curve with snapshots shown at two different times: $t = t_0$, and $t = t_0 - 5$ min. The blue arrows along the circuit indicate the sense of total circulation. The gray shaded region

enclosed in a heavy line is the horizontal projection of the circuit at t = t_0 - 5 min onto the ground. The southeastern portion of the circuit at this time descends below 100 m AGL, where a northeastward-directed frictional force generates large positive circulation tendency; the area containing the circuit segment where this occurs is shaded in red. The horizontal ground-relative wind at 10 m AGL is given by black vectors, while the frictional force at 10 m AGL is given by the purple vector. The green curve denotes the position of the convergence boundary at 10 m AGL, which is located south and west of the main frictional generation zone. (b) Zoomed view of the red circle in (a), which lies in a horizontal plane at approximately 10 m AGL. Vectors and blue curve are the same as in (a), but annotated to clarify the physical processes and emphasize that the drag force and circuit circulation are both directed toward the northeast in this area.

Rapid intensification of the low-level mesocyclone in FWFRIC appears to have its origins in the stronger horizontal convergence along the storm-scale convergence boundary at the surface (relative to EnvFRIC), which promotes a modestly stronger low-level updraft from 1200-1320 s, and hence stronger stretching of environmental vorticity after it is tilted into the vertical. Once vorticity within the low-level mesocyclone begins to ramp up during this period, the corresponding dynamic pressure drop yields an enhanced upward-directed VPPGF below 1 km AGL and initiates a positive feedback cycle of intensification and lowering of the mesocyclone. The presence of large frictionally-generated vorticity in the inflow region east of the convergence boundary in FWFRIC is a key factor which sustains this cycle for several minutes, culminating in tornadogenesis by 1500 s. In EnvFRIC, relatively weaker convergence at the surface (and associated low-level updraft) hampers the establishment of this feedback cycle. Furthermore, even to the limited extent that the feedback does occur in EnvFRIC, the lack of frictionally-enhanced horizontal vorticity for parcels near the ground further inhibits its progression relative to FWFRIC.

Leslie (1971) proposed a mechanism by which a vortex may build downward with time through a bootstrap process known as the dynamic pipe effect (DPE), and this

idea has influenced the subsequent literature on tornadogenesis. The positive feedback observed during the low-level mesocyclone intensification and lowering in FWFRIC shares some similarities with the DPE. Trapp and Davies-Jones (1997) used analytical and numerical models to illustrate a theoretical basis for the role of the DPE in real-world tornadogenesis. Davies-Jones et al. (2001), however, argued against the DPE as a mechanism capable of generating a vortex at the ground from purely barotropic vorticity; in other words, the midlevel mesocyclone formed from tilting environmental vorticity probably cannot build all the way to the ground simply through the bootstrap process. French et al. (2013) also showed using mobile doppler radar observations that tornado vortex signatures (TVSs) for three separate supercell tornadogenesis cases actually appeared first near the ground, then built upward, counter to the DPE. Nonetheless, the DPE can potentially explain the lowering of a mesocyclone below 1 km AGL, particularly in cases where horizontal streamwise vorticity is very large at the time it is tilted into the vertical. Wicker and Wilhelmson (1995) and Noda and Niino (2010) noted dynamically-induced lowering of the low-level mesocyclone similar to that in FWFRIC herein; in their simulations, baroclinic vorticity provided the surplus of horizontal vorticity near the ground necessary for rapid vortex stretching below 1 km AGL.

The circulation analyses we presented for FWFRIC during mesocyclone intensification show that frictional circulation is generated rapidly on segments of the circuit lying near the ground in the inflow region. A conceptualized illustration of this circuit evolution is presented in Fig. 4.15a, with an annotated zoom of the drag-induced circulation generation region in Fig. 4.15b. Note that the convergence boundary is

simply a near-ground wind shift line bisecting the low-level mesocyclone, separating generally westward-directed (to the northeast of the boundary) vs. eastward-directed (to the southwest of the boundary) flows (c.f. Fig. 4.6a). When parcels are drawn upward into the low-level mesocyclone from the inflow region east of the boundary (e.g., the red zone along the ground in Fig. 4.15a and b) and their horizontal vorticity is tilted into the vertical, the large frictionally-generated vorticity component gives them a "head start" in cyclonic vorticity amplification, relative to near-ground parcels drawn into the mesocyclone in EnvFRIC. The initial horizontal vorticity of the near-ground parcels in EnvFRIC is approximately limited to that of the background environment, as drag has not acted to enhance vorticity within the inflow region in that experiment. Bluestein (2007) argues that low-precipitation supercells, owing to their lack of strong cold pools, should not be expected to produce strong low-level mesocyclones "unless there is strong, pre-existing horizontal vorticity in the boundary layer." During the early stages of our simulated storm in the present study, the storm shares thermodynamic characteristics with a low-precipitation supercell, so similar logic applies. While the background shear in the sounding used for both of our experiments features considerable vorticity in the boundary layer (e.g., 0-1 km SRH of 435 m^2 s^{-2}), the substantial enhancement of vorticity by drag within the lowest few hundred meters AGL in FWFRIC appears to tip the scale in favor of rapid mesocyclogenesis down to 400 m AGL.

Although our results are robust in terms of the signal in the circulation budgets, as well as the agreement between the interpolated (from model predicted fields) and integrated values of circulation in the budgets, there are a couple of caveats that bear

reiterating. First, our treatment of circuit parcels passing below 10 m AGL introduces a certain degree of uncertainty (there are no grid levels below 10 m AGL to resolve the near-wall gradient of flow). Second, LES turbulence schemes tend to overestimate near-wall shear of wall-parallel flows, which may quantitatively affect the amount of vorticity generation by the surface drag. We again note that this problem is different from the shear overestimation problem specific to laminar flow in LES discussed in MB16; in our case, the inflow profile comes from a background sounding already subject to the effects of surface drag, and is in a three-force balance.

Our analysis of circuits enclosing the incipient tornado at 1500 s in FWFRIC corroborates the critical role of frictionally-generated vorticity that we proposed in Chapter 3. Furthermore, the circulation budgets for these circuits quantitatively demonstrate an unsurprising but important fact: within the lowest 1 km AGL of the tornado, frictional forcing accounts for a decreasing proportion of the total circulation with height. At 100 m AGL, more than half of the total circulation surrounding the tornado at 1500 s comes directly from friction. This suggests that despite the large barotropic vorticity in this layer from the background wind shear, new vorticity generated by friction within accelerating inflow during the 5-8 min prior to tornadogenesis can be the most important source of tornadic vorticity near the ground. In future work, we plan to investigate this phenomenon by applying circulation budget analysis to a wider array of simulations, including those with heterogeneous initial conditions and tornadoes which occur in the presence of an established cold pool. We also plan to perform additional idealized simulations with different sounding profiles

and different drag coefficients, which should help to clarify how generalizable the conclusions of the last two chapters are for tornadic storms.

Chapter 5 The Effect of the Drag Coefficient on Mesocyclone and Tornado Evolution

5.1 Methodology

In this chapter, a set of five experiments is performed using the ARPS where each experiment is differentiated solely by the value of the drag coefficient. Except where noted in this section, the model configuration is the same as described in Section 3.1.1. Once again, the grid spacing is 50-m in the horizontal, and the vertical grid is stretched from 20 m at the ground to 400 m above 10 km AGL. The initial condition is horizontally homogeneous and derived from sounding MAY3B, and an artificial thermal bubble of maximum amplitude 6 K is placed near the domain center to initiate deep moist convection.

5.1.1 Large-scale balance technique

In comparison to FWFRIC and EnvFRIC, the primary difference in the model configuration for the experiments in this chapter is that a new technique is employed to achieve a three-force balance in the model among the horizontal PGF, Coriolis, and frictional forces. This "large-scale balance" (LSB) technique was developed by Dr. Daniel Dawson with the goal of allowing the background environment to remain quasi-steady in idealized simulations that are initialized with an arbitrary sounding, even if surface drag is active in the model. Assume that a sounding (hereafter "observed sounding" for the remainder of Section 5.1) with which we wish to initialize a simulation was sampled in an environment that was already subject to a three-force balance:

$$0 = -\frac{1}{\rho_z}\frac{\partial p_z}{\partial x} + fv + F_x[u], \tag{5.1}$$

$$0 = -\frac{1}{\rho_z}\frac{\partial p_z}{\partial y} - fu + F_y[v], \tag{5.2}$$

where F represents the frictional terms calculated from quantities inside the square brackets. If we conduct a simulation in the ARPS using this observed sounding as the initial condition, we can directly simulate the Coriolis force (second RHS term) and (parameterized) surface drag (third RHS term) in the model because they are strict functions of the local wind profile, which is known. It is only the horizontal PGF (first RHS term) from the observed sounding environment that is not known, in the general case. If we assume that the Coriolis and frictional forces acting in our simulation are representative of the corresponding forces in the observed sounding environment, it is straightforward to estimate the horizontal PGF from (5.1) and (5.2):

$$P_x = fv + F_x[u], \tag{5.3}$$

$$P_y = -fu + F_y[v], \tag{5.4}$$

where P is a pseudo-PGF force that represents our estimate of the real horizontal PGF in the observed sounding environment. In practice, we obtain the RHS of (5.3) and (5.4) using the change in the horizontal wind components after the first time step of model integration[21]. At this early time, away from the thermal bubble, the Coriolis and frictional forces are the only forces acting on the wind profile. As such, we estimate:

$$fv + F_x[u] = \frac{u_1 - u_0}{\Delta t}, \tag{5.5}$$

$$-fu + F_y[v] = \frac{v_1 - v_0}{\Delta t}, \tag{5.6}$$

[21] In the experiments herein, we evaluate (5.5) and (5.6) at the southwesternmost interior grid column in the domain; in general, they could be evaluated at any unperturbed grid column.

where the subscripts for u and v indicate the model time step, and Δt is the duration of a model time step. After the first model time step, (5.5) and (5.6) are solved at each vertical grid level, which defines the vertical pseudo-PGF profile. We then add the pseudo-PGF to the momentum equations for all subsequent time steps in the simulation. With the pseudo-PGF active in the model, the wind profile remains quasi-steady in time away from introduced perturbations (e.g., from a convective storm).

For the purposes of idealized storm-scale simulations with parameterized drag, the LSB technique can be used in lieu of the comparatively complex friction balancing procedure (FBP) described in Section 3.1. In addition to its relative simplicity, an advantage of the LSB technique is that it yields a force-balanced profile that does not differ meaningfully from the observed sounding. This is advantageous in that it allows for the use of an arbitrary user-specified drag coefficient in the model while maintaining the background wind profile, which may be desirable for comparisons between simulations. It is important to note that while the LSB technique yields a force-balanced background environment in the model, it does not represent the *same* force balance which would have occurred in the observed sounding environment for an arbitrary drag coefficient. If the drag coefficient in a simulation employing the LSB technique is smaller (larger) than the drag coefficient in the observed environment, the pseudo-PGF at grid levels near the ground will underestimate (overestimate) the magnitude of the real PGF from the observed sounding environment; its orientation will also contain error. Consequently, the balanced wind profile in the simulation will likely exhibit more (less) near-ground shear than would the observed sounding environment in the presence of the smaller (larger) user-assigned drag coefficient. Fig. 5.1 illustrates how the LSB

behaves in a limiting case where the drag coefficient is large in the observed sounding environment, but is set to zero in the simulation. In such a case, the simulation's background wind profile near the ground (Fig. 5.1b) would differ markedly from the real geostrophic profile (Fig. 5.1c) which should exist in a frictionless environment. In a sense, the LSB technique allows us to model a controlled, drag-independent background environment at the expense of the *most realistic* possible background environment for a particular value of C_d.

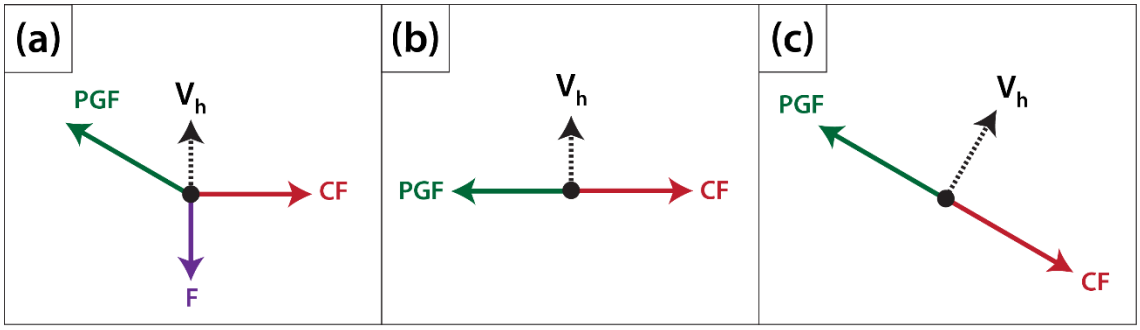

Fig. 5.1. Conceptual illustration of the horizontal force balance acting at the lowest grid point AGL using the LSB technique with $C_d = 0$. (a) The real three-force balance which exists in the observed sounding environment (green vector is the horizontal PGF; red vector is the Coriolis force; purple vector is the frictional force; dashed black vector is the horizontal wind). (b) The force balance in a simulation employing the LSB with $C_d = 0$ and using the observed sounding; the horizontal PGF is specified by the technique such that it offsets the Coriolis force. (c) Approximation of the force balance which would exist in nature if the local surface were frictionless; the PGF would remain the same as in (a), and the Coriolis force would modify to offset it in the case of geostrophic balance.

Note in (5.3) and (5.4) that we apply Coriolis to the full wind components in simulations using the LSB technique, rather than just the perturbation wind, as was the case in earlier simulations using the FBP. This is simply a technical detail inherent to the LSB methodology, and does not signify a physical difference in what we are simulating. Indeed, given the same initial sounding and drag coefficient, the LSB and

FBP are approximately equivalent[22]. Test simulations indicate that the two techniques applied properly to equivalent supercell simulations produce nearly identical results out to at least 2400 s (D. Dawson, personal communication).

5.1.2 Experiment design

In this chapter, five experiments are performed using the LSB technique. As in FWFRIC and EnvFRIC (from Chapter 3 and Chapter 4), the initial sounding for all experiments is MAY3B. MAY3B is the result of applying the FBP described in Section 3.1.2 to sounding MAY3, which was extracted from a real-data simulation in DA10. MAY3 itself was subject to a realistic three-force balance in the DA10 simulation, while MAY3B is known to contain a modest excess of near-ground shear due to the geostrophic assumption in the FBP (see Section 3.1.2). However, for continuity with FWFRIC and EnvFRIC, we nonetheless choose to employ MAY3B for the experiments in this chapter.

The experiments and their drag coefficients are summarized in Table 5.1. With respect to the drag coefficient, these experiments are intended to sample the parameter space spanned by real surfaces (land, water, and urban) over which supercells may exist in the real world. Experiment CD0 is the LSB-based equivalent to EnvFRIC; that is, drag does not act on storm perturbations in CD0, even though its background wind profile has resulted from drag. In the remaining experiments, drag does act on the storm perturbations, but the magnitude varies according to C_d. (Note: a simulation using C_d = 0.01 would be the LSB-based equivalent of FWFRIC.)

[22] Theoretically, they should be equivalent in the case that (a) the 1D simulation used for the balancing step in the FBP yields an output sounding wherein the Coriolis and mixing have come into precise balance; and (b) this output sounding is used to initialize the 3D storm simulations with both techniques.

Table 5.1. Drag coefficients for LSB experiments.

Experiment	**C_d**
CD0	0
CD2-3	0.002
CD5-3	0.005
CD2-2	0.02
CD5-2	0.05

5.2 Simulation results

5.2.1 Overview and qualitative analysis

Owing to their similar configuration, all five experiments evolve qualitatively similarly to FWFRIC and EnvFRIC for the first 600 s. As with those two experiments, subtle differences in the near-ground wind field begin to grow during the 600-1200 s period and ultimately lead to more qualitatively meaningful differences around 1500 s. Fig. 5.2a presents a time series of domainwide minimum perturbation pressure for the five experiments. All experiments with drag enabled feature pronounced pressure deficits of 40-80 hPa during the 1500-2200 s time period, and a tendency exists for the minima to appear earlier as the drag coefficient increases (e.g., CD2-2 reaches its minimum about 400 s before CD2-3). A time series of maximum storm-relative horizontal winds (Fig. 5.2b) exhibits a similar pattern in the experiments' maxima during this period. Following these initial extrema, all experiments exhibit relatively weak maximum winds and pressure deficits until about 3000 s. From 3000 s to the end of the integration period at 4800 s, each experiment has several distinct perturbation pressure minima, and correlation between the experiments becomes relatively weak;

inter-experiment differences have become quite nonlinear and complex by this time. The most striking feature of this period is that the no-drag (CD0) and weak-drag (CD2-3) experiments exhibit by far the largest maximum pressure deficits; the strong-drag (CD2-2 and CD5-2) experiments exhibit by far the weakest deficits; and CD5-3 falls roughly midway between those two groups (Fig. 5.2a). This stands in direct contrast to the pressure minima during the period before 2400 s. The storm features responsible for these discrepancies will now be shown and discussed.

Fig. 5.3 presents domainwide time-height cross sections from 0-3000 s of maximum updraft and vertical vorticity for the five experiments. The initial lowering of the mesocyclone from around 1500 m AGL toward the ground can be seen in the plots of updraft (Fig. 5.3a-f) to proceed earlier in the simulation as drag the coefficient increases. Similar to FWFRIC (as described in Chapter 3), large cyclonic vorticity develops explosively upward from the ground in all experiments except CD0 during the 1300-1800 s period (Fig. 5.3f-j). This process occurs progressively earlier with increasing drag coefficient from CD2-3 to CD2-2, but there is little difference in timing between CD2-2 and CD5-2. Based on these cross-sections, it appears that surface drag (with C_d of some value not larger than 0.002) is required in order for an intense low-level mesocyclone to develop during this early stage of the simulation, and that larger values generally hasten this process. However, at the high end of the sampled parameter space, there exist signs of an upper limit on favorability for intense low-level mesocyclogenesis somewhere in the range $0.02 < C_d < 0.05$. Although the lowering of the mesocyclone occurs slightly earlier in CD5-2 than in CD2-2, the maximum

mesocyclone updraft and vorticity are weaker overall in CD5-2, and intense rotation ($\zeta > 0.75\ s^{-1}$) does not extend above 300 m AGL (Fig. 5.3d-e, i-j).

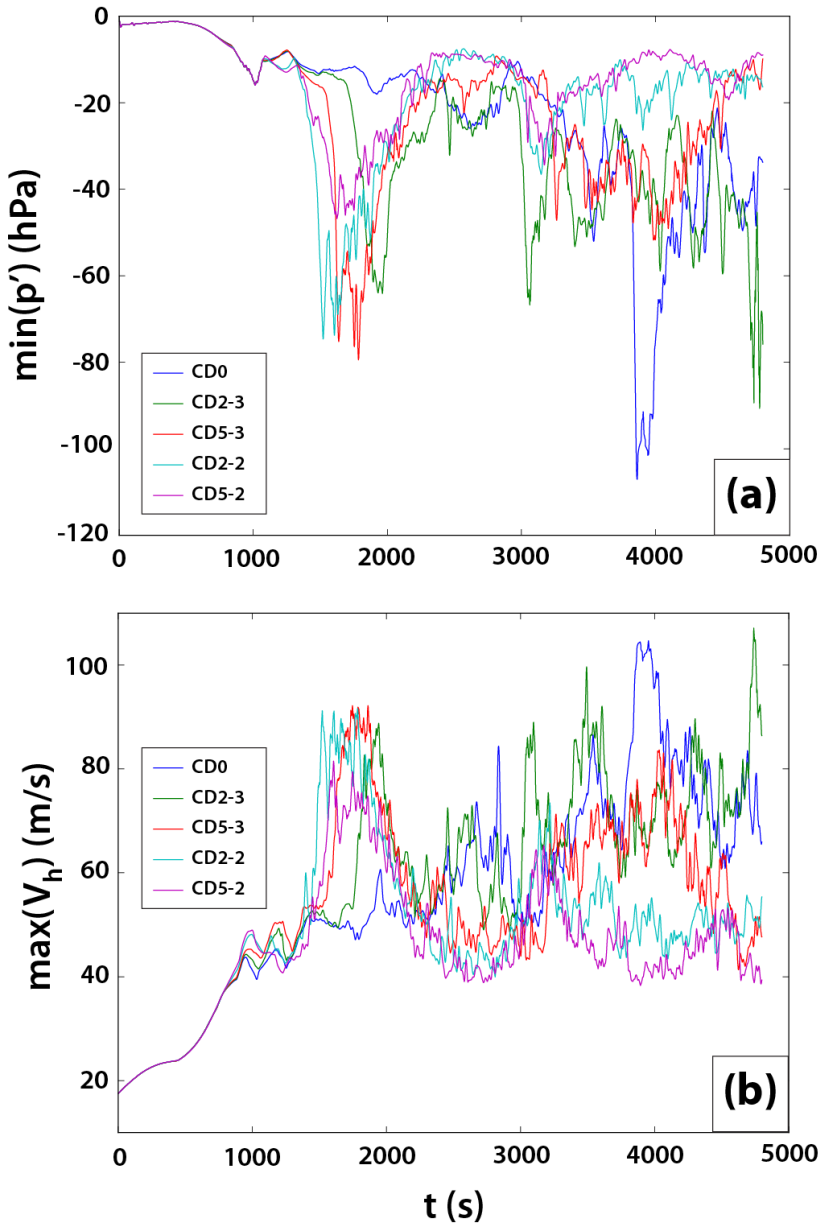

Fig. 5.2. Time series of domainwide (a) minimum perturbation pressure, and (b) maximum horizontal storm-relative wind speed, for the five LSB-based experiments between 0-4800 s.

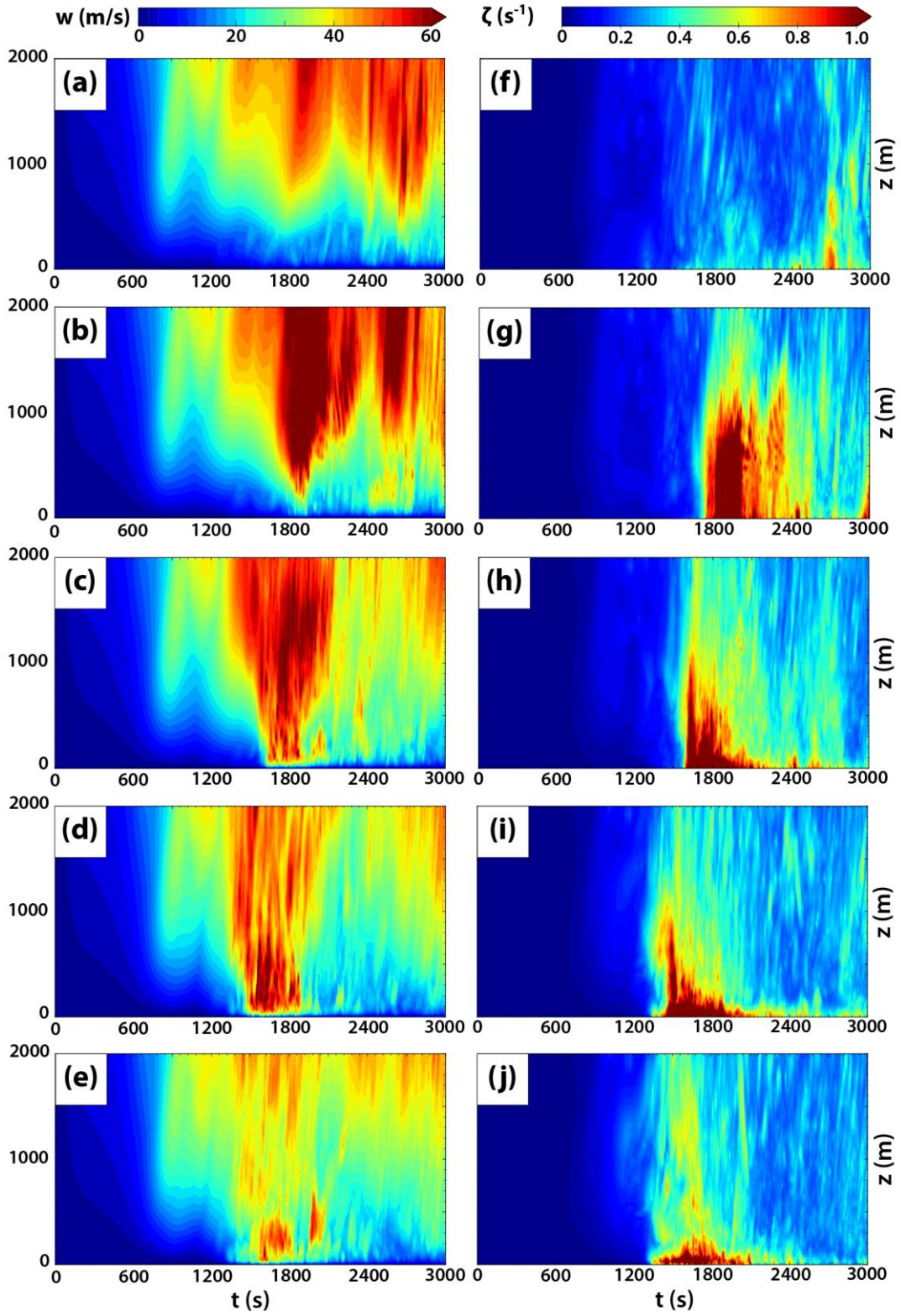

Fig. 5.3. Domainwide maximum time-height cross sections from 0-3000 s of updraft for (a) CD0, (b) CD2-3, (c) CD5-3, (d) CD2-2, and (e) CD5-2; and of vertical vorticity for (f) CD0, (g) CD2-3, (h) CD5-3, (d) CD2-2, and (e) CD5-2.

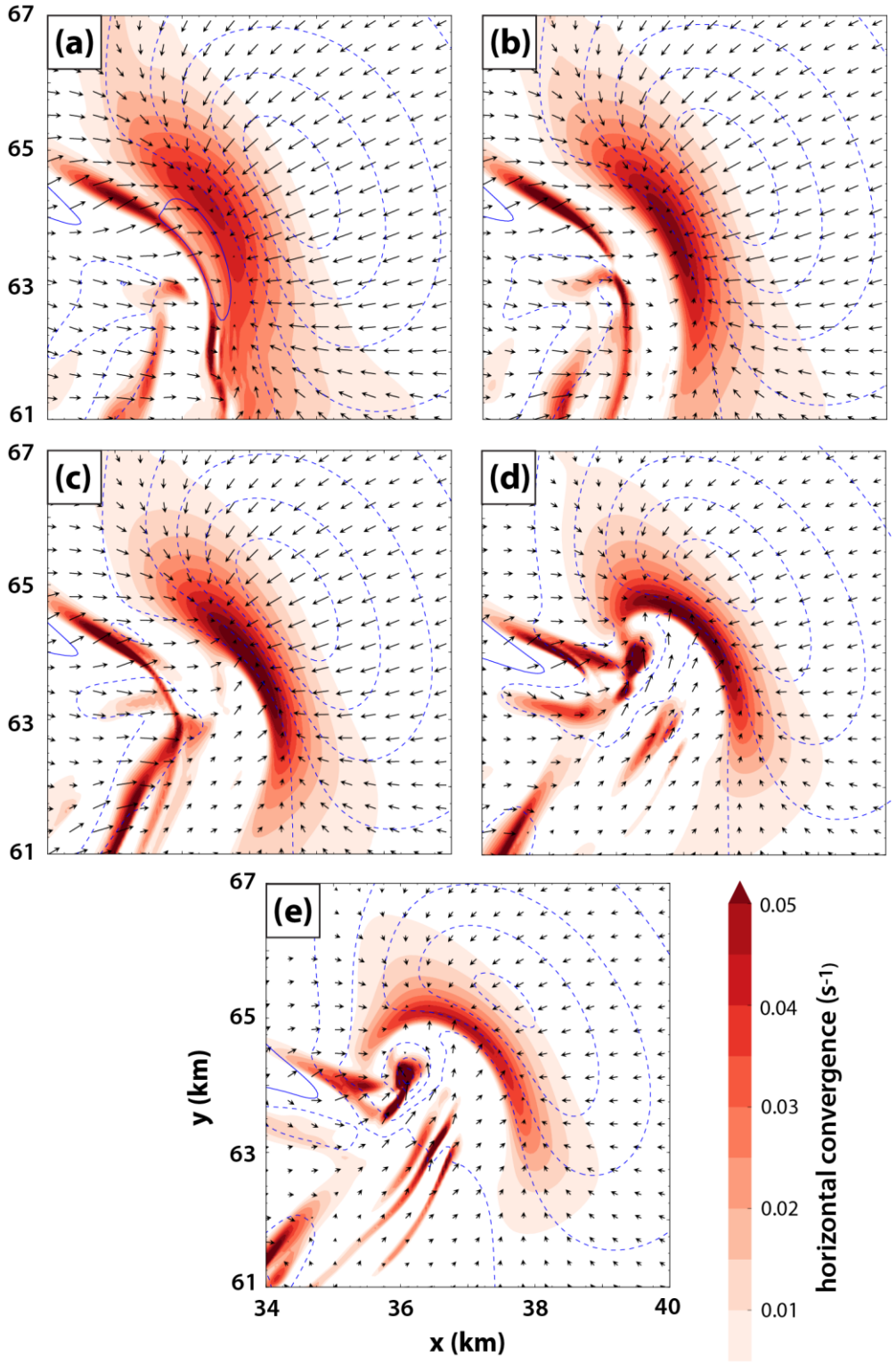

Fig. 5.4. Horizontal cross-section at 10 m AGL and 1320 s of horizontal convergence (shaded), perturbation pressure (blue dashed contours every 1 hPa for p' ≤ -1 hPa), and ground-relative wind vectors for (a) CD0, (b) CD2-3, (c) CD5-3, (d) CD2-2, and (e) CD5-2.

Horizontal cross-sections of horizontal convergence, perturbation pressure, and ground-relative wind vectors at 1320 s are presented in Fig. 5.4. In CD0, a broad zone of convergence is seen along the surface boundary, which is primarily north-south oriented and separates westerly and easterly flow on either side (Fig. 5.4a). As the drag coefficient increases in the remaining experiments, a few trends are noted. First, the surface boundary becomes progressively more curved along its northern extent around (x = 36 km, y = 65 km). Second, the convergence zone becomes more compact, with a larger maximum convergence magnitude at its center (except in CD5-2, where maximum convergence is weaker than in all other drag experiments). Third, the "inflow low" (denoted by the innermost perturbation pressure contour) east of the boundary becomes centered more toward the northwest. In CD2-2 and CD5-2, a strong pressure minimum associated with a developing tornado[23] can already be seen at this time near (x = 36 km, y = 64 km) (Fig. 5.4d-e). All of these trends largely mirror the discrepancies between EnvFRIC and FWFRIC analyzed in Section 3.2.1. The relatively orderly changes with increasing drag coefficient between CD0 and CD2-2 increase confidence that the early-simulation convergence boundary behavior in FWFRIC and EnvFRIC is predictable and representative of monotonic trends within the parameter space of drag coefficients (c.f. Fig. 3.4). By contrast, the markedly weaker convergence maximum in CD5-2 compared with CD2-2 is another indication that surface drag in CD5-2 is so strong as to inhibit processes leading to low-level mesocyclogenesis and tornadogenesis during this period. The ground-relative flow on both sides of the boundary, and particularly within the inflow east of the boundary, is so weak in CD5-2

[23] The criteria for identifying a tornado in the experiments herein will follow those in Chapter 3: a circular vortex with maximum storm-relative wind speeds of at least 29 m s^{-1} (EF-0), and maximum vertical vorticity of least 0.3 s^{-1}, at the lowest grid level AGL.

(Fig. 5.4e) that the resultant anemic low-level convergence proves detrimental to low-level updraft maintenance (Fig. 5.3e).

Fig. 5.5 displays horizontal cross-sections at 10 m AGL and 1800 s showing the state of the surface cold pool and the tornado (except in CD0, where no tornado is ongoing at 1800 s). The surface convergence boundary remains more north-south oriented in experiments with a smaller drag coefficient, whereas experiments with a larger coefficient tend to exhibit a strongly curved boundary that wraps into the tornado. It is noteworthy that relatively warm air resulting from a dynamically-driven downdraft south of the mesocyclone (e.g., centered near [x = 32 km, y = 63 km] in Fig. 5.5a) tends to wrap cyclonically around the mesocyclone and partially encircle the tornado in the experiments with larger drag coefficients, whereas the surface boundary south of the mesocyclone in CD0 (and, to a much lesser extent, CD2-3) appears to block this warm air from wrapping in.

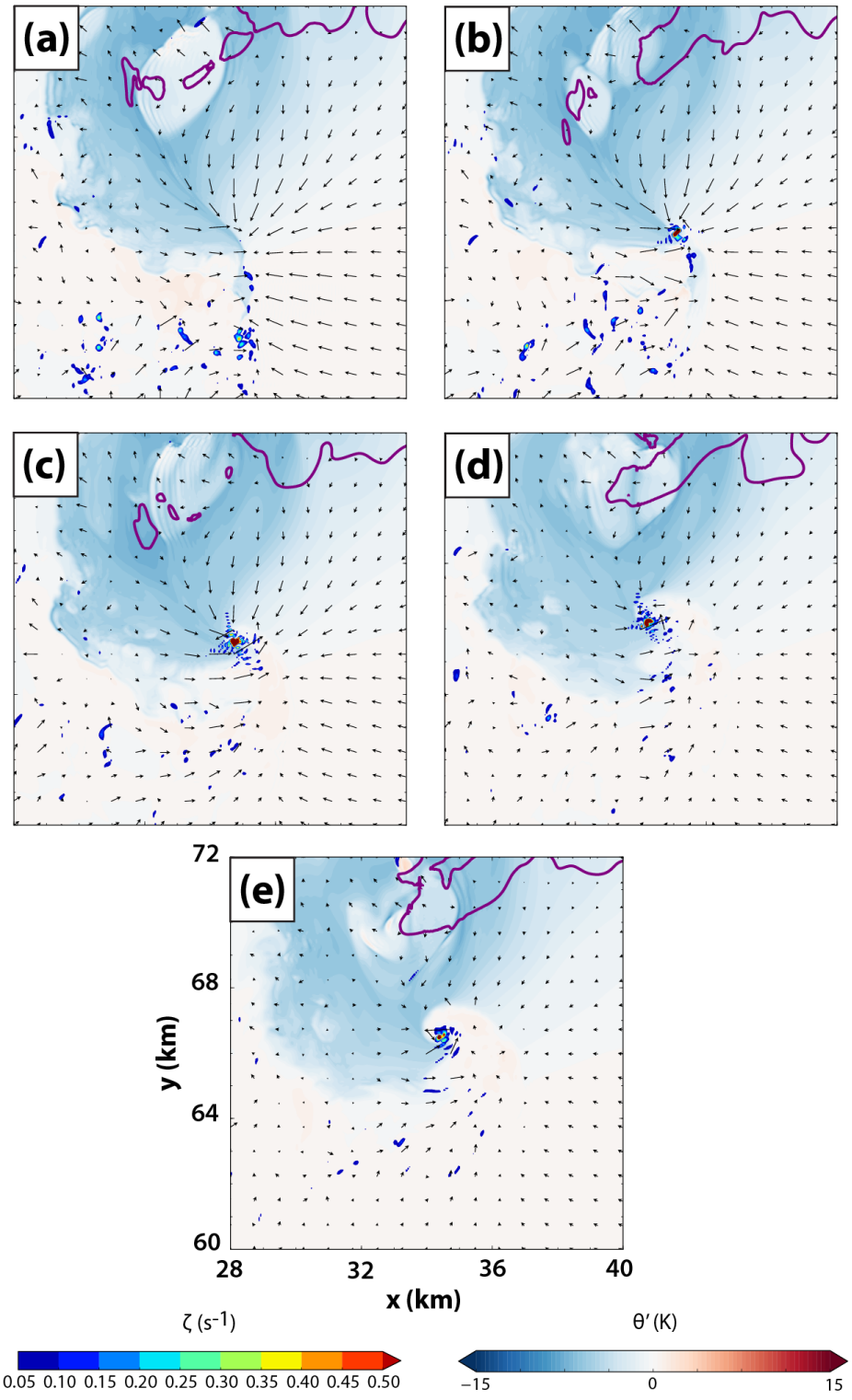

Fig. 5.5. Horizontal cross-section at 10 m AGL and 1800 s of perturbation potential temperature (shaded), cyclonic vorticity (shaded for $\zeta \geq 0.05$ s^{-1}), the 0.3 g kg^{-1} rainwater mixing ratio contour (purple), and ground-relative wind vectors for (a) CD0, (b) CD2-3, (c) CD5-3, (d) CD2-2, and (e) CD5-2.

Fig. 5.6 presents domainwide maximum time-height cross-sections for updraft and vertical vorticity for the period 2400-4800 s. After a lull in strong or persistent tornadic activity during the 2400-3000 s period, all experiments enter a second "cool regime" of tornado production beginning around 3000 s. This regime is characterized by tornadoes whose genesis occurs with cool outflow already in close proximity to (and, at times, even surrounding) the vortex. These tornadoes appear more similar to a typical supercell tornado documented by field experiments and observations, compared with the early-storm tornado around 1300-1800 s in the experiments with drag. Fig. 5.7 presents horizontal cross-sections equivalent to those in Fig. 5.5, but each panel is valid at an early time during the life cycle of the first "cool regime" tornado in an experiment. In all experiments, a mature RFD characterized by generally cool outflow has penetrated south of the tornado's location by this timeframe. Interestingly, the flow pattern discrepancy between experiments within the near-ground mesocyclone that was noted in Fig. 5.5 is still apparent: flow originating south of the tornado appears to wrap around cyclonically east of the vortex to a greater extent in the experiments with a large drag coefficient (Fig. 5.7d,e). Comparatively, the near-ground mesocyclone in CD0 (Fig. 5.7a) is characterized by sharp convergence boundaries separating several distinct, coherent horizontal flows. The smoothly "spiraling" flow regime around the near-ground mesocyclone apparent in CD2-2 and CD5-2 is a result expected at the tornado scale when surface friction upsets cyclostrophic balance and turns flow radially inward (Trapp 2000); in the present study, a similar change seems to occur at a somewhat broader scale, on the order of 2-5 km in the horizontal. This phenomenon was discussed in Section 3.2.1 during the period when the first low-level mesocyclone in FWFRIC and

EnvFRIC was in its developing stages (900-1300 s), but appears also to occur with later mesocyclones in CD2-2 and CD5-2.

In general, increasing the drag coefficient appears to result in faster cycling of low-level mesocyclones for our experiments. Fig. 5.8 presents horizontal cross-sections from CD0 and CD2-2 which illustrate this trend. In CD2-2, low-level circulations tend to develop and move rearward (in a storm-relative sense) after a few minutes, becoming horizontally displaced westward from the main storm updraft; meanwhile, a new circulation begins developing back to the east beneath the main updraft before dissipation of the old circulation is complete (Fig. 5.8a-b). By contrast, in CD0, there is no sign of cyclic mesocyclogenesis; the primary (strongest) tornado is quite long-lived (Fig. 5.8c-d), and weaker tornadoes earlier and later in the simulation form in the same storm-relative area at the intersection of the FFGF and RFGF (not shown). These results are in direct conflict with those reported by Adlerman and Droegemeier (2002) (hereafter AD02), to the extent that their simulated storm can be compared with the storm in our simulations. AD02 found that increasing the drag coefficient *decreased* the frequency of mesocyclone cycling; this was true over a range of four C_d values, and regardless of whether ice or warm rain microphysics were employed. The simulations in AD02 used the 20 May 1977 Del City sounding, were much coarser in the horizontal (500-m grid spacing) and vertical (100-m grid spacing near the ground), and employed a different experimental design wherein friction was applied *only* to perturbations. Even despite these differences, it is somewhat surprising and noteworthy that our results regarding mesocyclone cycling are diametrically opposed. The tornadoes in CD0 appear to remain immediately along the sharp surface convergence boundary throughout their

life cycles; in CD2-2 and CD5-2, these boundaries are less defined (after the initial cycle around 1300-1800 s), and tornadoes tend to continue unabated as they move well behind the RFGF within the RFD. The type of mesocyclogenesis seen in the strong-drag experiments is most consistent with the occluding mode described in Adlerman and Droegemeier (2005) with old circulations retreating rearward into the RFD, rather than shifting south along the RFGF.

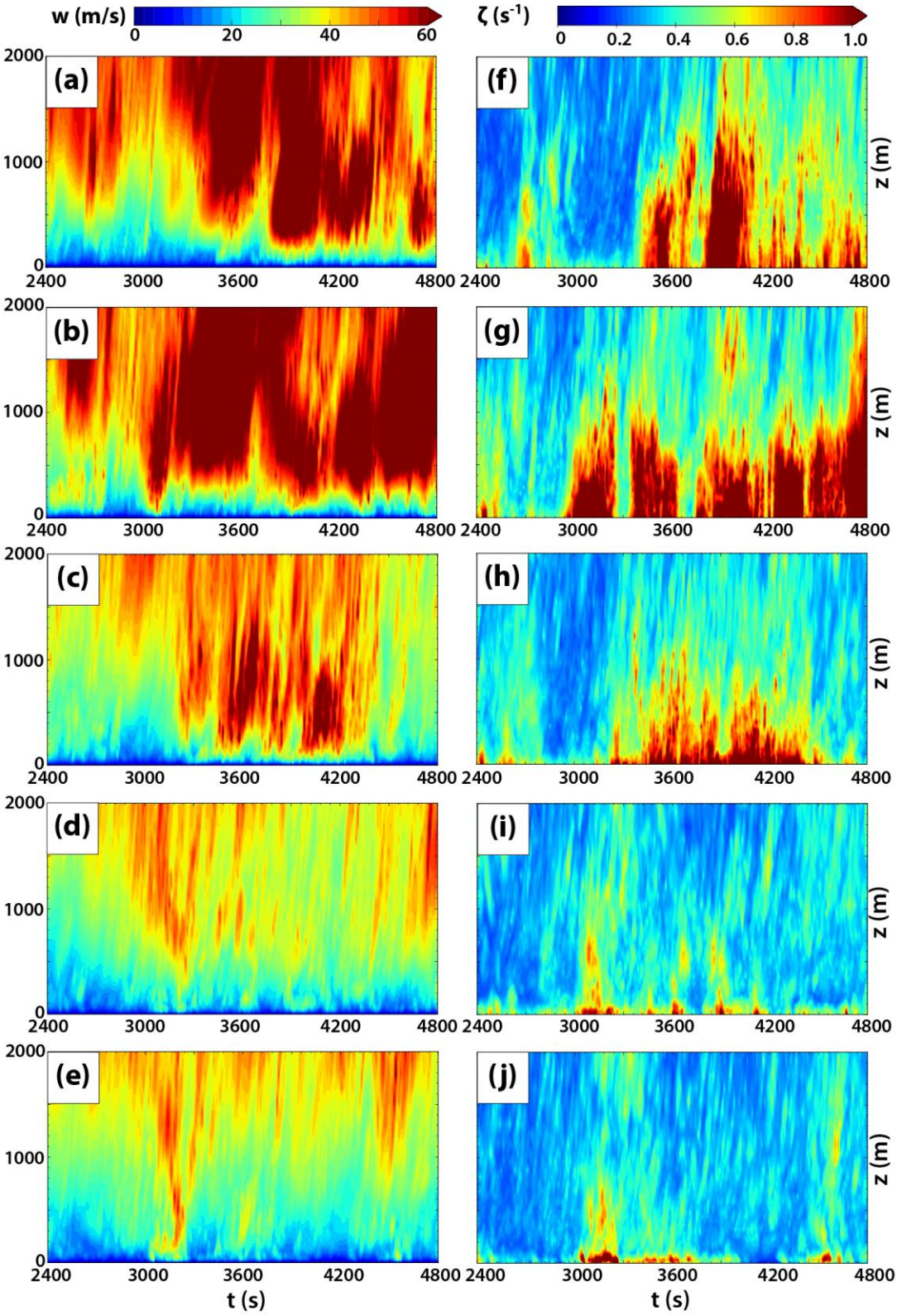

Fig. 5.6. As in Fig. 5.3, but for the period 2400-4800 s.

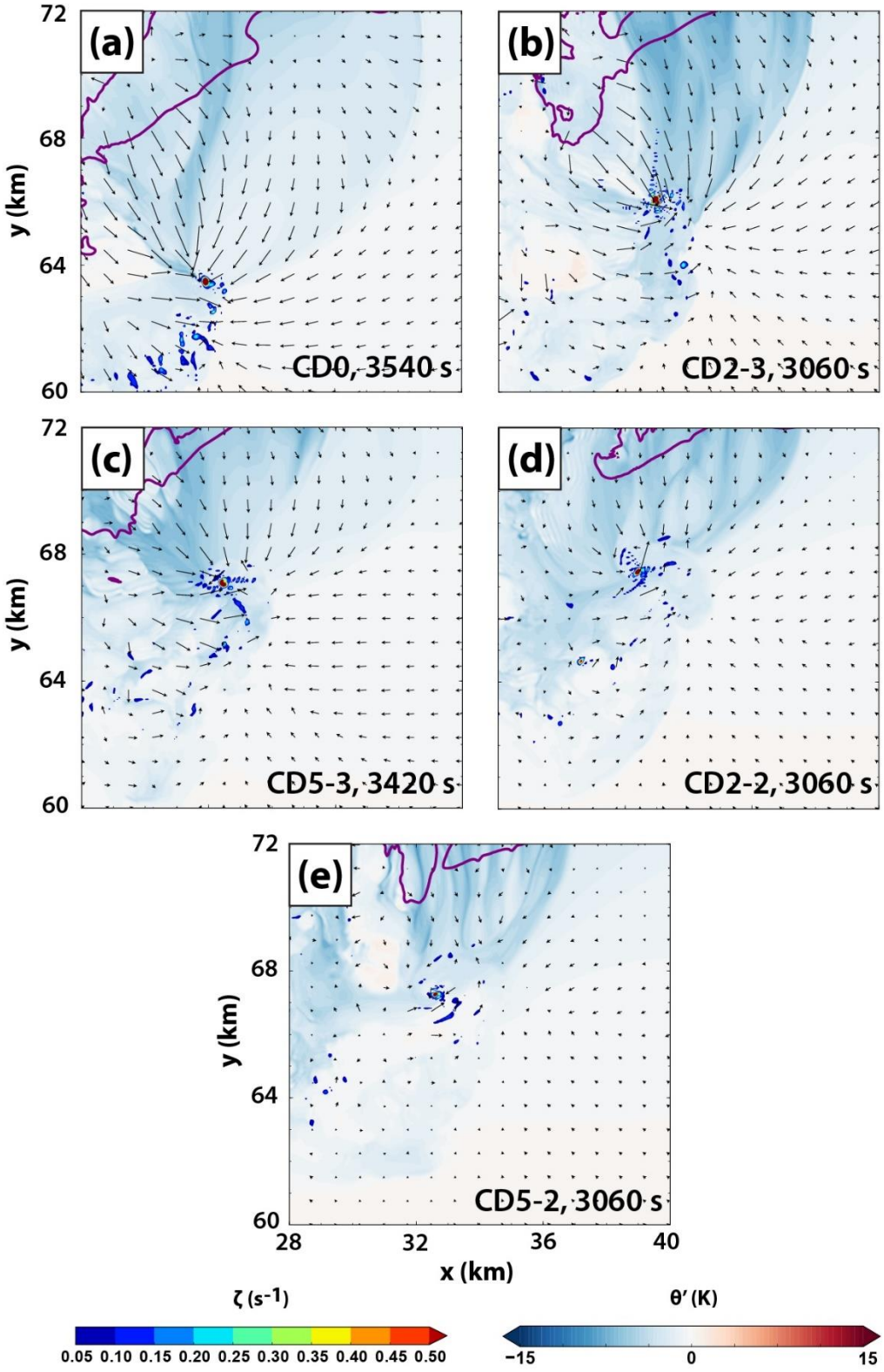

Fig. 5.7. As in Fig. 5.5, except at (a) 3540 s, (b) 3060 s, (c) 3420 s, (d) 3060 s, and (e) 3060 s.

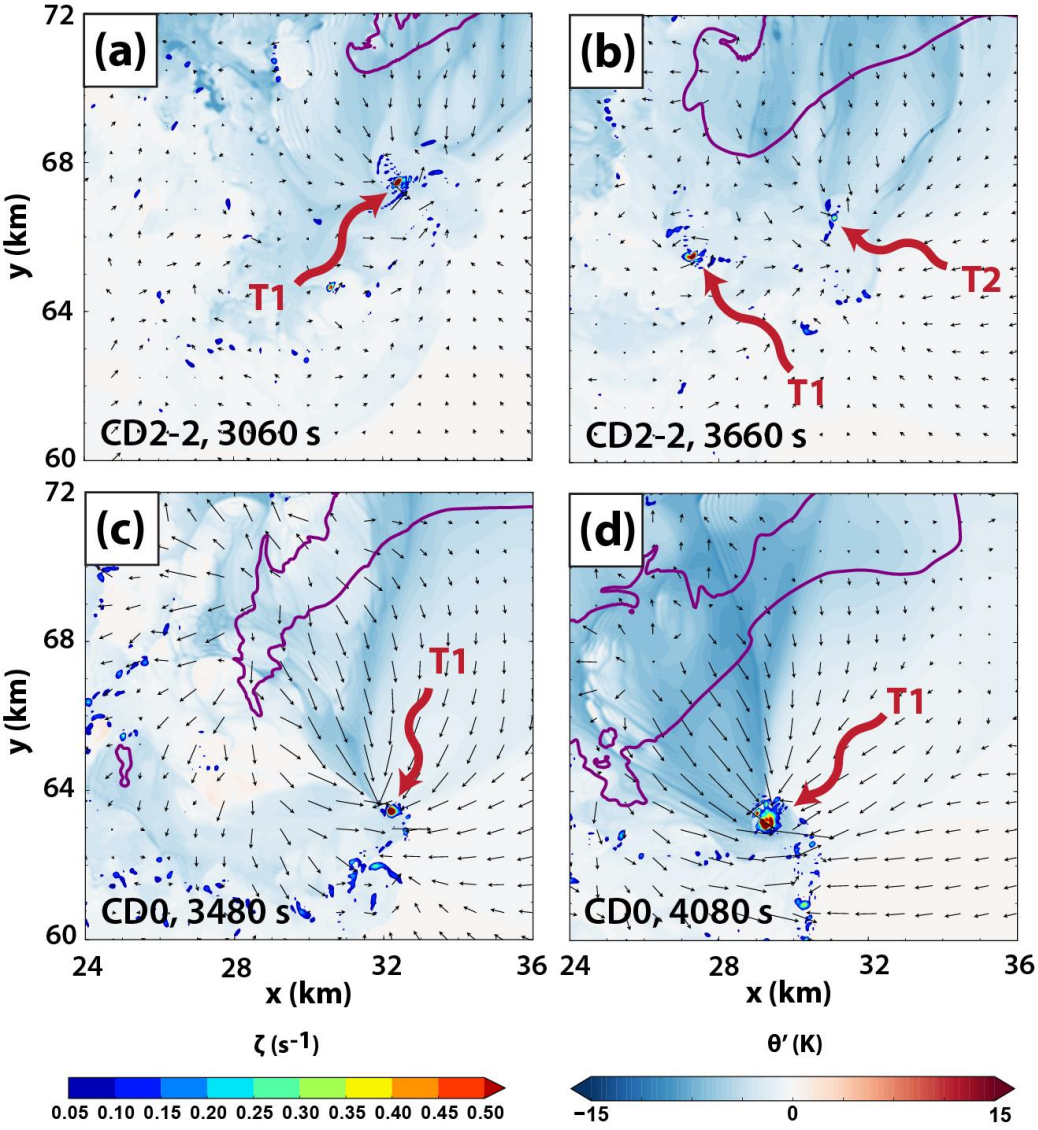

Fig. 5.8. Horizontal cross-section at 10 m AGL and 1800 s of perturbation potential temperature (shaded), cyclonic vorticity (shaded for $\zeta \geq 0.05$ s^{-1}), the 0.3 g kg^{-1} rainwater mixing ratio contour (purple), and ground-relative wind vectors for (a) CD0 at 3480 s, (b) CD0 at 4080 s, (c) CD2-2 at 3060 s, and (d) CD2-2 at 3660 s. In (a)-(b), the first tornado of the post-3000 s period in CD2-2 is denoted by T1, and the second tornado of this period is denoted by T2. In (c)-(d), the first tornado of the post-3000 s period in CD0 is denoted by T1.

5.2.2 Tornado structure

Because this is the first three-dimensional storm-scale modeling study (to the author's knowledge) to vary the drag coefficient in a controlled manner, use grid spacing of O(50 m), and investigate tornadoes, it is of interest to examine how the

tornado-scale structure (to the extent it is resolved on our grid) varies among our experiments. Fig. 5.9 presents vertical cross-sections of updraft, vertical vorticity, and wind vectors through the first tornado occurring in the drag experiments (CD2-3, CD5-3, CD2-2, and CD5-3). Note that the x-z cross-sections are manually chosen to bisect the center of the tornado at 10 m AGL for each experiment and time. Although the cross-sections are taken near the time of peak tornado intensity (by vorticity magnitude) for each experiment, it must be cautioned that some discrepancies between experiments may be time-dependent, or otherwise related to storm-scale differences not directly tied to the vortex's interaction with the lower boundary. Nonetheless, "corner flow" (Rotunno 1977; Lewellen et al. 2000) appears more pronounced in CD2-2 and CD5-2 (Fig. 5.9c-d) than in CD2-3 and CD5-3 (Fig. 5.9a-b). Consequently, strong (>30 m s^{-1}) updraft within the vortex tends to extend downward nearer the ground in the experiments with a larger drag coefficient. In CD2-3, which uses the weakest nonzero drag coefficient, the tornado's primary updraft (near x = 34.7 km) is elevated and fed by flow which turns upward with a relatively large radius; vertical velocity >30 m s^{-1} only occurs above 200 m AGL (Fig. 5.9a). Evidence of marginally resolved multi-vortex structure exists to varying degrees in CD5-3 (Fig. 5.9b) and CD2-2 (Fig. 5.9c); by contrast, the tornado in CD5-2 features a core axial updraft, supported by flow at the lowest grid level AGL converging sharply from the east and west (Fig. 5.9d).

Fig. 5.10 presents vertical cross-sections through tornadoes in CD0 and CD2-3 which occur during the cool-tornado regime (the other experiments did not produce strong, vertically-deep tornadoes in this regime). The tornado in CD0 exhibits clear two-cell structure, characterized by an axial downdraft and dual vorticity maxima on

either zonal side of the vortex (Fig. 5.10a). By contrast, the tornado is CD2-3 exhibits updraft at its core up to about 500 m AGL (above which a weak central downdraft exists), coincident with a strong cyclonic vorticity maximum.

The trends in corner flow and tornado-scale updraft behavior seen within the C_d parameter space in our experiments are broadly in agreement with Trapp (2000) (hereafter T00), who performed idealized axisymmetric vortex simulations with free-slip and no-slip boundary conditions. A key finding in T00 was that an axial (central) downdraft penetrated to the surface in their free-slip simulation, but was dislodged aloft in their no-slip simulation by an intense axial jet erupting upward from the ground. Radial inflow resulting from surface friction disrupting cyclostrophic balance gives rise to this axial jet (Bluestein 2007); with all other variables held constant, larger drag coefficients should tend to enhance this effect, as the magnitude of the frictional force increases relative to other forces acting on near-ground parcels at the periphery of the vortex. Indeed, we see strong updrafts which develop very near the ground in CD2-2 and CD5-2; these differences from the weak-drag and no-drag experiments are also evidenced in the time-height sections (Fig. 5.3a-e, Fig. 5.6a-e), which reveal stronger updraft below 100 m AGL in CD2-2 and CD5-2 even during the cool regime tornado period, when those experiments produce tornadoes substantially weaker than the tornadoes in CD0 (Fig. 5.6a,d-e). The shallower vertical nature of the cool regime tornadoes in CD2-2 and CD5-2 (e.g., Fig. 5.6f-j) appears to be primarily due to their tendency to intensify while horizontally displaced west of the main storm updraft, rather than a direct result of their interaction with the frictional surface, but future work should clarify this.

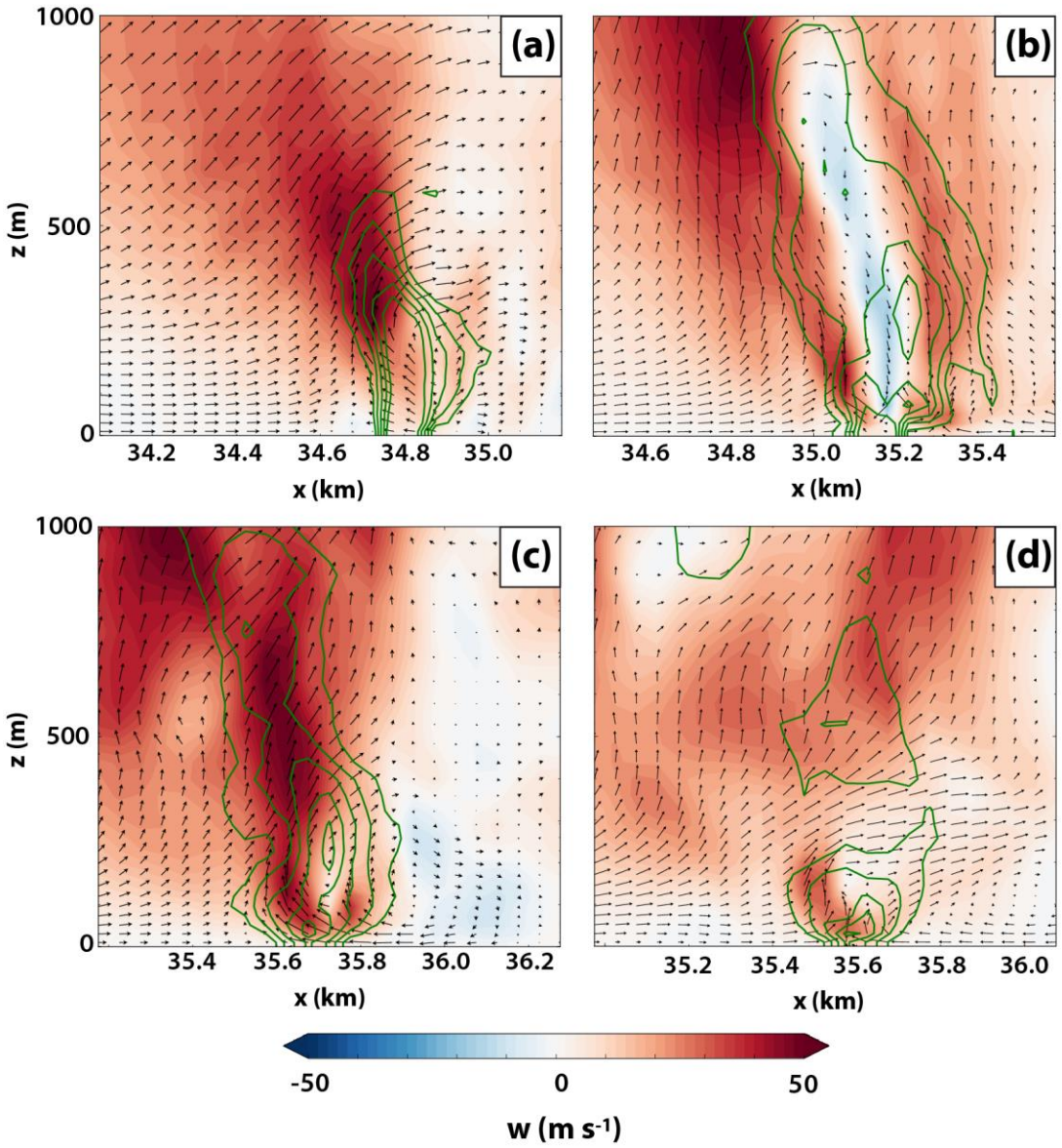

Fig. 5.9. Vertical cross-section in the x-z plane of vertical velocity (shaded), vertical vorticity (green contours every 0.2 s^{-1} for $\zeta \geq 0.2$ s^{-1}), and ground-relative wind vectors for (a) CD2-3 at 1860 s along y = 65275 m, (b) CD5-3 at 1680 s along y = 65325 m, (c) CD2-2 at 1500 s along y = 65225 m, and (d) C5-2 at 1500 s along y = 65225 m.

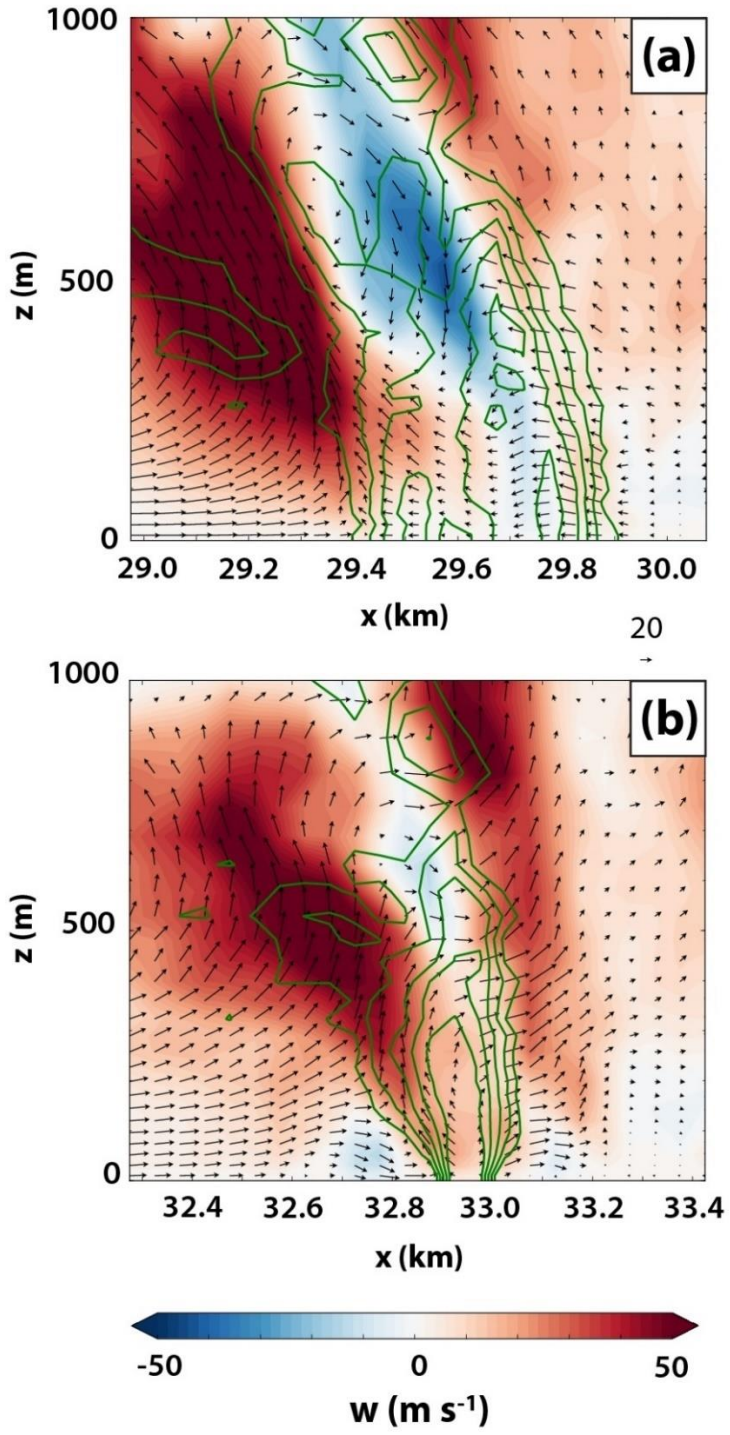

Fig. 5.10. As in Fig. 5.9, except for (a) CD0 at 3960 s along y = 63375 m, and (b) CD2-3 at 3120 s along y = 65625 m.

5.2.3 Circulation analysis of early mesocyclone

In order to examine the dynamics of mesocyclone intensification, material circuits will once again be employed, as in Section 4.2.2. In this case, it is of particular interest to determine whether the contribution to mesocyclone circulation from surface drag increases in an orderly fashion as the drag coefficient increases. The procedure for initializing the circuits, as well as for calculating circulation and its forcing terms along the circuit, is the same as in Section 4.2.2. As a brief review: horizontal circular circuits of radius 1.5 km are initialized centered on the low-level mesocyclone (determined subjectively from the model wind field) with parcels approximately 19 m apart. These parcels are integrated backward in time as trajectories; when the distance between adjacent parcels exceeds 25 m after an integration time step, a new parcel is added to the circuit at the midpoint of the line segment connecting those parcels, and is then included at all subsequent (backward) time steps. We integrate circuits backward in time for 10 min (600 s) at a time step of 0.5 s (afforded by linear temporal interpolation of the wind between model data files, which are available every 2 s). After integration, the relevant state variables are interpolated to parcel locations to find circulation and its forcing terms (baroclinic and mixing; see Section 4.2.2 for details) at each model data time (every 2 s).

In the present study, we initialize circuits for each experiment across an array of initial heights and circuit times. For each experiment, we initialize a circuit at three heights (500 m, 1000 m, and 2000 m AGL) at four times (1200 s, 1260 s, 1320 s, 1380 s); this yields 12 circuits per experiment, and 60 total circuits. Our goal is to track how the forcing terms affect the low-level mesocyclone circulation during its period of initial

intensification. Fig. 5.11 presents time series of the integrated contributions from the mixing (solid) and baroclinic (dashed) forcing terms, normalized by the total circulation about each circuit. It should be emphasized that each data point in Fig. 5.11 represents the total contribution from mixing over the preceding 10 min for a unique circuit; for each experiment, the plotted time series is composed of contributions from four distinct circuits initialized at different times (1200 s, 1260 s, 1320 s, and 1380 s). At 500 m AGL (Fig. 5.11a), the mixing term imposes a net negative contribution of 15-25% of the mesocyclone's final circulation for each of the initialization times in experiments CD0 and CD2-3; these contributions remain relatively steady over the period. By contrast, the mesocyclone in CD5-3, CD2-2, and CD5-2 sees an increased contribution with time from the mixing term during this period. The contribution at 1200 s is weakly negative for CD5-3, but becomes weakly positive by 1380 s. For CD2-2 and CD5-2, the mixing contribution at 1200 s is negligible, but grows increasingly positive with time; by 1380 s, mixing generation accounts for more than 40% of the circuits' circulation. In all experiments and at all times, the contribution from baroclinity is negligible, accounting for no more than 10% (negative or positive) of the final circulation.

The trend for the mixing term to provide a more positive contribution to circulation as C_d increases is expected, based on the mechanism identified in Chapter 4 wherein surface drag slows the southwestward-directed momentum of near-ground inflow parcels. To verify the physical mechanisms responsible for the mixing term's contributions in Fig. 5.11, three-dimensional circuits are plotted in Fig. 5.12, with each inter-parcel segment shaded by its local contribution to the mixing term (as in Fig. 4.8). The circuits plotted are those initialized around the mesocyclone at 1380 s and 500 m

AGL in each experiment; the plot time is 1140 s (4 min into the circuits' backward integration). As seen in circulation budgets for these circuits (Fig. 5.13), the magnitude of the mixing term tends to be maximized around this time (1140 s), whether its values are predominantly positive (CD2-3, CD2-2, and CD5-2) or negative (CD0 and CD2-3) during the integration window. It is apparent in Fig. 5.12 that the circuits in all five experiments contain a long segment lying near the ground toward their southeastern extent, similar to circuits previously analyzed in EnvFRIC and FWFRIC (c.f. Fig. 4.9). Along this near-ground segment, which lies in the inflow region east of the mesocyclone, the sign of the local contribution to the mixing term for each experiment mirrors the predominant sign seen in Fig. 5.11a and Fig. 5.13 for the circuit as a whole (in all experiments, other relatively large values are seen locally in the higher portions of the circuit toward its northwestern extent, but these tend to manifest as dipoles with opposite signs on the upward- and downward-directed circuit segments). Thus, the near-ground circuit segment in the inflow region appears largely responsible for the total forcing from mixing in each experiment, implicating the effects of surface drag (or lack thereof, in CD0). These circulation budgets further corroborate the mechanism from Chapter 4 (e.g., Fig. 4.15) and verify its presence over the C_d parameter space we examine herein: in CD5-3, CD2-2, and CD5-2, surface drag is acting against southwestward-directed near-ground flow in the inflow region, which retards flow that is locally consistent with clockwise (negative) circulation about the circuit. The same mechanisms are represented in the circuits at 1000 m AGL, but constitute a relatively smaller portion of the final circulation (Fig. 5.11b); at 2000 m AGL, mixing has only a modest impact on circulation overall (Fig. 5.11c).

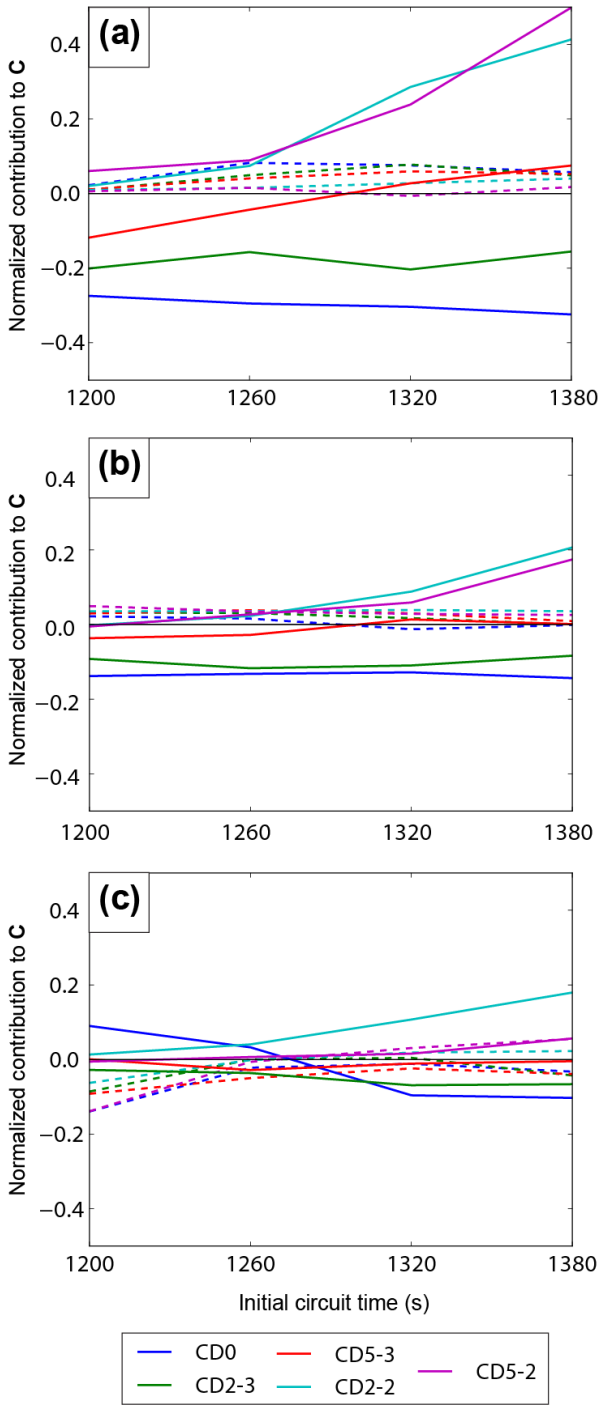

Fig. 5.11. Time series of normalized contribution to total circuit circulation from mixing (solid) and baroclinic (dashed) forcing terms for circuits initialized at (a) 500 m AGL, (b) 1000 m AGL, and (c) 2000 m AGL. Time on the abscissa represents when the mesocyclone-enclosing circuit was initialized. The forcing contributions occurred over the 10 min period prior to the circuit initialization (e.g., 600-1200 s for a circuit initialized at 1200 s). The magnitude of the contribution is normalized by the total circulation at the circuit initialization time, and therefore represents a fraction of the final circuit circulation.

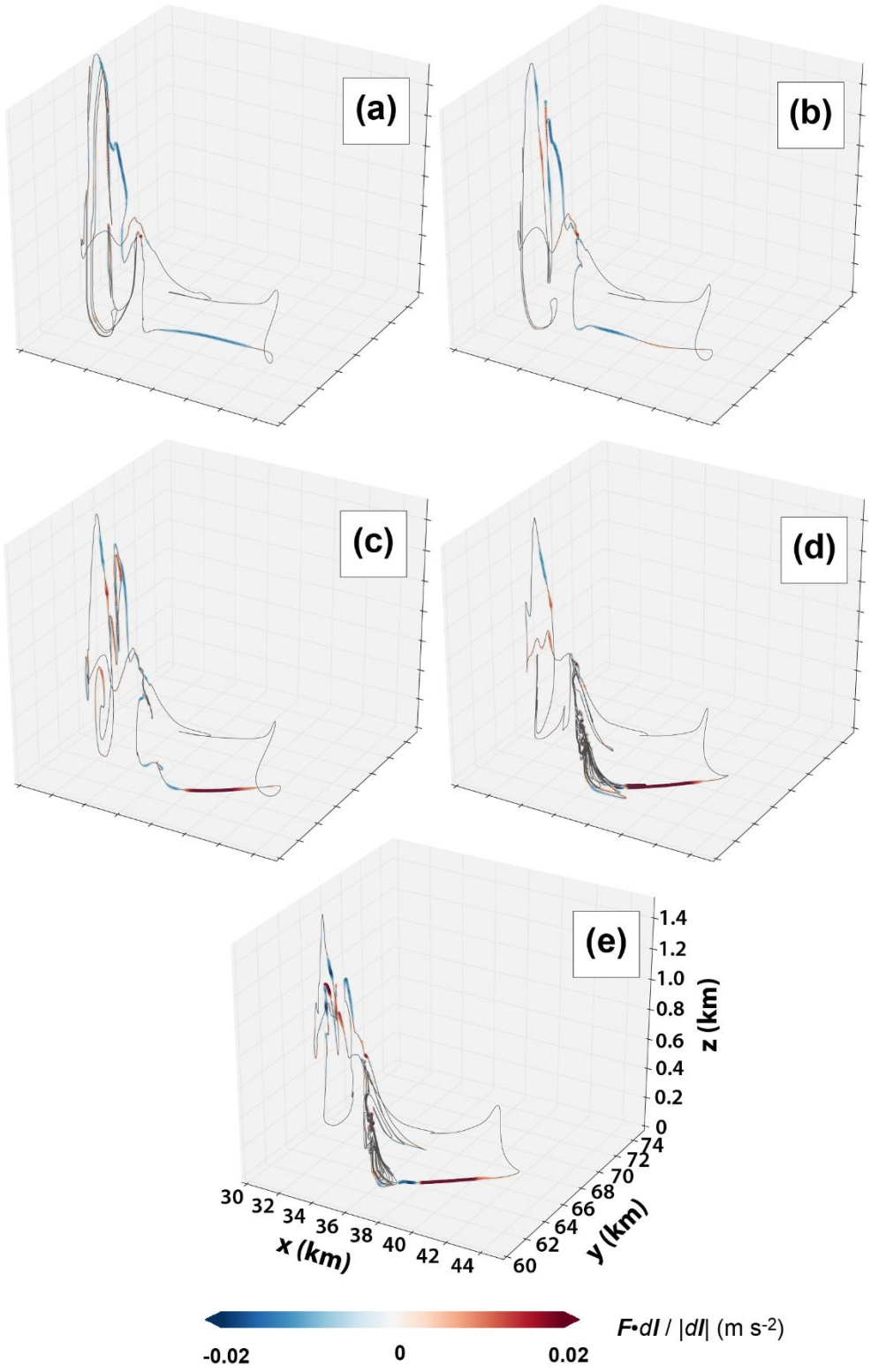

Fig. 5.12. For circuits initialized at 1380 s and 500 m AGL, the circuit position at 1140 s is plotted for the circuit in (a) CD0, (b) CD2-3, (c) CD5-3, (d) CD2-2, and (e) CD5-2. Parcels are colored by $\mathbf{F}\cdot d\mathbf{l}/|d\mathbf{l}|$ (the "mixing term") for the adjacent circuit segment, which represents the local contribution to $\mathbf{F}\cdot d\mathbf{l}$ for that segment.

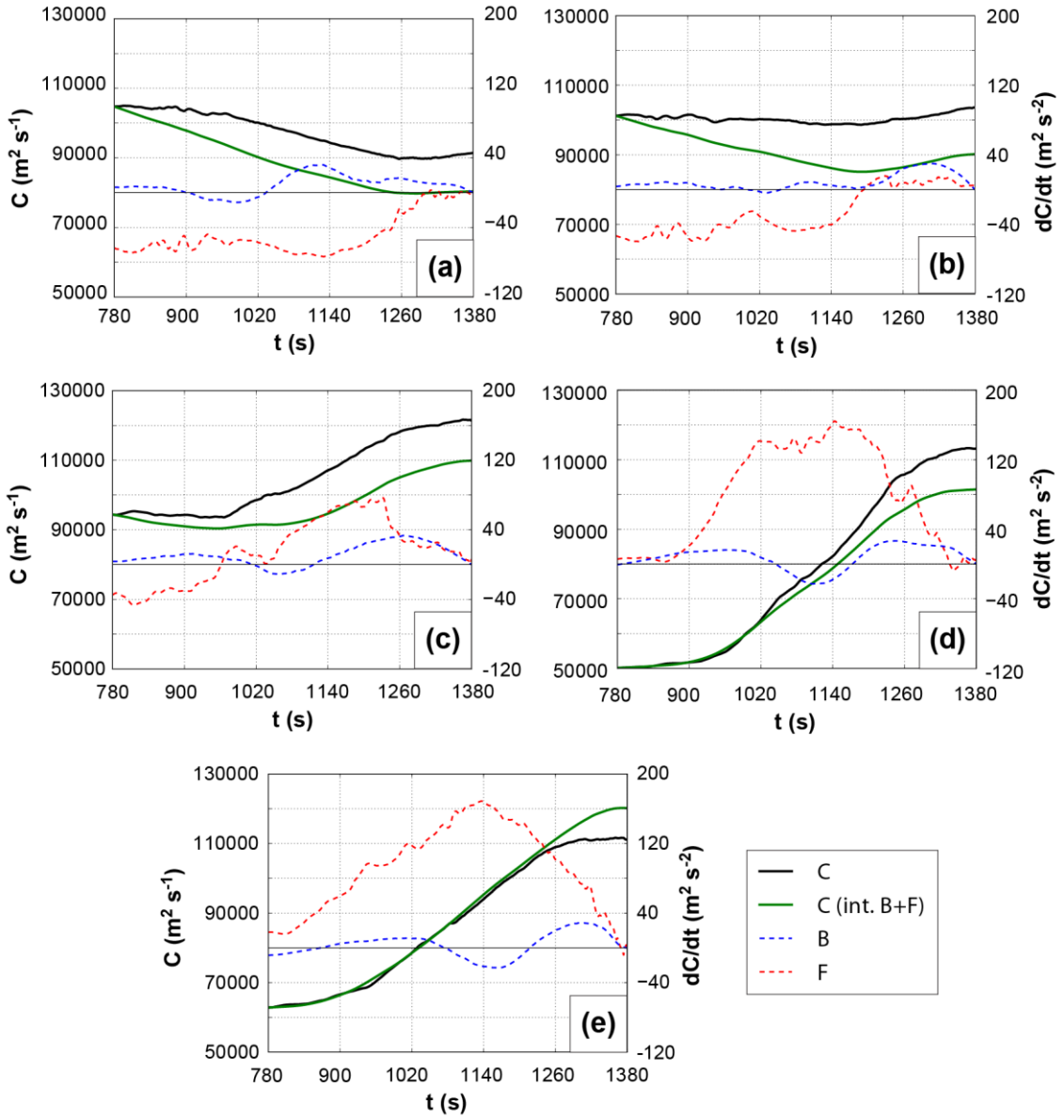

Fig. 5.13. Time series of interpolated circulation (solid black), circulation integrated from source terms (solid green), baroclinic forcing term (dashed blue), and mixing forcing term (dashed red) for the circuits in Fig. 5.12; (a-e) correspond to the circuits described therein. The values plotted here are budgets valid along the same circuit as it evolves in time (unlike in Fig. 5.11, where each time represents values from a different circuit). The left axis is for the interpolated and integrated circulation, while the right axis is for the forcing terms.

A noteworthy result is that, in the absence of drag, mixing imposes a *substantial* negative contribution to the final circulation at 500-1000 m AGL in CD0, and even to a lesser extent in CD2-3. As discussed in Section 4.2.2 and in M16 (see their Fig. 24),

internal mixing acts to dampen local vorticity maxima (e.g., the large horizontal vorticity in the inflow region east of the mesocyclone). The budgets at 500 m AGL for CD0 suggest this effect can act to reduce the circuits' circulation by as much as 25-30%. This provides a baseline which puts the mixing contribution for the other experiments into context: in experiments CD2-2 and CD5-2, where the mixing term provides a 40-50% *positive* net contribution to circulation, the final circulation may be as much as 150% larger than would be expected in the absence of drag. Furthermore, in CD5-3, mixing has only a small positive contribution to the mesocyclone circulation at 1380 s; in such a case, surface drag is still generating substantial circulation (e.g., Fig. 5.12c), but it is mostly offset by the diffusive effects of internal mixing. One caveat to interpreting the mixing forcing in CD0 as a "baseline" for the other experiments is that agreement between its circuit's interpolated and integrated circulation budgets is only modest, with the integrated budget undershooting the interpolated values substantially by the end of the integration window; the negative contribution from mixing could therefore potentially be overestimated (Fig. 5.13a).

5.2.4 Role of surface drag in cool regime tornadoes

The development of tornadoes within the cool regime (after 3000 s, characterized by a mature RFD) in all five experiments provides a valuable opportunity to evaluate how surface drag impacts tornadoes whose storm-relative contexts more closely resemble a typical supercell tornado in nature. To this end, material circuits are initialized within and immediately surrounding cool regime tornadoes in three experiments: CD0, CD2-3, and CD2-2. The wind field within and near the low-level mesocyclone during the cool regime is considerably more heterogeneous and complex

than is seen during the genesis of the early-storm mesocyclone and tornado (c.f. Fig. 5.5, Fig. 5.7). As a result, material circuits initialized surrounding incipient tornadoes in CD0 and CD2-3 are unable to complete backward integration of more than 2-3 min before spatial distortion becomes so extreme that O(100000) new parcels are required at each time step; thus, integration was aborted for these circuits. In CD2-2, material circuits are initialized surrounding a pre-tornadic vortex (PTV) at 2820 s at heights of 100 m AGL and 400 m AGL, then successfully integrated backward in time for 300 s (5 min). Fig. 5.14 presents the storm-relative context (Fig. 5.14a,d) and circulation budgets (Fig. 5.14b-c, e-f) for these two circuits. For the circuit initialized at 100 m AGL, circulation nearly doubles over the 5-min integration window, and this owes to the mixing term (Fig. 5.14b) which is large and positive during the first 3 min of the window (Fig. 5.14c); the baroclinic term has a weakly negative net contribution. For the circuit initialized at 400 m AGL, a modest circulation increase of around 10% is seen during the integration window, again owing entirely to the mixing term (Fig. 5.14e,f).

For the circuit initialized at 100 m AGL, a three-dimensional view of the circuit at 2580 s (Fig. 5.15a; 3 min before initialization), along with a horizontal cross-section at 100 m AGL (Fig. 5.15b), confirms that the mixing term is once again producing large positive circulation near the ground in the inflow sector east of the PTV. Crucially, this suggests surface drag may still be contributing a substantial portion of the near-ground mesocyclone (and likely PTV) vorticity during the cool regime in CD2-2. By this time, some of the storm characteristics from the early mesocyclone period analyzed in Section 5.2.3 (and Chapter 3-Chapter 4) which differ from a typical supercell tornadogenesis configuration are no longer present. The inflow sector east of the low-

level mesocyclone contains some thermal perturbations which have emanated from the FFD, making it more heterogeneous than in the early mesocyclone period; furthermore, the PTV occurs during the second distinct mesocyclone cycle in CD2-2, so there is no concern that the initial thermal bubble (which we use to initiate convection) meaningfully influenced its development. For the circuit initialized at 400 m AGL, the mixing contribution is positive but modest during the 5-min integration window (Fig. 5.14e-f); the relatively small change in total circulation during the window suggests any important generation processes likely occurred earlier in the simulation, when the circuit becomes too distorted for meaningful budget calculations. Overall, the cool regime of tornado production in the experiments herein is characterized by large trajectory error growth for parcels initialized in and around tornadoes and integrated backward in time, limiting the scope and confidence of our conclusions at this time. In order to elucidate the dynamics over a preceding period of tens of minutes lending to large cyclonic vorticity in these tornadoes, future work will need to address this challenging problem (Dahl et al. 2012) in new ways.

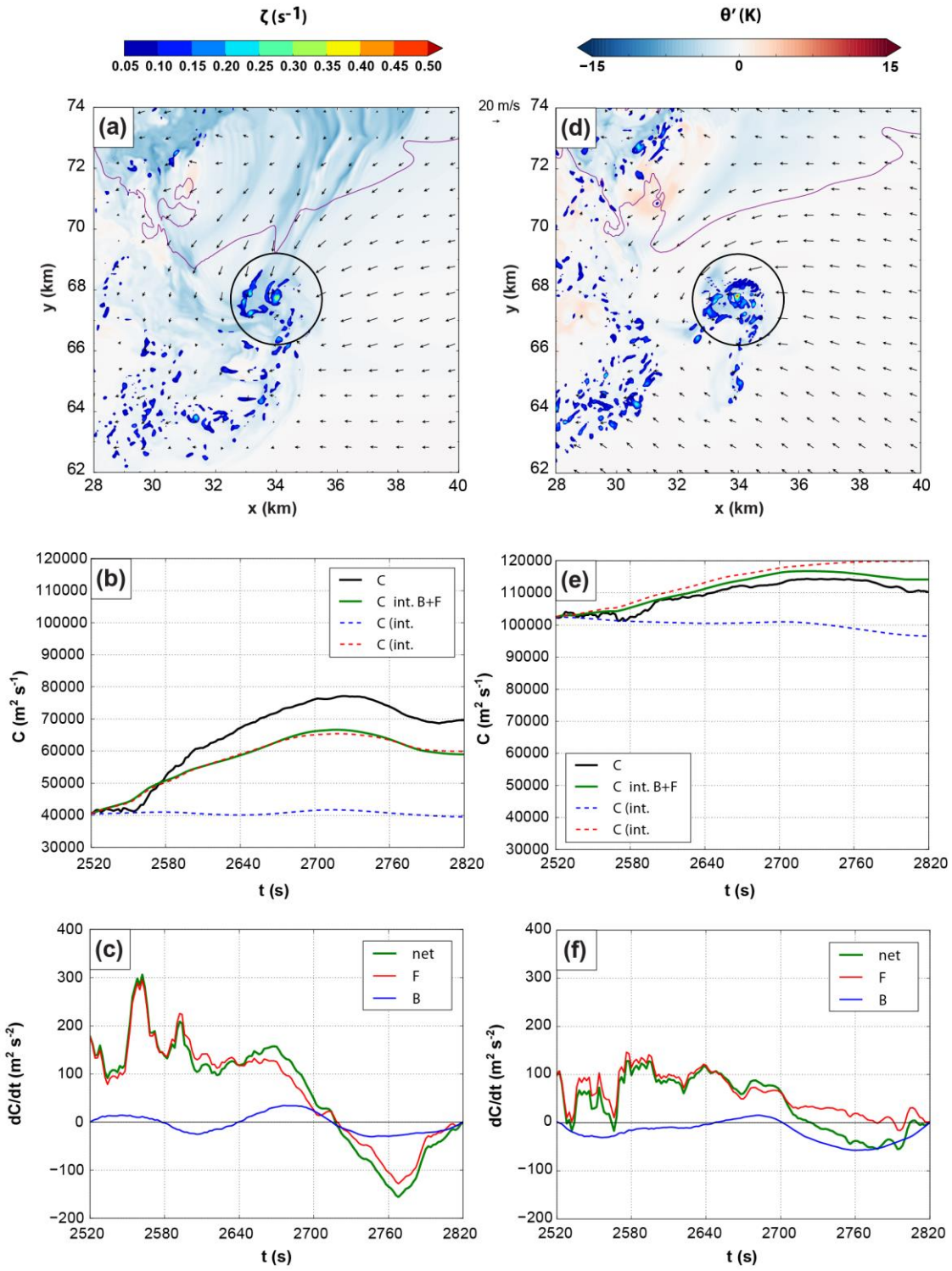

Fig. 5.14. (a) Horizontal cross-section in CD2-2 at 2820 s and 100 m AGL of perturbation potential temperature (shaded), vertical vorticity (overlaid shaded), the 0.3 g kg^{-1} rainwater mixing ratio contour (purple), and wind vectors. The circuit initialized at 100 m AGL and 2820 enclosing the tornado is overlaid as a black circle. (b) Time series of circulation about the circuit interpolated from model wind field (solid black),

integrated from forcing terms (solid green), integrated from mixing forcing only (dashed red), and integrated from baroclinic forcing only (dashed blue) for the circuit. (c) Time series of circulation tendency along the circuit owing to mixing forcing (red), baroclinic forcing (blue), and net forcing (green). (d-f) as in (a-c), except for the circuit initialized at 400 m AGL; the cross-section of model fields in (d) is also taken at 400 m AGL.

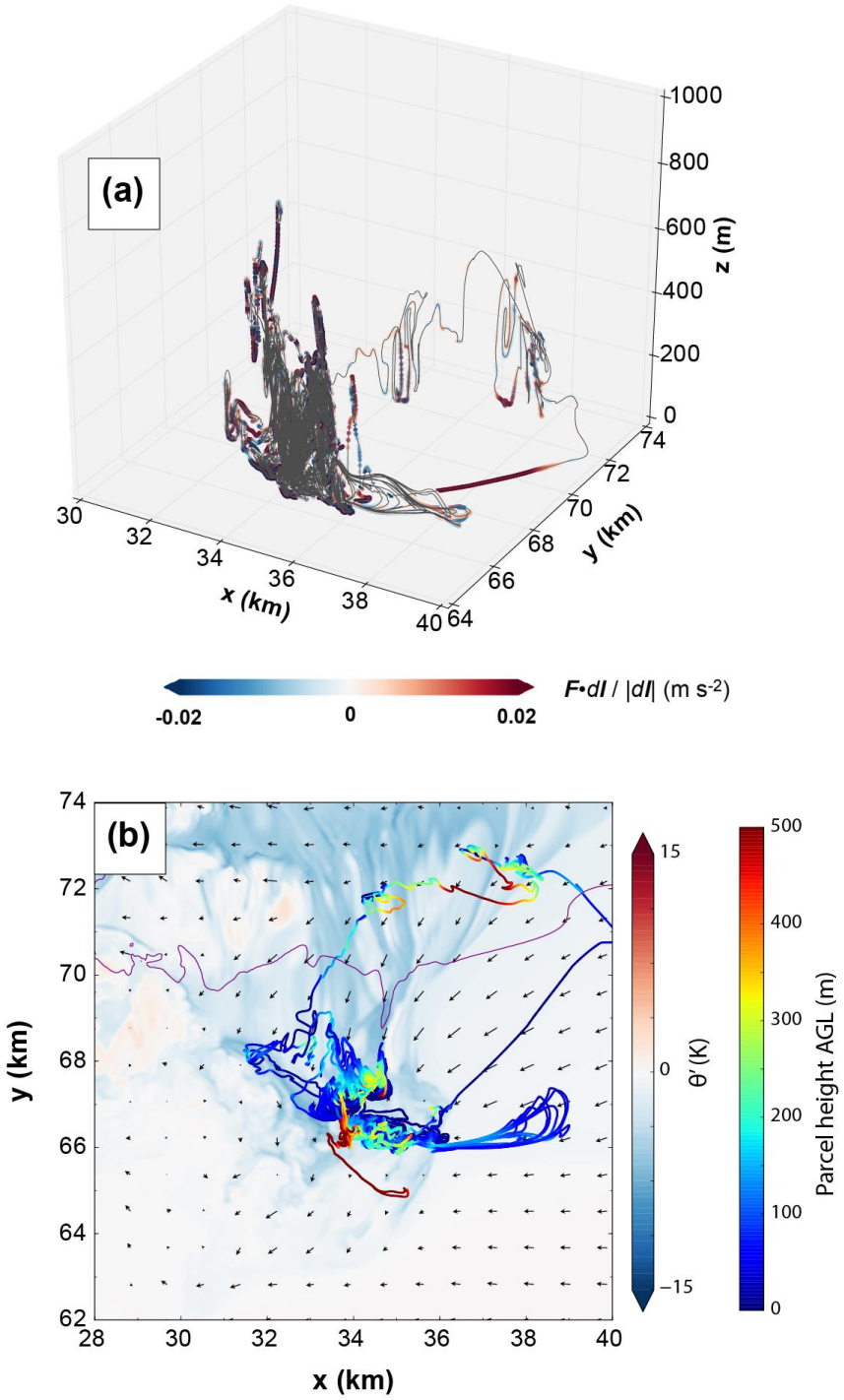

Fig. 5.15. For the circuit initialized enclosing the PTV in CD2-2 at 2820 s and 100 m AGL, (a) the spatial distribution of the circuit at 2580 s, with each inter-parcel segment shaded by the local mixing contribution as in Fig. 5.12; (b) horizontal cross-section in CD2-2 at 100 m AGL and 2580 s of perturbation potential temperature (shaded), 0.3 g kg^{-1} rainwater mixing ratio contour (purple), and wind vectors, with a horizontal projection of the circuit's position at 2580 s (shaded by parcel height) overlaid.

5.3 Summary and conclusions

In this study, a new method (originally conceived by Dr. Daniel Dawson; publication forthcoming) was introduced for maintaining a three-force balance among the horizontal PGF, Coriolis force, and frictional force in idealized single-sounding 3D simulations. This large-scale balance (LSB) technique allows the use of an arbitrary initial sounding in simulations which use parameterized surface drag with constant C_d; without the LSB, surface drag would act to modify the background wind profile over time throughout the domain, particularly near the ground. The LSB technique was employed in five idealized supercell simulations based on sounding MAY3B (from Chapter 3) whose drag coefficients ranged from $C_d = 0$ to $C_d = 0.05$. All the simulations with nonzero drag coefficients produced a low-level mesocyclone 1200-1800 s into the simulation which lowered toward the ground and eventually spawned a strong tornado, similar to FWFRIC in previous chapters. The experiment with $C_d = 0$ was very similar to EnvFRIC, and did not produce a tornado nor an intense near-ground mesocyclone during this period. Material circuits were initialized enclosing the initial low-level mesocyclone during its early intensification phase, integrated backward in time, and circulation budgets were calculated. These budgets suggest surface drag contributes a larger positive proportion of the total circulation for circuits in the experiments with large drag coefficients during this early intensification period. Furthermore, the budgets for circuits in CD0 reveal that in the absence of surface drag, mixing processes (turbulence and numerical diffusion) commonly impose a substantial (15-25% below 1 km AGL) negative contribution to circulation for circuits bound for the low-level mesocyclone.

Later in the simulations, after 3000 s, additional tornadoes occurred in all five experiments. We termed this period the "cool regime" for tornadogenesis, as cool outflow has emanated from the precipitation core and formed a classical RFD by this time. Within the cool regime, the propensity for strong tornadoes among experiments was the opposite of the early mesocyclone: the strongest tornadoes occurred in the experiments with no drag and weak drag, while the experiments with strong drag produced shorter-lived, weaker, and vertically shallower tornadoes. Circulation budgets for material circuits initialized enclosing a PTV in one strong-drag experiment suggested that surface drag may still contribute substantially to near-ground vorticity, but only a 5-min integration window was possible with reliable budgets, owing to the complex wind field. The prevalence of strong flow, and strong gradients in the flow, around the mesocyclone during this regime also prevented reliable circulation budgets for tornadoes and PTVs in other experiments. The roadblocks to assessing vorticity and circulation budgets accurately in this regime suggest trajectory error mitigation strategies should be an essential component of future work on this topic.

A few more qualitative differences in mesocyclone and tornado behavior were noted between experiments. First, low-level mesocyclones in the experiments with drag (particularly strong drag) tended to move rearward behind the RFGF, in a storm-relative sense, quickly after genesis; in the experiment with no drag, tornadoes remained anchored to the intersection of the FFGF and RFGF, and no cyclic mesocyclone behavior was observed during the 4800 s simulation period. Second, zoomed vertical cross-sections of the tornadoes revealed structure that behaved consistently with previous laboratory experiments (Ward 1972) and numerical simulations (Trapp 2000).

Specifically, radial inflow along the ground toward the center of tornadoes in the strong-drag experiments was substantially sharper than in the weak-drag and no-drag experiments. A central axial updraft was observed down to ground level in the experiment with the largest drag coefficient; in the other experiments, strong updraft tended to exist closer to the ground with increasing drag coefficient, and the axial downdraft (if any) tended to be confined to some height above the ground (but extended to the ground in the no-drag experiment).

For typical cases of supercell tornadogenesis in the real world, the most pressing question relevant to our work remains: how much of a role does surface friction play in generating tornadic vorticity when cool downdrafts (and associated baroclinic vorticity) are also present near or surrounding the tornado? The results presented for the cool regime tornadoes herein, along with recent work by Schenkman et al. (2014) and Mashiko (2016b), support the possibility of a prominent role in some cases. In terms of vorticity and circulation budgets, the challenge continues to lie in evaluating these terms along parcel trajectories accurately over a long enough duration to eliminate the possibility of other important sources before the beginning of the budget integration window. Since significant, long-lived tornadoes within the cool regime appear *more difficult* to obtain in our experiments with large C_d (e.g., values realistic for land) than for small or zero C_d, our results should perhaps serve as a warning that such tornadoes are produced too "easily" in idealized free-slip simulations (it is, of course, possible that this result is sounding-dependent, which should be evaluated in future work).

The results presented in this chapter constitute one step forward from the previous chapters toward understanding surface drag's role in supercell tornadogenesis

dynamics, but many steps remain. One such step is to perform experiments similar to those presented herein for a range of different initial soundings, which should illuminate which of our results are generalizable to most storms. Another step is to decrease the horizontal grid spacing by a factor of 2 or 3 to better resolve tornadoes; cross-sections presented herein showed indications that our grid is just fine enough to simulate some semblance of multiple-vortex structure (e.g., Fig. 5.10), but that the subvortices are only marginally resolved, leading to unrealistic structure. Decreasing the vertical grid spacing over the lowest 500 m AGL could also prove immensely helpful in calculating vorticity and circulation budgets along trajectories and circuits bound for tornadoes and low-level mesocyclones, as such parcels tend to originate from below 10 m AGL quite often. The simulations herein also still contain laminar flow in the inflow region, which could possibly be subject to exaggerated near-ground shear as described by Markowski and Bryan (2016); one goal for future work is to eliminate this caveat by inducing turbulence in the far field with small thermal perturbations (steps must be taken to maintain a realistic wind profile and prevent spurious convective updrafts, however). If these steps are taken within the realm of idealized supercell simulations, then alongside real-data, terrain-resolving modeling studies (such as S14 and NM16) which emphasize the role of surface drag in storm dynamics, as well as observational efforts, we are optimistic that an important component of the tornadogenesis problem will soon come into clearer focus.

Chapter 6 Summary and Future Directions

In this dissertation, idealized three-dimensional simulations of supercells were conducted in the Advanced Regional Prediction System (ARPS) and analyzed with the broad goal of elucidating the role of surface drag in tornadogenesis. To that end, two methods were described for imposing a three-force balance among the horizontal PGF, Coriolis force, and frictional force in the simulated background environment. Achieving such a force balance is required to conduct idealized experiments wherein the presence and/or magnitude of surface drag is varied while controlling for the background wind profile. These methods were leveraged successfully in two sets of experiments, and a multitude of differences between the experiments illuminated potential roles of surface drag related directly or indirectly to tornadogenesis.

The first set of experiments employed a friction-balancing technique. This technique involves starting with a sounding that is assumed to be geostrophic, integrating a 1D column run with frictional and "perturbation" Coriolis forces turned on for several hours to achieve a force balance, and then using the final wind profile from the column run to initialize 3D storm simulations. This technique is best suited to running a pair of simulations: one with surface drag specified only as a function of the base-state wind (making it effectively free-slip), and another with surface drag specified in the traditional way. Of the pair, the former simulation can be conceptualized as representing "environmental drag" only (i.e., the background profile contains drag-induced near-ground shear), while the latter simulation represents all of drag's real-world impacts (i.e., perturbations introduced by a simulated storm are directly impacted by friction). In this study, a pair of simulations was conducted starting with a sounding

based on the 3 May 1999 tornado outbreak in Oklahoma. In the "full-wind drag" simulation, a low-level mesocyclone developed after 1200 s, then strengthened, lowered well below 1 km AGL, and produced a tornado after 1500 s. In the "environmental drag" simulation, a similar mesocyclone developed, but did not strengthen rapidly or produce a tornado. Vorticity budgets along trajectories entering the tornado around its genesis time in the "full-wind drag" experiment revealed that many parcels originated from the inflow air east of the vortex, where surface drag generated large horizontal vorticity on the storm scale as air accelerated into the low-level mesocyclone. This enhanced vorticity had a dominantly crosswise component for the inflow parcels, which was exchanged to become streamwise as the parcels curved cyclonically, then ultimately tilted into the vertical near and within the tornado. Baroclinic processes did not play an important role in generating vorticity for this tornado, as no appreciable cold pool existed near the vortex at this time in the simulation. A combination of the enhanced horizontal vorticity generated by friction and the stronger low-level convergence (supporting stronger updrafts) along a storm-scale surface boundary in the "full-wind drag" experiment was implicated in tornadogenesis, as these two factors were unique to that experiment.

The parent mesocyclone evolution was also examined in detail for the aforementioned pair of simulations. It was shown that the mesocyclone in the "full-wind drag" experiment lowered toward the ground more rapidly than in the "environmental drag" experiment due to a positive feedback between enhanced updraft and enhanced mesocyclone vorticity (which induces pressure falls aloft, further strengthening the low-level updraft). Material circuits were initialized around the

mesocyclone in both experiments and traced backward in time while tracking circulation and its tendency terms. The enhanced mesocyclone circulation in the "full-wind drag" simulation was shown to result in large part from the same reservoir of frictionally-enhanced near-ground shear in the inflow region that was implicated in tornadogenesis. Furthermore, circulation budgets for material circuits initialized enclosing the tornado in the "full-wind drag" experiment revealed a monotonic decrease with height in the relative contribution of surface drag to the vortex circulation.

The second set of experiments employed a new large-scale balance (LSB) technique. This LSB technique allows a single-sounding idealized simulation to be initialized using an arbitrary background sounding and (spatiotemporally constant) drag coefficient while remaining in three-force balance through the duration of the simulation. Five experiments were initialized using the same sounding from the first set of experiments, but with varying drag coefficients (C_d = 0, 0.002, 0.005, 0.02, 0.05). During the first 1800 s of the simulations, a low-level mesocyclone developed, intensified, and lowered toward the ground in all experiments with surface drag, eventually producing a tornado; the intensification tended to occur earlier for larger values of C_d. Vertical cross-sections through the tornadoes revealed sharper corner flow and stronger near-ground updraft in the experiments with larger drag coefficients. Material circuits were initialized around the intensifying low-level mesocyclone in the experiments with $C_d > 0$ at several times and heights; circulation budgets for these circuits corroborated the importance of frictionally-generated circulation within the inflow region identified in the first set of experiments, and suggested this effect

becomes more pronounced with increasing C_d. The low-level mesocyclone in the no-drag experiment did not intensify or lower substantially during this period.

The second set of experiments also was integrated out to 4800 s in order to investigate storm and tornado behavior after a classical, precipitation-driven RFD develops. After 3000 s, which we termed the "cool regime" of tornado production, new low-level mesocyclones and tornadoes developed in all five experiments. The no-drag and weak-drag experiments showed the most propensity for strong, long-lived tornadoes in this regime, while the strong-drag experiments generally produced shorter-lived, weaker, and shallower tornadoes. This result serves as a caution that idealized free-slip supercell simulations may possibly tend to produce strong vortices from baroclinic vorticity sources too easily, compared to more realistic semi-slip simulations which use drag coefficients typical for land. Circulation budgets for material circuits initialized enclosing one pre-tornadic vortex in a strong-drag experiment suggested that surface drag may still be important in generating vortex circulation during the cool regime, even with more baroclinic forcing available in the vicinity. However, trajectory errors and rapid divergence between parcels comprising backward-integrated circuits plagued many attempts to evaluate tornado vorticity sources more holistically across experiments, so much work remains in this regard. A qualitative difference in cyclic mesocyclogenesis behavior was also noted between experiments during this period: those with large drag coefficients saw mesocyclones develop and persist for 10-15 min while moving rearward (in a storm-relative sense) within the RFD as a new mesocyclone began to develop along the RFGF, while the no-drag case saw a single, persistent low-level mesocyclone anchored along the FFGF-RFGF intersection.

The results outlined in this dissertation lend to increased confidence that surface drag can meaningfully influence supercell dynamics, including low-level mesocyclogenesis and tornadogenesis. Although numerous aspects of simulated storm and tornado evolution were described and evaluated, the most important result can be summarized succinctly: when near-ground flow bound for a low-level mesocyclone or tornado accelerates, surface drag tends to generate new horizontal vorticity (by retarding flow near the ground more than flow immediately above), and this vorticity may in some cases be reoriented in such a way that it ultimately contributes to the cyclonic vorticity within the mesocyclone or tornado. This phenomenon was described in Schenkman et al. (2014), and has more recently been discussed in a range of modeling studies (Markowski 2016; Mashiko 2016b). Ideally, the results discussed in this dissertation will contribute meaningfully to this ongoing discussion. Operational implications exist for the proposed vorticity generation mechanism, such as the possibility for land use or urban infrastructure to influence storm evolution and tornadogenesis likelihood locally. Future work on this topic within the realm of traditional storm-scale numerical modeling should focus on generalizing the results herein to a broad array of background environments, as well as finding techniques for overcoming the trajectory accuracy limitations encountered for long vorticity and circulation budget windows. Perhaps more importantly, observational techniques must be developed and employed for measuring the near-ground vertical wind profile in supercells (particularly in the inflow sector) with high spatiotemporal resolution, ideally capturing data similar to the tower dataset described in Dowell and Bluestein (1997)

with more regularity. If such steps are taken, there is abundant reason to believe improvements to scientific understanding and NWP will result.

References

Adlerman, E. J., and K. K. Droegemeier, 2002: The Sensitivity of Numerically Simulated Cyclic Mesocyclogenesis to Variations in Model Physical and Computational Parameters. *Mon. Wea. Rev.*, **130,** 2671-2691.

——, 2005: The Dependence of Numerically Simulated Cyclic Mesocyclogenesis upon Environmental Vertical Wind Shear. *Mon. Wea. Rev.*, **133,** 3595-3623.

Agee, E., and E. Jones, 2009: Proposed Conceptual Taxonomy for Proper Identification and Classification of Tornado Events. *Wea. Forecasting*, **24,** 609-617.

Agee, E. M., 2014: A Revised Tornado Definition and Changes in Tornado Taxonomy. *Wea. Forecasting*, **29,** 1256-1258.

Ashley, W. S., 2007: Spatial and Temporal Analysis of Tornado Fatalities in the United States: 1880–2005. *Wea. Forecasting*, **22,** 1214-1228.

Atkins, N. T., and M. S. Laurent, 2009: Bow Echo Mesovortices. Part II: Their Genesis. *Mon. Wea. Rev.*, **137,** 1514-1532.

Atkins, N. T., J. M. Arnott, R. W. Przybylinski, R. A. Wolf, and B. D. Ketcham, 2004: Vortex Structure and Evolution within Bow Echoes. Part I: Single-Doppler and Damage Analysis of the 29 June 1998 Derecho. *Mon. Wea. Rev.*, **132,** 2224-2242.

Bluestein, H. B., 1985: The formation of a "landspout" in a "broken-line" squall line in Oklahoma. *14th Conf. on Severe Local Storms*, American Meteorological Society.

——, 2007: Advances in applications of the physics of fluids to severe weather systems. *Rep. Prog. Phys.*, **70,** 1259-1323.

Boustead, J. M., and K. L. R. Gross, 2016: Environmental Factors in the Varying Length of Time between First Echo and First Tornado. *28th AMS Conference on Severe Local Storms*, Portland, OR.

Brandes, E. A., 1978: Mesocyclone Evolution and Tornadogenesis: Some Observations. *Mon. Wea. Rev.*, **106,** 995-1011.

Brasseur, J. G., and T. Wei, 2010: Designing large-eddy simulation of the turbulent boundary layer to capture law-of-the-wall scalinga). *Phys. of Fluids*, **22,** 021303.

Brooks, H. E., C. A. Doswell, and R. B. Wilhelmson, 1994: The Role of Midtropospheric Winds in the Evolution and Maintenance of Low-Level Mesocyclones. *Mon. Wea. Rev.*, **122,** 126-136.

Brotzge, J., and W. Donner, 2013: The Tornado Warning Process: A Review of Current Research, Challenges, and Opportunities. *Bull. Amer. Meteor. Soc.*, **94,** 1715-1733.

Brotzge, J. A., S. E. Nelson, R. L. Thompson, and B. T. Smith, 2013: Tornado Probability of Detection and Lead Time as a Function of Convective Mode and Environmental Parameters. *Wea. Forecasting*, **28,** 1261-1276.

Browning, K. A., 1964: Airflow and Precipitation Trajectories Within Severe Local Storms Which Travel to the Right of the Winds. *J. Atmos. Sci.*, **21,** 634-639.

Browning, K. A., and R. J. Donaldson, 1963: Airflow and Structure of a Tornadic Storm. *J. Atmos. Sci.*, **20,** 533-545.

Chow, F. K., R. L. Street, M. Xue, and J. H. Ferziger, 2005: Explicit Filtering and Reconstruction Turbulence Modeling for Large-Eddy Simulation of Neutral Boundary Layer Flow. *J. Atmos. Sci.*, **62,** 2058-2077.

Coffer, B. E., and M. D. Parker, 2017: Simulated Supercells in Nontornadic and Tornadic VORTEX2 Environments. *Mon. Wea. Rev.*, **145,** 149-180.

Dahl, J. M. L., 2015: Near-Ground Rotation in Simulated Supercells: On the Robustness of the Baroclinic Mechanism. *Mon. Wea. Rev.*

Dahl, J. M. L., M. D. Parker, and L. J. Wicker, 2012: Uncertainties in Trajectory Calculations within Near-surface Mesocyclones of Simulated Supercells. *Mon. Wea. Rev.*

——, 2014: Imported and Storm-Generated Near-Ground Vertical Vorticity in a Simulated Supercell. *J. Atmos. Sci.*, **71,** 3027-3051.

Davies-Jones, R., 1984: Streamwise Vorticity: The Origin of Updraft Rotation in Supercell Storms. *J. Atmos. Sci.*, **41,** 2991-3006.

——, 2014: A review of supercell and tornado dynamics. *Atmospheric Research*, **158–159,** 274-291.

Davies-Jones, R., and H. Brooks, 1993: Mesocyclogenesis from a Theoretical Perspective. *The Tornado: Its Structure, Dynamics, Prediction, and Hazards*, American Geophysical Union, 105-114.

Davies-Jones, R., and P. Markowski, 2013: Lifting of Ambient Air by Density Currents in Sheared Environments. *J. Atmos. Sci.*, **70,** 1204-1215.

Davies-Jones, R., D. Burgess, and M. P. Foster, 1990: Test of helicity as a tornado forecast parameter. *16th AMS Conference on Severe Local Storms*, American Meteorological Society, 216-219.

Davies-Jones, R., R. J. Trapp, and H. B. Bluestein, 2001: Tornadoes and Tornadic Storms. *Severe Convective Storms*, Meteorological Monographs, 167-221.

Davies-Jones, R. P., 1982: Observational and Theoretical Aspects of Tornadogenesis. *Intense Atmospheric Vortices*, L. Bengtsson, and J. Lighthill, Eds., Springer Berlin Heidelberg, 175-189.

Dawson, D. T., M. Xue, J. A. Milbrandt, and M. K. Yau, 2010: Comparison of Evaporation and Cold Pool Development between Single-Moment and Multimoment Bulk Microphysics Schemes in Idealized Simulations of Tornadic Thunderstorms. *Mon. Wea. Rev.*, **138,** 1152-1171.

Dawson, D. T., M. Xue, J. A. Milbrandt, and A. Shapiro, 2015: Sensitivity of Real-Data Simulations of the 3 May 1999 Oklahoma City Tornadic Supercell and Associated Tornadoes to Multimoment Microphysics. Part I: Storm- and Tornado-Scale Numerical Forecasts. *Mon. Wea. Rev.*, **143,** 2241-2265.

Dowell, D. C., and H. B. Bluestein, 1997: The Arcadia, Oklahoma, Storm of 17 May 1981: Analysis of a Supercell during Tornadogenesis. *Mon. Wea. Rev.*, **125,** 2562-2582.

Droegemeier, K. K., S. M. Lazarus, and R. Davies-Jones, 1993: The Influence of Helicity on Numerically Simulated Convective Storms. *Mon. Wea. Rev.*, **121,** 2005-2029.

Duda, J. D., and W. A. Gallus, 2010: Spring and Summer Midwestern Severe Weather Reports in Supercells Compared to Other Morphologies. *Wea. Forecasting*, **25,** 190-206.

Elsner, J. B., and Coauthors, 2016: The Relationship between Elevation Roughness and Tornado Activity: A Spatial Statistical Model Fit to Data from the Central Great Plains. *J. Appl. Meteor. Climatol.*, **55,** 849-859.

Forbes, G. S., and R. M. Wakimoto, 1983: A Concentrated Outbreak of Tornadoes, Downbursts and Microbursts, and Implications Regarding Vortex Classification. *Mon. Wea. Rev.*, **111,** 220-236.

French, M. M., H. B. Bluestein, I. PopStefanija, C. A. Baldi, and R. T. Bluth, 2013: Reexamining the Vertical Development of Tornadic Vortex Signatures in Supercells. *Mon. Wea. Rev.*, **141,** 4576-4601.

Fujita, T. T., 1971: Proposed characterization of tornadoes and hurricanes by area and intensity, 42 pp.

Golden, J. H., 1971: Waterspouts and tornadoes over South Florida. *Mon. Wea. Rev.*, **99,** 146-154.

Grasso, L. D., and W. R. Cotton, 1995: Numerical Simulation of a Tornado Vortex. *J. Atmos. Sci.*, **52,** 1192-1203.

Grice, G. K., and Coauthors, 1999: The Golden Anniversary Celebration of the First Tornado Forecast. *Bull. Amer. Meteor. Soc.*, **80,** 1341-1348.

Grzych, M. L., B. D. Lee, and C. A. Finley, 2007: Thermodynamic Analysis of Supercell Rear-Flank Downdrafts from Project ANSWERS. *Mon. Wea. Rev.*, **135,** 240-246.

Houser, J. L., H. B. Bluestein, and J. C. Snyder, 2016: A Finescale Radar Examination of the Tornadic Debris Signature and Weak-Echo Reflectivity Band Associated with a Large, Violent Tornado. *Mon. Wea. Rev.*, **144,** 4101-4130.

Katona, B., P. Markowski, C. Alexander, and S. Benjamin, 2016: The Influence of Topography on Convective Storm Environments in the Eastern United States as Deduced from the HRRR. *Wea. Forecasting*, **31,** 1481-1490.

Klemp, J. B., and R. B. Wilhelmson, 1978a: The Simulation of Three-Dimensional Convective Storm Dynamics. *J. Atmos. Sci.*, **35,** 1070-1096.

——, 1978b: Simulations of Right- and Left-Moving Storms Produced Through Storm Splitting. *J. Atmos. Sci.*, **35,** 1097-1110.

Klemp, J. B., and R. Rotunno, 1983: A Study of the Tornadic Region within a Supercell Thunderstorm. *J. Atmos. Sci.*, **40,** 359-377.

Klemp, J. B., R. B. Wilhelmson, and P. S. Ray, 1981: Observed and Numerically Simulated Structure of a Mature Supercell Thunderstorm. *J. Atmos. Sci.*, **38,** 1558-1580.

Lee, B. D., C. A. Finley, and C. D. Karstens, 2012: The Bowdle, South Dakota, Cyclic Tornadic Supercell of 22 May 2010: Surface Analysis of Rear-Flank Downdraft Evolution and Multiple Internal Surges. *Mon. Wea. Rev.*, **140,** 3419-3441.

Lemon, L. R., and C. A. Doswell, 1979: Severe Thunderstorm Evolution and Mesocyclone Structure as Related to Tornadogenesis. *Mon. Wea. Rev.*, **107,** 1184-1197.

Leslie, L. M., 1971: The development of concentrated vortices: A numerical study. *J. Fluid Mech.*, **48,** 1-21.

Lewellen, D. C., W. S. Lewellen, and J. Xia, 2000: The Influence of a Local Swirl Ratio on Tornado Intensification near the Surface. *J. Atmos. Sci.*, **57,** 527-544.

Lewellen, W. S., D. C. Lewellen, and R. I. Sykes, 1997: Large-Eddy Simulation of a Tornado's Interaction with the Surface. *J. Atmos. Sci.*, **54,** 581-605.

Lin, Y.-L., R. D. Farley, and H. D. Orville, 1983: Bulk Parameterization of the Snow Field in a Cloud Model. *Journal of Climate and Applied Meteorology*, **22,** 1065-1092.

Markowski, P., Y. Richardson, and G. H. Bryan, 2015: How does surface drag affect the development of near-surface vertical vorticity in supercell thunderstorms? *8th European Conference on Severe Storms*, Wiener Neustadt, Austria.

Markowski, P., Y. Richardson, E. Rasmussen, J. Straka, R. Davies-Jones, and R. J. Trapp, 2008: Vortex Lines within Low-Level Mesocyclones Obtained from Pseudo-Dual-Doppler Radar Observations. *Mon. Wea. Rev.*, **136,** 3513-3535.

Markowski, P., and Coauthors, 2012: The pretornadic phase of the Goshen County, Wyoming, supercell of 5 June 2009 intercepted by VORTEX2. Part II: Intensification of low-level rotation. *Mon. Wea. Rev.*

Markowski, P. M., 2016: An Idealized Numerical Simulation Investigation of the Effects of Surface Drag on the Development of Near-Surface Vertical Vorticity in Supercell Thunderstorms. *J. Atmos. Sci.*, **73,** 4349-4385.

Markowski, P. M., and Y. P. Richardson, 2014: The Influence of Environmental Low-Level Shear and Cold Pools on Tornadogenesis: Insights from Idealized Simulations. *J. Atmos. Sci.*, **71,** 243-275.

Markowski, P. M., and G. H. Bryan, 2016: LES of Laminar Flow in the PBL: A Potential Problem for Convective Storm Simulations. *Mon. Wea. Rev.*, **144,** 1841-1850.

Markowski, P. M., E. N. Rasmussen, and J. M. Straka, 1998: The Occurrence of Tornadoes in Supercells Interacting with Boundaries during VORTEX-95. *Wea. Forecasting*, **13,** 852-859.

Markowski, P. M., J. M. Straka, and E. N. Rasmussen, 2002: Direct Surface Thermodynamic Observations within the Rear-Flank Downdrafts of Nontornadic and Tornadic Supercells. *Mon. Wea. Rev.*, **130,** 1692-1721.

Marquis, J., Y. Richardson, P. Markowski, D. Dowell, and J. Wurman, 2012: Tornado Maintenance Investigated with High-Resolution Dual-Doppler and EnKF Analysis. *Mon. Wea. Rev.*, **140,** 3-27.

Marquis, J., Y. Richardson, P. Markowski, J. Wurman, K. Kosiba, and P. Robinson, 2016: An Investigation of the Goshen County, Wyoming, Tornadic Supercell of 5 June 2009 Using EnKF Assimilation of Mobile Mesonet and Radar Observations Collected during VORTEX2. Part II: Mesocyclone-Scale Processes Affecting Tornado Formation, Maintenance, and Decay. *Mon. Wea. Rev.*, **144,** 3441-3463.

Mashiko, W., 2016a: A Numerical Study of the 6 May 2012 Tsukuba City Supercell Tornado. Part I: Vorticity Sources of Low-Level and Midlevel Mesocyclones. *Mon. Wea. Rev.*, **144,** 1069-1092.

——, 2016b: A Numerical Study of the 6 May 2012 Tsukuba City Supercell Tornado. Part II: Mechanisms of Tornadogenesis. *Mon. Wea. Rev.*, **144,** 3077-3098.

Mashiko, W., H. Niino, and T. Kato, 2009: Numerical Simulation of Tornadogenesis in an Outer-Rainband Minisupercell of Typhoon Shanshan on 17 September 2006. *Mon. Wea. Rev.*, **137,** 4238-4260.

Mason, P. J., and D. J. Thomson, 1992: Stochastic backscatter in large-eddy simulations of boundary layers. *J. Fluid Mech.*, **242,** 51-78.

Moeng, C.-H., and J. C. Wyngaard, 1988: Spectral Analysis of Large-Eddy Simulations of the Convective Boundary Layer. *J. Atmos. Sci.*, **45,** 3573-3587.

Noda, A. T., and H. Niino, 2010: A Numerical Investigation of a Supercell Tornado: Genesis and Vorticity Budget. *Journal of the Meteorological Society of Japan*, **88,** 135-159.

Nolen, R. H., 1959: A radar pattern associated with tornadoes. *Bull. Amer. Meteor. Soc.*, **40,** 277-279.

Nowotarski, C. J., and P. M. Markowski, 2016: Modifications to the Near-Storm Environment Induced by Simulated Supercell Thunderstorms. *Mon. Wea. Rev.*, **144,** 273-293.

Nowotarski, C. J., P. M. Markowski, Y. P. Richardson, and G. H. Bryan, 2015: Supercell Low-Level Mesocyclones in Simulations with a Sheared Convective Boundary Layer. *Mon. Wea. Rev.*, **143,** 272-297.

Orf, L., R. Wilhelmson, B. Lee, C. Finley, and A. Houston, 2017: Evolution of a Long-Track Violent Tornado within a Simulated Supercell. *Bull. Amer. Meteor. Soc.*, **98,** 45-68.

Palmer, R. D., and Coauthors, 2011: Observations of the 10 May 2010 Tornado Outbreak Using OU-PRIME: Potential for New Science with High-Resolution Polarimetric Radar. *Bull. Amer. Meteor. Soc.*, **92,** 871-891.

Przybylinski, R. W., 1995: The Bow Echo: Observations, Numerical Simulations, and Severe Weather Detection Methods. *Wea. Forecasting*, **10,** 203-218.

Rasmussen, E. N., S. Richardson, J. M. Straka, P. M. Markowski, and D. O. Blanchard, 2000: The Association of Significant Tornadoes with a Baroclinic Boundary on 2 June 1995. *Mon. Wea. Rev.*, **128,** 174-191.

Rasmussen, E. N., J. M. Straka, R. Davies-Jones, C. A. D. III, F. H. Carr, M. D. Eilts, and D. R. MacGorman, 1994: Verification of the Origins of Rotation in Tornadoes Experiment: VORTEX. *Bull. Amer. Meteor. Soc.,* **75,** 995-1006.

Roberts, B., and M. Xue, 2017, in press: The Role of Surface Drag in Mesocyclone Intensification Leading to Tornadogenesis within an Idealized Supercell Simulation. *J. Atmos. Sci.*

Roberts, B., M. Xue, A. D. Schenkman, and D. T. D. II, 2016: The Role of Surface Drag in Tornadogenesis within an Idealized Supercell Simulation. *J. Atmos. Sci.,* **73,** 3371-3395.

Rotunno, R., 1977: Numerical Simulation of a Laboratory Vortex. *J. Atmos. Sci.*, **34,** 1942-1956.

Rotunno, R., and J. B. Klemp, 1982: The Influence of the Shear-Induced Pressure Gradient on Thunderstorm Motion. *Mon. Wea. Rev.*, **110,** 136-151.

Rotunno, R., and J. Klemp, 1985: On the Rotation and Propagation of Simulated Supercell Thunderstorms. *J. Atmos. Sci.,* **42,** 271-292.

Rotunno, R., P. M. Markowski, and G. H. Bryan, 2017: 'Near-ground' vertical vorticity in supercell thunderstorm models. *J. Atmos. Sci.*, **0,** null.

Schenkman, A. D., M. Xue, and A. Shapiro, 2012: Tornadogenesis in a Simulated Mesovortex within a Mesoscale Convective System. *J. Atmos. Sci.*

Schenkman, A. D., M. Xue, and M. Hu, 2014: Tornadogenesis in a High-Resolution Simulation of the 8 May 2003 Oklahoma City Supercell. *J. Atmos. Sci.*, **71,** 130-154.

Schenkman, A. D., M. Xue, and D. T. D. II, 2016: The Cause of Internal Outflow Surges in a High-Resolution Simulation of the 8 May 2003 Oklahoma City Tornadic Supercell. *J. Atmos. Sci.*, **73,** 353-370.

Shabbott, C. J., and P. M. Markowski, 2006: Surface In Situ Observations within the Outflow of Forward-Flank Downdrafts of Supercell Thunderstorms. *Mon. Wea. Rev.*, **134,** 1422-1441.

Skamarock, W. C., M. L. Weisman, and J. B. Klemp, 1994: Three-Dimensional Evolution of Simulated Long-Lived Squall Lines. *J. Atmos. Sci.*, **51,** 2563-2584.

Skinner, P. S., C. C. Weiss, M. M. French, H. B. Bluestein, P. M. Markowski, and Y. P. Richardson, 2014: VORTEX2 Observations of a Low-Level Mesocyclone with Multiple Internal Rear-Flank Downdraft Momentum Surges in the 18 May 2010 Dumas, Texas, Supercell. *Mon. Wea. Rev.*, **142,** 2935-2960.

Smith, B. T., R. L. Thompson, J. S. Grams, C. Broyles, and H. E. Brooks, 2012: Convective Modes for Significant Severe Thunderstorms in the Contiguous United States. Part I: Storm Classification and Climatology. *Wea. Forecasting,* **27,** 1114-1135.

Snook, N., and M. Xue, 2008: Effects of microphysical drop size distribution on tornadogenesis in supercell thunderstorms. *Geophys. Res. Lett.*, **35,** L24803.

Tang, B., and Coauthors, 2016: Topographic and Boundary Influences on the 22 May 2014 Duanesburg, New York, Tornadic Supercell. *Wea. Forecasting*, **31,** 107-127.

Thompson, R. L., B. T. Smith, J. S. Grams, A. R. Dean, and C. Broyles, 2012: Convective Modes for Significant Severe Thunderstorms in the Contiguous United States. Part II: Supercell and QLCS Tornado Environments. *Wea. Forecasting*, **27,** 1136-1154.

Trapp, R. J., 1999: Observations of Nontornadic Low-Level Mesocyclones and Attendant Tornadogenesis Failure during VORTEX*. *Mon. Wea. Rev.*, **127,** 1693-1705.

Trapp, R. J., 2000: A Clarification of Vortex Breakdown and Tornadogenesis. *Mon. Wea. Rev.*, **128,** 888-895.

Trapp, R. J., and B. H. Fiedler, 1995: Tornado-like Vortexgenesis in a Simplified Numerical Model. *J. Atmos. Sci.*, **52,** 3757-3778.

Trapp, R. J., and R. Davies-Jones, 1997: Tornadogenesis with and without a Dynamic Pipe Effect. *J. Atmos. Sci.*, **54,** 113-133.

Trapp, R. J., G. J. Stumpf, and K. L. Manross, 2005: A Reassessment of the Percentage of Tornadic Mesocyclones. *Wea. Forecasting*, **20,** 680-687.

Wakimoto, R. M., and J. W. Wilson, 1989: Non-supercell Tornadoes. *Mon. Wea. Rev.*, **117,** 1113-1140.

Wakimoto, R. M., and N. T. Atkins, 1996: Observations on the Origins of Rotation: The Newcastle Tornado during VORTEX 94. *Mon. Wea. Rev.*, **124,** 384-407.

Ward, N. B., 1972: The Exploration of Certain Features of Tornado Dynamics Using a Laboratory Model. *J. Atmos. Sci.*, **29,** 1194-1204.

Weisman, M. L., and J. B. Klemp, 1982: The Dependence of Numerically Simulated Convective Storms on Vertical Wind Shear and Buoyancy. *Mon. Wea. Rev.*, **110,** 504-520.

Weisman, M. L., and C. A. Davis, 1998: Mechanisms for the Generation of Mesoscale Vortices within Quasi-Linear Convective Systems. *J. Atmos. Sci.*, **55,** 2603-2622.

Weisman, M. L., and R. J. Trapp, 2003: Low-Level Mesovortices within Squall Lines and Bow Echoes. Part I: Overview and Dependence on Environmental Shear. *Mon. Wea. Rev.*, **131,** 2779-2803.

Wicker, L. J., and R. B. Wilhelmson, 1993: Numerical Simulation of Tornadogenesis Within a Supercell Thunderstorm. *The Tornado: Its Structure, Dynamics, Prediction, and Hazards*, American Geophysical Union, 75-88.

——, 1995: Simulation and Analysis of Tornado Development and Decay within a Three-Dimensional Supercell Thunderstorm. *J. Atmos. Sci.*, **52,** 2675-2703.

Wilson, J. W., 1986: Tornadogenesis by Nonprecipitation Induced Wind Shear Lines. *Mon. Wea. Rev.*, **114,** 270-284.

WSEC, 2006: A recommendation for an Enhanced Fujita Scale (EF-Scale), 95 pp.

Wurman, J., and Coauthors, 2012: The Second Verification of the Origins of Rotation in Tornadoes Experiment: VORTEX2. *Bull. Amer. Meteor. Soc.*, **93,** 1147-1170.

Xue, M., K. K. Droegemeier, and V. Wong, 2000: The Advanced Regional Prediction System (ARPS) – A multi-scale nonhydrostatic atmospheric simulation and prediction model. Part I: Model dynamics and verification. *Meteor. Atmos. Phys*, **75,** 161-193.

Xue, M., M. Hu, and A. D. Schenkman, 2014: Numerical Prediction of the 8 May 2003 Oklahoma City Tornadic Supercell and Embedded Tornado Using ARPS with the Assimilation of WSR-88D Data. *Wea. Forecasting*, **29,** 39-62.

Xue, M., K. Zhao, M. Wang, Z. Li, and Y. Zheng, 2016: Recent significant tornadoes in China. *Advances in Atmospheric Sciences*, **33,** 1209-1217.

Xue, M., and Coauthors, 2001: The Advanced Regional Prediction System (ARPS) - A multi-scale nonhydrostatic atmospheric simulation and prediction tool. Part II: Model physics and applications. *Meteor. Atmos. Phys*, **76,** 143-165.